Fabrication and characterization of micromachined dielectric thin films and temperature sensors using thermoluminescence

A DISSERTATION
SUBMITTED TO THE FACULTY OF THE GRADUATE SCHOOL
OF THE UNIVERSITY OF MINNESOTA
BY

Sangho Sam Kim

IN PARTIAL FULFILLMENT OF THE REQUIREMENTS
FOR THE DEGREE OF
Doctor of Philosophy

Joseph J. Talghader

March, 2013

Acknowledgements

There are many people who have earned my gratitude for their contribution to my time in graduate school. Most of all, special thanks goes to my advisor Joseph J. Talghader for supporting, advising and encouraging me to conditionally do in-depth research all the time. Three committee members would be appreciated for serving on my final defense committee. My colleague, Nick Gabriel who is now working at 3M, was a great helper not only for collaboration work but also for paper correction in the first two journals that I published. Merlin Mah and Phil Armstrong made it possible to achieve my third journal paper with the great help of Matlab coding and experimental setting. In addition, I am grateful to all my lab members, Dr. Woo-Bin Song, Yuyan Wang, Anand Gawarikar, Brad Tiffany, Jan Makowski, Ryan Shea, Wing Shan Chan, Kyle Olson, and Luke Taylor.

Part of this work was carried out in the UMN Nanofabrication Center (NFC) which receives partial support from NSF through the NNIN program. Many NFC staff members helped me to enable the fabrication processes presented in this dissertation. In particular I would like to thank Kevin Roberts, Tony Whipple, Gary Olin, and Terry Brough.

Part of this work was also carried out in the UMN Characterization Facility, which receives partial support from NSF through the MRSEC program. Help from Bob Hafner with Scanning Electron Microscope (SEM) imaging is appreciated in particular.

This research is made possible by serveral funding sources: the Joint Technology Office (JTO) and the United States Air Force Office of Scientific Research (USAFOSR) for funding support under the Multidisciplinary University Research Initiative (MURI); the Office of Naval Research (ONR); and the Defense Threat Reduction Agency (DTRA).

I am grateful to Nik Nadeau and Steve Wunrow for reviewing my dissertation. I

also wanted to thank my wife who is always supporting and encouraging me to do more work in school than at home. I would also like to thank my parents, especially my father who passed away and did not have chance to see my final dissertation. All my work cannot be done without his silent support.

Dedication

To my family, Eunhee Yang, Hana Kim, Eagan Kim, and to my parents

Abstract

High-power laser technology has a number of applications, whether for the military (i.e., anti-missile weaponry) or for material processing, medical surgery, laser-induced nuclear fusion, and high-density data storage. However, external obstacles could cause a laser to problematically change its direction. Optical components such as mirrors already address this problem by deflecting a laser beam, but can be damaged easily due to the intensity of the laser. Therefore, this dissertation examines how to improve reliability of high power laser application systems by three significant standards. First, we demonstrate that an atomic layer deposition (ALD) of Al_2O_3 can stabilize novel dielectric optical mirrors composed of SiO_2 nanorods, whose porosity makes it attractive for use as a low refractive index material. Such a deposition can stabilize material properties in dry versus humid atmospheres, where both the refractive index and coefficient of thermal expansion (CTE) vary dramatically. This encapsulation ability is demonstrated in dielectric multilayers as a Distributed Bragg Reflector (DBR). Second, we show that the difference in hydroxyl signatures of micromachined dielectric membranes can make detection of optical materials' laser damage more accurate. This signature difference, appearing as the decrease in post-laser absorption peaks associated with hydroxyl groups (OH), is measured by Fourier transform infrared spectroscopy and corresponds to regions of high fluence from a Nd:YAG laser. This detection technique will be useful to determine the lifespan of the optical components used in a high power laser. Third, we find that heterogeneous thermoluminescent (TL) multilayers composed of LiF:Mg,Ti and CaF_2:Dy with Kapton as an interlayer can enhance reconstruction of laser heating events through thermal gradients that penetrate deep into a material, thereby preserving memory of the temperature history of the surface. Using the finite-difference time-domain method (FDTD) and the first order kinetics model of TL, we estimate dynamic heat transfer and then populate the final luminescent intensity. A thermal contact conductance between the critical layers is also introduced to better simulate experimental results, thereby resolving dynamic temperatures by hundreds of milliseconds.

Contents

List of Tables

List of Figures

Chapter 1

Introduction

High-power laser technology has been attractive for a number of applications, such as materials processing (e.g., welding, cutting, drilling, etc.) and medical surgery (e.g., LASIK [Laser-Assisted in Situ Keratomileusis]) in order to make cuts precise to the micrometer [2]. High-power lasers are also useful for military anti-missile weaponry systems, allowing for pinpoint accuracy and unparalleled speed [2]. Furthermore, high-density data storage technology also benefits from high-power lasers as a light and heat source for optical data storage, heat-assisted magnetic recording (HAMR), and phase-change memory [3, 4, 5].

These lasers often require optical components which can deflect or guide the laser beam to a certain location. For instance, waveguides can direct and deliver the light to its final destination. Optical mirrors, made of either metal or dielectric materials, are also necessary to deflect a laser beam if external obstacles disrupt the laser's direct path. However, most optical components and materials can be vulnerable and damaged easily due to the laser's intensity. Therefore, this dissertation examines three ways to improve reliability of high-power laser application systems, namely, improving the durability of optical mirror materials, increasing the accuracy of laser damage threshold detection, and enhancing reconstruction of laser heating events through thermal gradients.

The first project in this dissertation involoves improvement of the durability of optical mirror materials. Thin films consisting of SiO_2 nanorods are of great interest because they tend to have a refractive index lower than the bulk value of about 1.46, which is especially useful in distributed Bragg reflectors [6] and anti-reflection coatings

[7]. In principle, there is an inverse relationship between film porosity and refractive index because the air trapped between nanorods reduces the composite refractive index of the film. Oblique-angle deposition makes it possible to grow these nanorods due to the self-shadowing effect [6]. There is a region where deposition is blocked due to self-shadowing. This effect creates nanorod thin films. A DBR made of the same material can be also realized by this oblique angle deposition [8].

Increasing the porosity, however, also causes the film to interact unfavorably with the external environment so that material properties such as refractive index and coefficient of thermal expansion (CTE) are unstable. For instance, water, with a refractive index of 1.33, can be trapped in the pores and boost the overall refractive index of a thin film, with the effect depending heavily on the level of surrounding humidity [9]. In addition to SiO_2, there are many other films whose mechanical properties are dependent on environmental conditions as well, for example, zirconium tungstate thin films [10] show different CTEs in dry versus wet environments.

In this first project we demonstrate that it is possible to stabilize porous films and prevent them from interacting with the ambient by coating ALD Al_2O_3 on top of the unstable dielectric films. This technique will be extremely important, not just for mirrors which need to be precisely controlled over temperature, but also for making thermally invariant mirrors [11].

The second project is about the laser damage threshold detection. The first sign of optical coating failure in high power laser systems is often disastrous. Because high power mirrors can be extremely expensive and often require tight alignment and mechanical assembly, it may not be possible to have backup mirrors. Ideally one would like to have an *in situ* method to assess the state of a coating that could predict damage prior to catastrophic failure. In this manner, one may be able to adapt the illumination or to repair the local area before one loses the entire mirror.

There has been much research focusing on the detection of laser-induced damage using laser scattering [12], integrated photothermal microscopy[13], total internal reflection microscopy [14, 15], high frequency scanning acoustic microscopy [16], optical coherence tomography [17, 18], and photoacoustic microscopy [19]. Not only can some methods detect the damage non-destructively, but also locate subsurface defects which are embedded deep inside of the coatings. However, most methods assume that the

optical coatings have particulate defects which may not be the same material as the coating; thus it is not apparent that they could detect the fundamental mechanism of material thermal collapse.

To expand on some methods mentioned previously, laser scattering has been suggested to observe damage in optical coatings [12]. This method has the advantage of utilizing the laser light itself and therefore needs no secondary equipment. However, the method requires that the source of the coating failure is one or more particulates whose size, number, or optical constants increase with time but well before catastrophic failure occurs. While particulate failure can certainly be tracked in this way, it is not clear that the underlying mechanisms of materials failure are captured by it.

Photothermal microscopy [13] has also been used to predict the impact of laser damage in real-time. During, *et al.* [20] described a pump-probe experiment where a pump optical pulse heats a silica film embedded with gold nanoparticles. This pulse slightly heats the local area around the beam and reduces the refractive index, deflecting a probe beam. Since pump-beam heating is related to the local absorption of the film, so is the probe-beam deflection. This technique can detect nanoparticles in the coatings of interest while also providing information about the surface profile. While the technique can obtain information on the onset of laser damage, it would be unable to identify the physical mechanisms accompanying such damage.

In this project, we investigate if fundamental thin film characteristics could be used to track damage in optical coatings. Since it is likely that any degradation in coating strength is accompanied by a change in bond structure, a materials technique that could quantify this change might be able to predict the onset of coating damage prior to catastrophic failure. Infrared absorption measures dipole transitions directly between different molecular vibrational states. Should any characteristics of local bonding change, it will show up in the infrared absorption spectrum. Perhaps the most common type of laser damage is laser-induced thermal damage. This can occur in a highly local area due to particulate absorption, but it can also occur over a larger area due to the absorption of the coating itself. Prior research into the properties of annealed thin films has shown that the infrared hydroxyl (OH) signature often decreases under high temperature annealing due to the desorption of water [21].

The final project or the third project is about the reconstruction of laser heating

events through thermal gradients. Thermoluminescence (TL) has been used extensively in radiation dosimetry [1] and sedimentary dating [22]. In general, luminescence emission is explained as the transfer of energy from radiation to the electrons of the solid, thus exciting the electrons from a ground state to an excited state [1]. The emission of a luminescence photon takes place when an excited electron returns to its ground state [1]. Furthermore, an excited electron can become trapped at a certain level, called a trap center, where the electron will remain until it is given enough energy to return to the excited state, before undergoing a normal transition back to the grounded state [1].

Laser-stimulated TL has been a popular research topic because it has applications to micro-dosimetry and high resolution TL imaging [23, 24]. For example, Braunlich *et. al.* first devised a laser stimulated TL system using a CO_2 laser and $CaSO_4$:Mn powder. In particular, he measured the two-dimensional TL pattern of the surface with localized laser heating [23].

Since then, there have been many attempts to study the laser-stimulated TL both theoretically and experimentally. The heat conduction model of LiF:Mg,Ti powder on top of a borosilicate glass substrate was solved analytically by Abtah *et. al.* [25, 26], focusing on laser-generated heat diffused into the LiF:Mg,Ti powder through the glass substrate, which resulted in a delayed TL response. Young *et. al.* also tried to calculate the temperature distributions of a similar LiF:Mg,Ti on a glass substrate for simple dynamic system where the laser could be turned on and off [27].

More recently, TL has found useful applications in determining the temperature history of rapid thermal events [28, 29]. Mah et. al. demonstrated that TL microparticle sensors can record the thermal history of detonated high explosives [30]. Microparticles of TL materials are uniquely suited for the detailed profiling of extremely violent temperature events, such as the explosive destruction of biological particles, which would destroy existing direct-contact sensors. TL microparticles have no fabricated components, are often composed of highly robust materials, and are inexpensive and relatively simple to fabricate in large quantities [28]. In [28], microparticles were spread onto the fabricated microheaters, which later can be used for TL measurement. However, these microparticles were difficult to integrate with the microheaters and vulnerable to external vibration, causing them to spread to locations where they can no longer produce a TL signal.

In this study, we suggest that thermal gradients in heterogeneous multilayered TL structures can provide a detailed record of thermal events. We model the TL responses of a three-layer TL structure for the case where laser-induced heating on one TL layer diffuses into another TL layer, resulting in different temperature distribution. To verify these simulation results, LiF:Mg,Ti and CaF_2:Dy samples are used and bonded with Kapton as an interlayer. These bonded TL composites produced strong multiple peaks from their component materials, whose individual contributions were distinguished in both the time and wavelength domains.

This dissertation addresses various elements of physics, including optics, solid mechanics, heat transfer, and thermoluminescence of dielectric materials. The first three chapters of this dissertation will review theories on which this research is based, while the remaining chapters address research methodology, results, and analysis. A brief summary of these chapters is as follows:

- Chapter 1 explains optomechanical modeling of dielectric thin films, which will be later applied to chapters 4 and 5.
- Chapter 2 examines heat transfer modeling and simulation, which will be beneficial for chapter 6.
- Chapter 3 explicates the theory of thermoluminescence later used in chapter 6, where heat converts to luminescence according to band gap theory.
- Chapter 4 presents this study's own examination of SiO_2 nanorod thin films encapsulated by ALD Al_2O_3 , including fabrication of nanorods and their application to optical mirror engineering in high-power laser conditions.
- Chapter 5 assesses the use of Fourier transform infrared spectroscopy for detecting laser damage in dielectric thin films.
- Chapter 6 describes how heterogenous dielectric TL multilayers can help to more accurately reconstruct a rapid thermal event.

Chapter 2

Optomechanical modeling of dielectric thin films

This chapter will provide a background of optics and solid mechanics of dielectric thin films.

2.1 Thermomechanical beam bending theory of dielectric thin films

The primary focus of this thesis is dielectric thin films, particularly their thermomechanical and optical properties. In this section, thermomechanical properties will be studied as they relate to thermal laser events.

Figure 2.1 shows how multi-layered thin films react to heating. Upon heating, whole multi-layers may deform in various ways, depending on the thermomechanical properties of each thin film. As shown in the fig 2.1, Young's modulus, thickness, and the coefficient of thermal expansion (CTE) are the most important parameters that determine whether a whole structure bends downward or upward. In this way, thermo-mechanical modeling can prove useful for designing thermally invariant mirrors, which enhance resistance to thermal expansion and therefore improve the accuracy of a lasers wavefront. In this section, the basic equation for thermally induced curvature bending will be studied.

The theory starts with three basic governing equations. The first is a force balance,

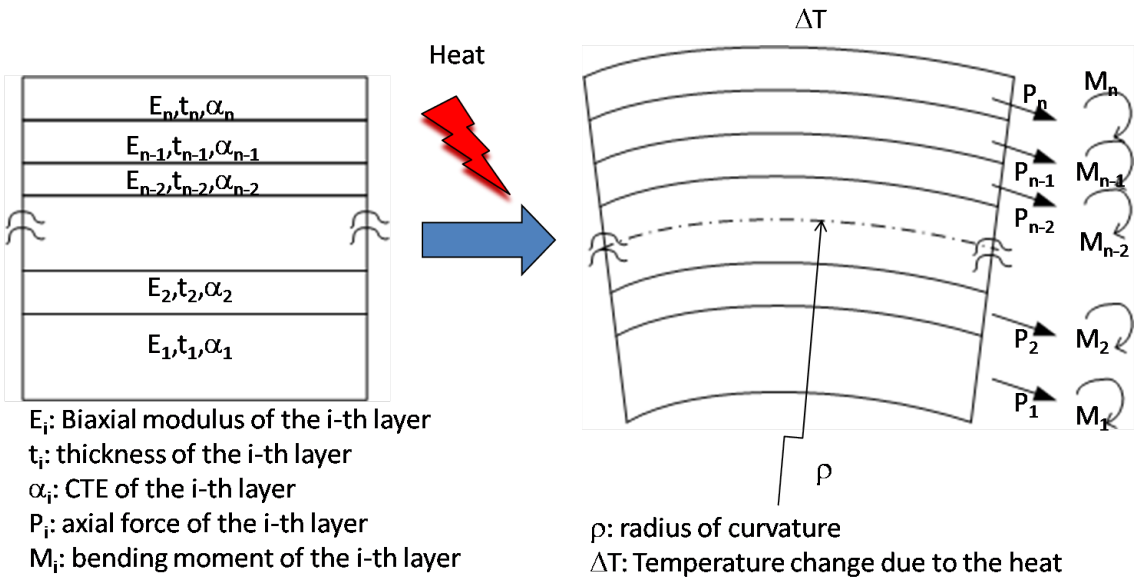

Figure 2.1: Diagram for multilayer beam deflection theory

in which all existing forces should sum to zero, as shown below:

$$\sum_{i=1}^{n} P_i = 0 \tag{2.1}$$

where, p_i stands for force in the i-th film.

The second equation is for moment balance. In this equation, the principle is the same as the force balance, and the sum of moment should zero out. We have:

$$\sum_{i=1}^{n} M_i + \sum_{i=1}^{1} \left[P_i \left(\sum_{j=1}^{i-1} t_j + \frac{t_i}{2} \right) \right] = 0 \tag{2.2}$$

where M_i is the moment in the i-th film. t_i is the thickness in the i-th film.

$$M_i = \frac{E_i I_i}{\rho} = \frac{E_i t^3}{12\rho} \tag{2.3}$$

where M is moment, E is Young's Modulus, I is moment of inertia ($= t^3/12$), ρ is radius of curvature, respectively.

Plugging (2.3) into (2.2) will lead to:

$$\frac{1}{\rho} \sum_{i=1}^{n} E_i t_i^3 + 12 \sum_{i=1}^{1} \left(\sum_{j=1}^{i-1} t_j + \frac{t_i}{2} \right) P_i = 0 \tag{2.4}$$

The last equation required is for continuity of strain. In other words, the strain and stress of materials inside should be continuous. Strain itself in this case consists of three parts: thermal strain, the one driven by force, and moment-driven strain. Therefore, the i-th strain should be equal to the neighboring strain, or the i+1-th strain. The total of the sum of the strain is composed of temperature driven, force driven, and moment driven strains, as shown below:

$$\epsilon_{sum} = \epsilon_{\Delta T} + \epsilon_P + \epsilon_M \tag{2.5}$$

One can expand the above equation as follows:

$$\alpha_i \Delta T + \frac{P_i}{E_i t_i} + \frac{t_i}{2\rho} = \alpha_{i+1} \Delta T + \frac{P_{i+1}}{E_{i+1} t_{i+1}} + \frac{t_{i+1}}{2\rho} \tag{2.6}$$

where α_i is the Coefficient of Thermal Expansion (CTE) of i-th layer and ΔT is the temperature difference from room temperature, and ρ is the curvature of the multilayer.

Taking $\sum_{k=1}^{j-1}$ of (2.6),

$$\sum_{k=1}^{j-1} (\alpha_{k+1} - \alpha_k) \Delta T = \frac{P_1}{E_1 t_1} - \frac{P_j}{E_j t_j} + \frac{1}{2\rho} \sum_{k=1}^{j-1} (t_{k+1} + t_k) \tag{2.7}$$

Likewise, taking $\sum_{k=1}^{j-1}$ of (2.6),

$$\sum_{k=1}^{i-1} (\alpha_{k+1} - \alpha_k) \Delta T = \frac{P_1}{E_1 t_1} - \frac{P_j}{E_j t_j} + \frac{1}{2\rho} \sum_{k=1}^{i-1} (t_{k+1} + t_k) \tag{2.8}$$

Let's substract (2.8) from (2.7), then

$$\begin{aligned} \sum_{k=1}^{j-1} (\alpha_{k+1} - \alpha_k) \Delta T - \sum_{k=1}^{i-1} (\alpha_{k+1} - \alpha_k) \Delta T = \frac{P_i}{E_i t_i} - \frac{P_j}{E_j t_j} \\ + \frac{1}{2\rho} \left[\sum_{k=1}^{j-1} (t_{k+1} + t_k) - \sum_{k=1}^{i-1} (t_{k+1} + t_k) \right] \end{aligned} \tag{2.9}$$

The third term in RHS (Right Hand Side) of this equation can be further simplified as follows:

$$\begin{aligned} \sum_{k=1}^{j-1} (t_{k+1} + t_k) - \sum_{k=1}^{i-1} (t_{k+1} + t_k) &= t_1 + t_j + 2 \sum_{k}^{j-1} t_k - \left(t_1 + t_i + 2 \sum_{k}^{i-1} t_k \right) \\ &= t_j - t_i + 2 \sum_{k}^{j-1} - 2 \sum_{k}^{i-1} t_k \end{aligned} \tag{2.10}$$

Therefore, (2.9) can be rewritten as:

$$\sum_{k=1}^{j-1}(\alpha_{k+1}-\alpha_k)\,\Delta T-\sum_{k=1}^{i-1}(\alpha_{k+1}-\alpha_k)\,\Delta T=\frac{P_i}{E_it_i}-\frac{P_j}{E_jt_j}+\frac{1}{2\rho}\left[t_j-t_i+2\sum_{k}^{j-1}t_k-2\sum_{k}^{i-1}t_k\right] \tag{2.11}$$

In order to remove the term, P_j because $_j=0$ by 2.1, multiply (2.11) by E_jt_j,

$$\begin{aligned}\frac{P_i}{E_it_i}\sum_{j=1}^{n}E_jt_j=\sum_{j=1}^{n}E_jt_j\left[\sum_{k=1}^{j-1}(\alpha_{k+1}-\alpha_k)\Delta T-\sum_{k=1}^{i-1}(\alpha_{k+1}-\alpha_k)\Delta T\right]\\ +\frac{1}{\rho}\sum_{j=1}^{n}E_jt_j\left[t_i-t_j+2\sum_{k}^{j-1}t_k-2\sum_{k}^{i-1}t_k\right]\end{aligned} \tag{2.12}$$

Finally one can calculate the i-th force as functions of thickness, Youngs Modulus, and CTE as follows:

$$\begin{aligned}P_i &= \frac{E_it_i}{\sum_j^i E_jt_j}\left[\frac{1}{\rho}\sum_{j}^{n}E_jt_j\left(\frac{t_i-t_j}{2}+\sum_{k}^{i-1}t_k-\sum_{k}^{j-1}t_k\right)\right]\\ &+ \frac{E_it_i}{\sum_j^i E_jt_j}\left[\sum_{j}^{n}E_jt_j\left(\sum_{k}^{j-1}(\alpha_{k+1}-\alpha_k)\Delta T-\sum_{k}^{i-1}(\alpha_{k+1}-\alpha_k)\Delta T\right)\right]\end{aligned} \tag{2.13}$$

Plugging (2.13) into (2.4),

$$\frac{1}{\rho}\sum_{i=1}^{n}E_it_i^3=-12\sum_{i=1}^{n}\frac{E_it_i}{\sum_j^n E_jt_j}(h_{i-1}+\frac{t_i}{2})\left[\frac{1}{\rho}\sum_{j}^{n}E_jt_j(\frac{t_i-t_j}{2}+h_{i-1}-h_{j-1})+\sum_{j}^{n}E_jt_j(\alpha_j-\alpha_i)\Delta T\right] \tag{2.14}$$

In the long run, the curvature of the multilayer can be expressed as a function of thickness, CTE, and Modulus, as follows:

$$\frac{1}{\rho_{thermal}}=\frac{6\sum_{i=1}^{n}E_it_i\,(2h_{i-1}+t_i)\,\{\sum_j^n E_jt_j(\alpha_i-\alpha_j)\Delta T\}}{\sum_i^n E_it_i\{\sum_j^n E_jt_j^3+3(2h_{i-1})\sum_j^n E_jt_j(t_i-t_j+2h_{i-1}-2h_{j-1})}=A\Delta T \tag{2.15}$$

where $h_i=\sum_k^i t_k$ and $A=\frac{6\sum_{i=1}^{n}E_it_i(2h_{i-1}+t_i)\{\sum_j^n E_jt_j(\alpha_i-\alpha_j)\}}{\sum_i^n E_it_i\{\sum_j^n E_jt_j^3+3(2h_{i-1})\sum_j^n E_jt_j(t_i-t_j+2h_{i-1}-2h_{j-1})}$. A similar formula and derivation can be found in [31].

The usual case is when the only unknown is the thin film CTE, which can be easily derived from (2.15). If there is initial curvature as ρ_0, the following equation can give out the solution for α_f, the thin film CTE:

$$\frac{1}{\rho_{total}}=\frac{1}{\rho_0}+\frac{1}{\rho_{thermal}}=\frac{1}{\rho_0}+A\Delta T \tag{2.16}$$

where A is a term derived in equation 2.15.

A simple version of this equation can be derived for a sanity check. The first version is for two layer's case:

$$\begin{aligned} \frac{1}{\rho} &= \frac{6E_1E_2t_2(t_1+t_2)(\alpha_2-\alpha_1)\Delta T}{(E_1t_1+E2t_2)(E1t_1^3+E_2t_2^3)+3E_1t_1E_2t_2(t_1+t_2)^2} \\ &= \frac{(\alpha_f-\alpha_s)\Delta T}{\frac{h}{2}+\frac{E_st_s^3+E_ft_f^3}{6h}\left(\frac{1}{E_st_s}+\frac{1}{E_ft_f}\right)} \end{aligned} \tag{2.17}$$

where $h = t_1 + t_2$ or $h = t_s + t_f$ where s stands for substrate and f for film. The latter equation in (2.17) is well known as Timoshenko's formula for bi-metal thermostats [32]. In a case when the substrate thickness is significantly larger than the thin film thickness ($t_s >> t_f$). Then, (2.17) can be further simplified as follows:

$$\frac{1}{\rho} = \frac{6E_ft_f(\alpha_f-\alpha_s)\Delta T}{E_st_s^2} \tag{2.18}$$

Since $\sigma = (\alpha_f - \alpha_s)\Delta T$,

$$\sigma_{Stoney} = \frac{E_st_s^2}{6t_f\rho} \tag{2.19}$$

which is also well known for Stoney's formula [33]. Therefore, these two simplified versions can determine whether (2.15) is derived correctly.

2.2 Theory of optical thin films

In the previous section, the thermomechanical properties of dielectric thin films have been investigated. In this section, the optical aspects of dielectric thin films will be explained. Dielectric films are often used as optical thin films, such as anti-reflection coatings and dielectric mirrors [34, 35]. Since they do not absorb light (the extinction coefficient, or k, is almost zero), they have been attractive for high-power and high-precision optics applications. This thesis applies the dielectric thin films to a mirror application called DBR (Distributed Bragg Reflector).

The principles of optical reflectance originate from Maxwell's electromagnetic field equations. There are several ways to calculate the optical reflectance of light propagation into the dielectric films. Here, an optical transmission matrix method is regarded as the easiest solution for optical reflectance calculations, because one can calculate the total

reflectance simply by multiplying the matrices corresponding to each thin film[36]. If the optical beam is incident upon the thin film interface, reflection as well as transmission occurs, as shown in Fig. 2.2 assuming no absorption.

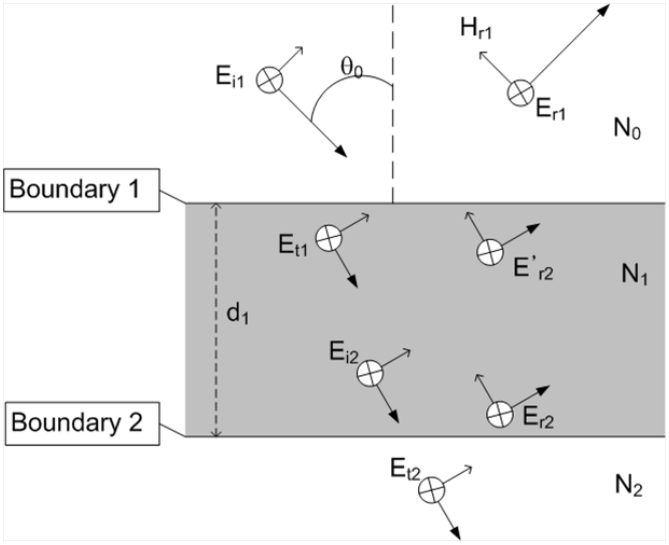

Figure 2.2: Electromagnetic field in interface layer with TE mode

Sinc there are two distinguished cases of polarization, we focus on TE (Transverse Electric) mode for illustration, where the electric field is perpendicular to the incident plane [37]. At boundary 1, the incident electric field should be equal to the sum of reflected and trasmitted field, according to continuity of tangential components [38, 36]:

$$E_1 = E_{i1} + E_{r1} = E_{t1} + E'_{r2} \tag{2.20}$$

where E stands for electric field, subscript of r, t, 1, 2 means reflectance, transmission, boundary 1, and boundary 2, respectively. The same principle will be applied to the magnetic field, which can be expressed as follows:

$$H_1 = H_{i1}\cos\theta_0 - H_{r1}\cos\theta_0 = H_{t1}\cos\theta_1 - H'_{r2}\cos\theta_1 \tag{2.21}$$

where $H_m = \sqrt{\frac{\epsilon_0}{\mu_0}} N_m E$, θ is incident angle, ϵ is permittivity, and N is refractive index, respectively.

Let $\eta_m = \sqrt{\frac{\epsilon_0}{\mu_0}} N_m \cos\theta_m$, then magnetic field equation will be further simplified:

$$H_1 = \eta_0 \left(E_{i1} - E_{r1}\right) = \eta_1 \left(E_{t1} - E'_{r2}\right) \tag{2.22}$$

The same equation can be set up for the boundary 2:

$$E_2 = E_{i2} + E_{r2} = E_{t2} \tag{2.23}$$

$$H_2 = \eta_0 \left(E_{i2} - E_{r2}\right) = \eta_2 E_{t2} \tag{2.24}$$

E_{i2} can be expressed as follows with a phase shift term, since $\vec{E} = Ee^{i(\omega t - kz)}$.

$$E_{i2} = E_{t1} e^{-i\delta} \tag{2.25}$$

where $\delta = \frac{2\pi N_1 d_1 \cos\theta_1}{\lambda}$, and d_1 is the film thickness.

Likewise:

$$E_{r2} = E'_{r2} e^{i\delta} \tag{2.26}$$

Therefore, E field equation for boundary 2 will be:

$$E_2 = E_{t1} e^{-i\delta} + E'_{r2} e^{i\delta} = E_{t2} \tag{2.27}$$

H field equation for boundary 2 will be:

$$H_2 = \eta_1 \left(E_{t1} e^{-1\delta} - E'_{r2} e^{i\delta}\right) = \eta_2 E_{t2} \tag{2.28}$$

In order to establish a relationship between boundaries 1 and 2, E'_{r2} and E_{t1} need to be removed from (2.20), (2.22), (2.27), and (2.28). (2.27)$\times\eta_1$ - (2.28) will lead to

$$\eta_1 E_2 - H_2 = E'_{r2} \tag{2.29}$$

$$E'_{r2} = \frac{\eta_1 E_2 - H_2}{2\eta_1 e^{i\delta}} = \frac{e^{-i\delta}}{2}(E_2 - H_2/\eta_1) \tag{2.30}$$

Plugging (2.30) into (2.27), one can derive the following equation:

$$E_2 = E_{t1} e^{-i\delta} + \frac{1}{2}\left(E_2 - H_2/\eta_1\right)$$

$$E_{t1} = \frac{e^{i\delta}}{2}(E_2 + H_2/\eta_2) \tag{2.31}$$

(2.31) and (2.30) into (2.20),

$$E_1 = E_{t1} + E'_{r2} = E_2\left(\frac{e^{i\delta} + e^{-i\delta}}{2}\right) + H_2\left(\frac{e^{i\delta} + e^{-i\delta}}{2}\right) = \cos\delta E_2 + \frac{i\sin\delta}{\eta_1} H_2 \tag{2.32}$$

Likewise, (2.31) and (2.30) into (2.22):

$$H_1 = E_2\left(\frac{e^{i\delta}-e^{-i\delta}}{2}\right)\eta_1 + H_2\left(\frac{e^{i\delta}+e^{-i\delta}}{2}\right) = \eta_1 i\sin\delta \times E_2 + \cos\delta \times H_2 \tag{2.33}$$

Finally, the electromagnetic field in boundary 1 can be calculated by multiplying the matrix, which represents the thin film's property with the electromagnetic field in boundary 2:

$$\begin{bmatrix} E_1 \\ H_1 \end{bmatrix} = \begin{bmatrix} \cos\delta & i\frac{\sin\delta}{\eta_1} \\ \eta_1 i\sin\delta & \cos\theta \end{bmatrix} \begin{bmatrix} E_2 \\ H_2 \end{bmatrix} = M \begin{bmatrix} E_2 \\ H_2 \end{bmatrix} \tag{2.34}$$

The final goal is to calculate optical reflectance, i.e., E_{r1}/E_{i1}. The equation (2.34) can re-expressed as follows:

$$\begin{bmatrix} E_{i1}+E_{r1} \\ \eta_0(E_{i1}-E_{r1}) \end{bmatrix} = M \begin{bmatrix} E_{t2} \\ \eta_2 E_{t2} \end{bmatrix} \tag{2.35}$$

(2.35)$/E_{t2} \longrightarrow$

$$\begin{bmatrix} E_{i1}/E_{t2}+E_{r1}/E_{t2} \\ \eta_0(E_{i1}/E_{t2}-E_{r1}/E_{t2}) \end{bmatrix} = M \begin{bmatrix} 1 \\ \eta_2 \end{bmatrix} = \begin{bmatrix} B \\ C \end{bmatrix} \tag{2.36}$$

$$B = E_{i1}/E_{t2} + E_{r1}/E_{t2} \tag{2.37}$$

$$C = \eta_0(E_{i1}/E_{t2} - Er1/E_{t2}) \tag{2.38}$$

$\eta_0\times$ (2.37) + (2.38) $\longrightarrow$

$$\frac{E_{i1}}{E_{t2}} = \frac{\eta_0 B + C}{2\eta_0} \longrightarrow \frac{E_{t2}}{E_{i1}} = \frac{2\eta_0}{\eta_0 B + C} \tag{2.39}$$

(2.39) $\longrightarrow$ (2.37) will be:

$$\frac{E_{r1}}{E_{t2}} = B - \frac{\eta_0 B + C}{2\eta_0} = \frac{\eta_0 B - C}{2\eta_0} \tag{2.40}$$

Finally,

$$\frac{E_{r1}}{E_{i1}} = \frac{E_{r1}}{E_{t2}}\frac{E_{t2}}{E_{i1}} = \frac{\eta_0 B - C}{\eta_0 B + C} \tag{2.41}$$

Therefore, optical reflectance will be

$$R = \left|\frac{E_{r1}}{E_{i1}}\right|^2 = \left|\frac{\eta_0 B - C}{\eta_0 B - C}\right|^2 \tag{2.42}$$

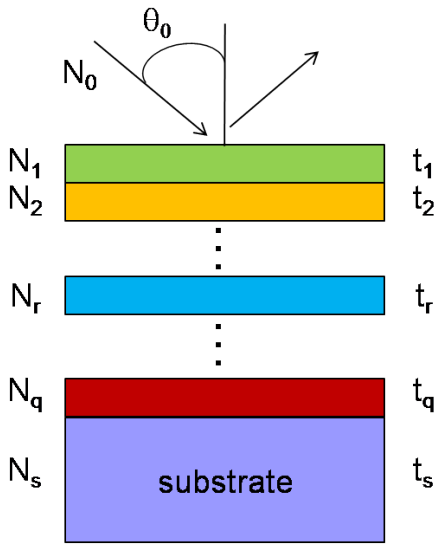

Figure 2.3: Illustration of optical matrix method

where $B = \frac{E_{t1}}{Et2} + \frac{E_{r1}}{E_{t2}}$ and $C = \eta_0 \left(\frac{E_{t1}}{Et2} - \frac{E_{r1}}{E_{t2}} \right)$. The reflectanc for TM (Transverse Magnetic) mode where magnetic file is perpendicular to the incident plane can be derived in a similar fashion as explained above [36].

The reflectance of multi-layered structures can easily be calculated by multiplying all the layers' properties, as shown in the equation (2.43) and illustrated in the Fig. 2.3. Starting with $N_r = n_r - ik_r$ as a complex refractive index where n_r is for real refractive index and k_r is the imaginary refractive index or often called extinction coefficient,

$$\begin{bmatrix} B \\ C \end{bmatrix} = \left\{ \prod_{r=1}^{q} \begin{bmatrix} \cos\delta_r & i\frac{\sin\delta}{\eta_r} \\ i\eta_r \sin\delta_r & \cos\delta_r \end{bmatrix} \right\} \begin{bmatrix} 1 \\ \eta_s \end{bmatrix} \tag{2.43}$$

where

$$\delta_r = \frac{2\pi \times N_r t_r \cos\theta_r}{\lambda} \tag{2.44}$$

and

$$\eta_{r,s,0} = \begin{cases} yN_{r,s,0}\cos\theta_{r,s,0} \text{ for s-polarization (TE)} \\ yN_{r,s,0}/\cos\theta_{r,s,0} \text{ for p-polarization (TM)} \end{cases} \tag{2.45}$$

The final reflectance will be evident in the following equation:

$$R = \left(\frac{\eta_0 B - C}{\eta_0 B + C} \right)^* \left(\frac{\eta_0 B - C}{\eta_0 B + C} \right) \tag{2.46}$$

where $*$ stands for complex conjugate [36].

The real simulation results will be shown in later chapter 5 with the real experiment compared. Briefly speaking, this theory fits fairly well with the real measurement.

2.3 Finite Difference Time Domain Method of Light Propagation

In the previous section, we modeled optical reflectance with an optical matrix method. In this chapter, the Finite Difference Time Domain (FDTD) method will be discussed, as this method can visualize how the optical beam propagates into the multi-layered dielectric films. In addition, the FDTD method is a useful numerical analysis tool when theoretical equations cannot be solved easily. Most parts of this section were extensively extracted from class notes and projects, as noted in reference [39].

The FDTD method offers a way to solve time-domain differential equations numerically. Analytical solutions very often do not exist, even for relatively simple geometries. With the right parameters, however, FDTD solutions can be very nearly exact. Algorithms are simple to implement in code with MATLAB in this thesis. Maxwell equations lend themselves nicely to FDTD analysis, since they enable numerical experimentation, thereby saving significant time with a fabrication or experiment. The derivatives in a differential equation are replaced with a set of algebraic and numeric approximations [39].

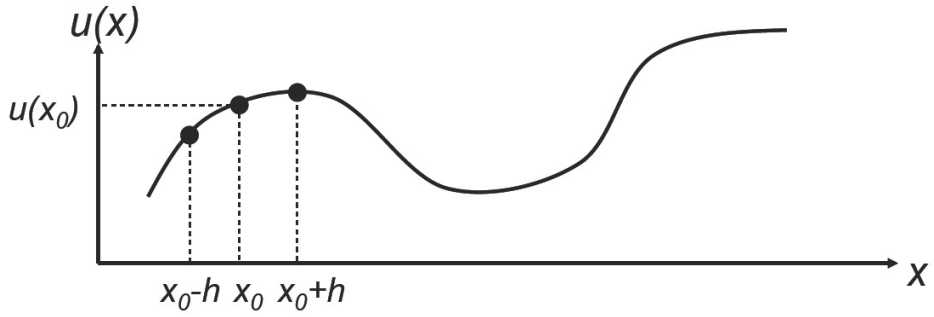

Figure 2.4: Illustration for FDTD derivative [39]

To begin with the FDTD, derivatives of a certain function can be represented, which

will be estimated as forward difference, backward difference, or central difference. These derivatives originated from Taylor Series Expansion, the overview of which will be omitted in this thesis. As shown in fig. 2.4, the derivative of $u(x_0)$ can be derived as follows. In the forward difference, x_0 is compared with the forward point, $x_0 + h$ where h is a finite distance.

$$\frac{du}{dx}|_{x_0} \simeq \frac{u(x_0+h) - u(x_0)}{(x_0+h) - x_0} = \frac{u(x_0+h) - u(x_0)}{h} \tag{2.47}$$

Likewise, one can derive the backward difference easily:

$$\frac{du}{dx}|_{x_0} \simeq \frac{u(x_0) - u(x_0-h)}{h} \tag{2.48}$$

The second derivative is itself a derivative of the first, so forward and backward difference can be combined together as derivative approximation:

$$\begin{aligned} \frac{d^2u}{dx^2}|_{x_0} &\simeq \frac{\frac{u(x_0)-u(x_0)}{h} - \frac{u(x_0)-u(x_0-h)}{h}}{h} \\ &= \frac{u(x_0+h) - 2u(x_0) + u(x_0-h)}{h^2} \end{aligned} \tag{2.49}$$

Light propagation into a medium, which occurs in dielectric films in this case, can be treated as wave. The governing equation of this propagation, as shown below, addresses only one-dimensional problems for simplicity. Figure 2.5 shows the illustration of this 1D wave equation. It starts with the following governing equation:

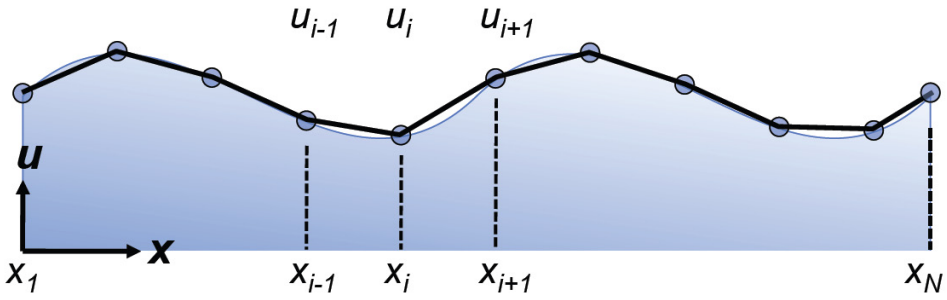

Figure 2.5: Illustration for FDTD 1D Wave equation [39]

$$\frac{\partial^2 u}{\partial t^2} = c^2 \frac{\partial^2 u}{\partial x} \tag{2.50}$$

where u is a wave as either vector or scalar (usually as electric field or magnetic field), t is time, x is positin, and c is constant. The following is the term for discretization of the equation (2.50).

$$\begin{aligned} x &\to x_i = i\Delta x \\ t &\to t_n = n\Delta t \\ u(x,t) &\to u(x_i,t_n) = u_i^n \\ \partial x &\to \Delta x \\ \partial t &\to \Delta t \end{aligned} \tag{2.51}$$

Then the 1D wave equation becomes as follows:

$$\frac{u(x_i,t_{n+1}) - 2u(x_i,t_n) + u(x_i,t_{n-1})}{\Delta t^2} = c^2 \frac{u(x_{i+1},t_n) - 2u(x_i,t_n) + u(x_{i-1},t_n)}{\Delta x^2} \tag{2.52}$$

2.3.1 Stability condition

There is a stability condition that needs to be met to solve this FDTD equation in (2.52). If this condition is not met, the solution will not converge. That is,

$$r = \left(\frac{c\Delta t}{\Delta x}\right)^2 \tag{2.53}$$

With the r plugged back in the original equation, one can reach the following:

$$\begin{aligned} u_i^{n+1} - 2u_i^n + u_i^{n-1} &= r\left(u_{i+1}^n - 2u_i^n + u_{i-1}^n\right) \\ \implies u_i^{n+1} &= 2(1-r)u_i^n + r\left(u_{i+1}^n + u_{i-1}^n\right) - u_i^{n-1} \end{aligned} \tag{2.54}$$

Let's plug the following equation into (2.54),

$$\begin{aligned} u(x,t) &= a(t)e^{jkx} \\ u_i^n &= a^n e^{jki\Delta x} \end{aligned} \tag{2.55}$$

then, (2.54) becomes

$$a^{n+1}e^{jki\Delta x} = 2(1-r)a^n e^{jki\Delta x} + r\left(e^{jki\Delta x} + a^n e^{-jki\Delta x}\right) - a^{n-1}e^{jki\Delta x} \tag{2.56}$$

Since $cos(\theta) = \frac{e^{i\theta}+e^{-i\theta}}{2}$,

$$\begin{aligned} a^{n+1} &= \left[2(1-r) + 2r\cos(k\Delta x)\right] a^n - a^{n-1} \\ \longrightarrow a^{n+1} &- 2\left[1 - r\left(1 - \cos k\Delta x\right)\right] a^n + a^{n-1} = 0 \end{aligned} \tag{2.57}$$

where $(1 - \cos k\Delta x) = 2\sin^2 \frac{k\Delta x}{2}$ and divide the above equation by a^{n-1}. The final equation will be:

$$a^2 - 2\left(1 - 2r\sin^2 k\Delta x\right) a + 1 = 0 \tag{2.58}$$

With the quadratic formula, one can derive the condition, which has to do with real number for **a**, as follows:

$$a = 1 - 2r\sin^2\frac{k\Delta x}{2} \pm \sqrt{\left(1 - 2r\sin^2\frac{k\Delta x}{2}\right)^2 - 1} \tag{2.59}$$

In order for **a** to be real number, the value of the inside root should be larger than or equal to zero. Therefore,

$$\begin{aligned} \left(1 - 2r\sin^2\frac{k\Delta x}{2}\right)^2 &\geq 1 \\ \rightarrow -1 \leq 1 - 2r\sin^2\frac{k\Delta x}{2} &\leq 1 \\ \longrightarrow -2 \leq -2r\sin^2\frac{k\Delta x}{2} &\leq 0 \\ \Rightarrow 0 \leq r\sin^2\frac{k\Delta x}{2} &\leq 1 \end{aligned} \tag{2.60}$$

since $0 \leq \sin^2\theta \leq 1$, the above condition can be further simplified.

$$0 \leq r = \left(\frac{c\Delta t}{\Delta x}\right)^2 \leq 1 \tag{2.61}$$

The final stability condition became:

$$c\Delta t \leq x \tag{2.62}$$

which is known as the *Courant* stability condition [40].

2.3.2 Boundary Conditions

There are several boundary conditions. First, the Dirichlet condition addresses the specific condition where the values at the boundary are the same, such as $u_1 = u_N$ =some value (usually zero). Second, the Neumann condition occurs when derivatives at the boundary are the same, such as $\frac{\partial u}{\partial x}|_1 = \frac{\partial u}{\partial x}|_2$. Third, the absorbing boundary condition assumes that waves traveling outward will disappear, and is expressed as follows:

$$\frac{\partial u}{\partial t} = -c\frac{\partial u}{\partial x} \tag{2.63}$$

This is also called an advection equation, describing that a scalar field, u(x,t) moves outward from the boundary by a flow of constant speed c. In other words, when the wave hits this boundary with the absorbing condition, the wave will pass through this boundary but not return to it as if the boundary absorbs the wave.

The general solution for this absorbing condition is as follows:

$$u = u_0(x - ct) \tag{2.64}$$

where u_0 could be any arbitrary function.

The last boundary condition discussed, which is the main focus of this thesis, is the dielectric multilayer boundary condition, where two different dielectric layers are interfacing each other. Basically, continuity of an electric field or magnetic field at the interface is the condition stated here:

2.3.3 2D wave equation

The one dimensional wave equation can be easily expanded to a two dimensional equation. The stability criterion will be as follows:

$$c\Delta t \leq \frac{1}{\sqrt{\frac{1}{\Delta x^2} + \frac{1}{\Delta y^2}}} \tag{2.65}$$

The absorbing boundary condition also will be changed slightly for a two-dimensional case:

$$\frac{\partial u}{\partial t} = -c\left(\frac{\partial u}{\partial x} + \frac{\partial u}{\partial y}\right) \tag{2.66}$$

The main equation to be solved is Maxwell's equation:

$$-\frac{\partial}{\partial t}\mu\overrightarrow{H} = \overrightarrow{\nabla} \times \overrightarrow{E} \tag{2.67}$$

This equation is then divided into three equations:

$$\begin{aligned} -\frac{\partial}{\partial t}\mu H_x &= \frac{\partial E_z}{\partial y} - \frac{\partial E_y}{\partial z} \\ -\frac{\partial}{\partial t}\mu H_y &= \frac{\partial E_x}{\partial z} - \frac{\partial E_z}{\partial x} \\ -\frac{\partial}{\partial t}\mu H_z &= \frac{\partial E_y}{\partial x} - \frac{\partial E_x}{\partial y} \end{aligned} \tag{2.68}$$

Likewise, one can derive three separate equations from another Maxwell's equation:

$$-\frac{\partial}{\partial t}\epsilon\overrightarrow{E} = \overrightarrow{\nabla} \times \overrightarrow{H} \tag{2.69}$$

This equation is then divided into three equations:

$$\begin{aligned} -\frac{\partial}{\partial t}\epsilon E_x &= \frac{\partial H_z}{\partial y} - \frac{\partial H_y}{\partial z} \\ -\frac{\partial}{\partial t}\epsilon E_y &= \frac{\partial H_x}{\partial z} - \frac{\partial H_z}{\partial x} \\ -\frac{\partial}{\partial t}\epsilon E_z &= \frac{\partial H_y}{\partial x} - \frac{\partial H_x}{\partial y} \end{aligned} \tag{2.70}$$

For the dielectric-dielectric boundary conditions, E_{tan} and H should be continuous [41]. One can discretize the above six equations into final 2D FDTD equations. An example can be written as follows:

$$\begin{aligned} H_z(i,j,t+1) \quad &= H_z(i,j,t) - \tfrac{1}{\mu}\tfrac{\Delta t}{\Delta x}\left[E_y(i+1,j,t) - E_y(i,j,t)\right] \\ &\quad + \tfrac{1}{\epsilon}\tfrac{\Delta t}{\Delta y}\left[E_x(i,j+1,t) - E_x(i,j,t)\right] \end{aligned} \tag{2.71}$$

where i and j stand for spatial terms, and t for time.

2.3.4 Real simulation results

The problem here to be solved concerns optical beam propagation through multi-layered dielectric films. In particular, the dielectric boundary condition applies to each boundary at the interface, and also an absorbing boundary condition applies to each far end

(bottom, top, left and bottom). If a certain wavelength is selected, one can simulate total reflection, as if light barely contacts the bottom.

Figure 2.6 shows simulation results from an optical FDTD process. The left side of each figure represents a multilayered structure similar to the multilayer addressed in this thesis. The blue layer stands for the low refractive index material, in which case SiO_2 was chosen (n_{SiO_2} is around 1.3), while the red layer is referred as the high refractive index material, in which TiO_2 was selected (n_{TiO_2} is around 1.96).

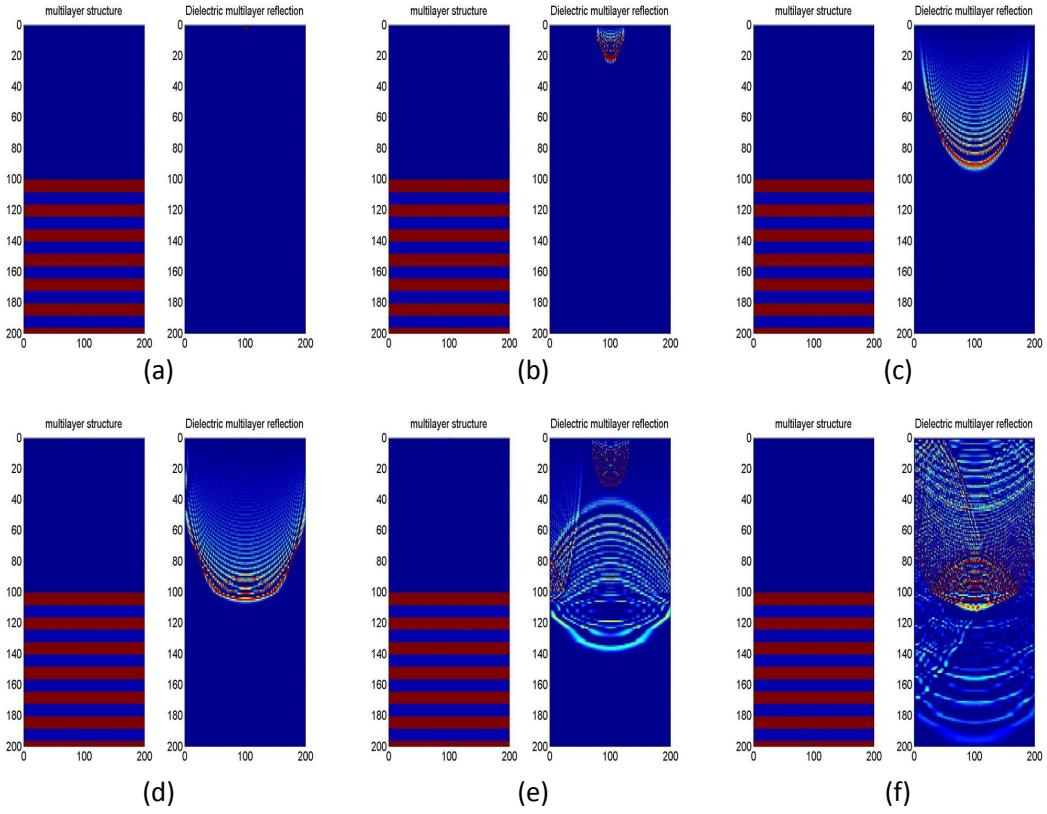

Figure 2.6: Simulation results for FDTD in nm scale with (a) at initial time, (b), (c), (d), (e), and (f) at transient time. All the figures are in the order of time.

This simulation shows that seven paired multilayers can behave as a single optical mirror. Figure 2.6(a) shows the initial state and Fig. 2.6(b) occurs when the light has just launched. Figure 2.6(c) shows how the light propagates toward the multilayer

structures. Finally, the light hits the first interface at the TiO_2 layer in Fig. 2.6(d) and Fig. 2.6(e) shows the progress. The final figure 2.6(f) shows that only little light contacts the bottom of the multilayer, demonstrating that almost all of the light is reflected. The absorbing boundary condition was applied to the left and right corners.

Chapter 3

Heat Transfer Modeling and Simulation

This chapter is mainly extracted from the following reference, written in preparation for journal submission [42].

3.1 Theory of heat transfer

3.1.1 Basic heat equation

The thermoluminescent dielectric thin films in this dissertation exhibit two different aspects of physics. The first aspect is heat transfer, specifically where the heat generated by other devices such as laser or micro-heaters is transferred through TL materials. The second aspect is thermoluminescence, in which light energy is converted by heat transfer with TL materials, according to band gap theory. This chapter focuses on the first aspect, heat transfer modeling.

There are three different heat transfer mechanisms. First, the term *heat conduction*, often called diffusion, refers to the thermal energy transfer through a material without bulk movement of the material. When the temperature of a substance is different from another body or its ambient, heat flow occurs so that the body and the ambient reach the same temperature, whose status is often called thermal equilibrium. Second, the term *heat convection* refers to thermal energy transfer in a moving fluid (liquid or gas).

Convection occurs when mass flow of a fluid (liquid or gas) conveys heat along with the flow of matter in the fluid. Generally speaking, convection consists of two different types, forced convection and natural convection. Forced convection occurs when a fluid is forced to flow by an external force, for example, a fan. Natural convection occurs due to buoyancy, where hot fluid rises since it has a lower density than cold fluid. The third case of heat transfer is *thermal radiation*, in which all surfaces of finite temperature emit energy in the form of electromagnetic waves. Hence, even without an intervening medium, there is a net heat transfer by radiation between two surfaces at different temperatures [43].

Thermal radiation is not addressed in this thesis, since the main mechanism between dieletric materials is the conduction. The convection is concerned with a boundary condition in this thesis because a TL layer is facing air which is a moving fluid.

For this study, we use thermoluminescent multilayers consisting of LiF:Mg,Ti and CaF_2:Dy for temperature sensor applications where thermal history needs to be reconstructed. Heat transfer modeling can make it possible to derive the thermal profile of each TL layer upon laser heating. This temperature as function of time would feed into a TL model to estimate the final luminescence intensity, which will be discussed in the next chapter.

The CaF_2:Dy surface of the TL multilayer is coated with aluminum, which serves as an absorption layer when the multilayer is heated by a Nd:YAG laser. The heat penetrates the multilayer over a period of time that depends on the multilayer thickness, diffusivity, and the thermal contact conductance of any interlayers. This process empties some of the filled traps, which alters the thermoluminescence that will be observed afterwards.

A heat transfer simulation has been used to estimate the temperature distribution in the structure. This temperature as a function of time feeds into a TL simulation, which estimates the trap depopulation and resulting TL glow curves. The heat transfer simulation assumes one-dimensional conduction. Furthermore, the multilayer is considered to be thin compared to its width, and the laser beam is assumed to be uniform over the entire surface so lateral heat conduction can be ignored. Figure 3.1 shows the diagram of this heat transfer model. The positive x direction penetrates into the multilayer with zero from the Al-CaF_2:Dy boundary:

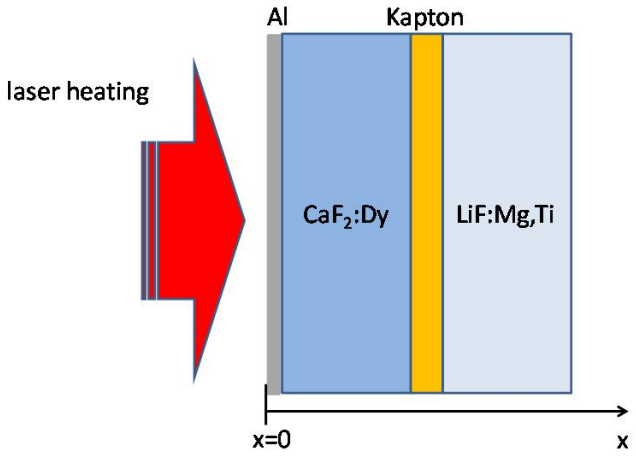

Figure 3.1: Diagram of heat transfer modeling for the TL multilayers having Al, CaF_2:Dy, Kapton tape, and LiF:Mg,Ti

One approximation has been made for simplification; the size of the multilayer is big enough compared to its thickness so that each layer at a certain thickness should have a uniform lateral temperature at any given time so that there is no lateral heat dissipation. This approximation can make the heat diffusion equation a one-dimensional equation. Figure 3.1 shows the diagram of this heat transfer model.

The heat diffusion equation is as follows [43]:

$$\frac{\partial}{\partial x}\left(k\frac{\partial T}{\partial x}\right)+\dot{q}=\rho c_p\frac{\partial T}{\partial t} \tag{3.1}$$

where k is thermal conductivity, ρ is mass density, c_p is specific heat, $\dot{q}$ is the rate at which energy is generated per unit volume of the medium (W/m^3), and T is temperature (°C).

We consider a simpler case which does not have heat generation, as follows:

$$\frac{\partial}{\partial x}\left(k\frac{\partial T}{\partial x}\right)=\rho c_p\frac{\partial T}{\partial t} \tag{3.2}$$

We assume that k=k(x) because the multilayer is heterogeneous and of finite thickness. Then, (3.2) will be:

$$\frac{\partial k}{\partial x}\frac{\partial T}{\partial x}+k\frac{\partial^2 T}{\partial x^2}=\rho c_p\frac{\partial T}{\partial t} \tag{3.3}$$

Introducing $\alpha = k/\rho c_p$ where α is thermal diffusivity, the above equation can be simplified as:

$$\frac{\partial T}{\partial t} = \frac{\partial \alpha}{\partial x}\frac{\partial T}{\partial x} + \alpha\frac{\partial^2 T}{\partial x^2} \tag{3.4}$$

where T_{pulse} means pulsed temperature from the laser heating that is applied to the Al side in Figure 3.1.

3.1.2 Boundary and initial conditions

To solve (3.4), boundary and initial conditions have to be provided. The first condition at t=0 would be:

$$T(x) = T_\infty \tag{3.5}$$

where T_∞ means room temperature. Also, the boundary condition at x=0 will be:

$$\left.\frac{\partial T}{\partial x}\right|_{x=0} = 0 \; and \; T\Big|_{x=0} = T_{pulse} \tag{3.6}$$

Since LiF:Mg,Ti would be exposed to air, the last boundary condition at x=L addresses heat convection, as follows:

$$k\left.\frac{\partial T}{\partial x}\right|_{x=L} = h(T - T_\infty) \tag{3.7}$$

3.2 Finite Difference Time Domain Method of Heat Transfer

Even though the heat equation with these conditions appears simple, solving this equation analytically is quite difficult. There are several methods that can be used (3.4). First, a thermal resistance model can be used where each layer is thought of as a simple resistance, and a circuit network calculation can be performed to extract the static thermal distribution [43] However, this method only works when the system reaches a steady state, so it is not appropriate for our analysis.

The second method would use a lumped capacitance, where heat conduction within an object or single layer occurs much faster than heat conduction across the boundary of the object. In other words, temperature within the object is assumed to be completely uniform in space but fluctuating over time. However, this approach also gives a final

equation having no function of thermal conductivity, depending only on air convection, density, and layer thickness. In this paper, the thermal conductivity and diffusivity of each layer are quite important.

Numerical methods were also proposed using the alternating-direction-implicit method, which is a finite difference method for solving parabolic and elliptic partial differential equations [44, 45].

3.2.1 Finite different method of heat transfer

The method used in this paper is a FDTD (Finite Difference Time Domain) method, where the above heat equation (3.4) is discretized in the following form:

$$\begin{aligned} \frac{\partial T}{\partial t} &= \frac{\partial \alpha}{\partial x}\frac{\partial T}{\partial x} + \alpha\frac{\partial^2 T}{\partial x^2} \\ \frac{T_m^{p+1} - T_m^p}{\Delta t} &= \frac{\alpha_{m+1} - \alpha_m}{\Delta x}\frac{T_{m+1}^p - T_m^p}{\Delta x} + \alpha_m \frac{T_{m+1}^p + T_{m-1}^p - 2T_m^p}{(\Delta x)^2} \end{aligned} \tag{3.8}$$

where superscript p stands for time domain (not an exponential term), and m for spatial domain. Therefore, p+1 refers to the temperature after p time and m+1 refers to the location next to m. By introducing a new term called the Fourier dimensionless number (Fo), $Fo = \alpha\Delta t/(\Delta x)^2$, the above equation can be further simplified as:

$$\begin{aligned} T_m^{p+1} &= T_m^p + (Fo_{m+1} - Fo_m) \times (T_{m+1}^p - T_m^p) + Fo_m(T_{m+1}^p + T_{m-1}^p - 2T_m^p) \\ &= Fo_{m+1}T_{m+1}^p + (1 - Fo_{m+1} - Fo_m)T_m^p + Fo_m T_{m-1}^p \end{aligned} \tag{3.9}$$

Fo indicates how each layer reacts against the heat transfer. In general, the larger Fo, the faster the heat can go through. It is noted that a stability condition has to be met for the above equation to be useful; that is, all the coefficients should be larger than zero. Hence,

$$\begin{aligned} 1 - Fo_{m+1} - Fo_m &\geq 0 \\ Fo_{m+1} + Fo_m &\leq 1 \end{aligned} \tag{3.10}$$

If Fo is constant, the final stability condition can be expressed as follows:

$$Fo \leq \frac{1}{2} \tag{3.11}$$

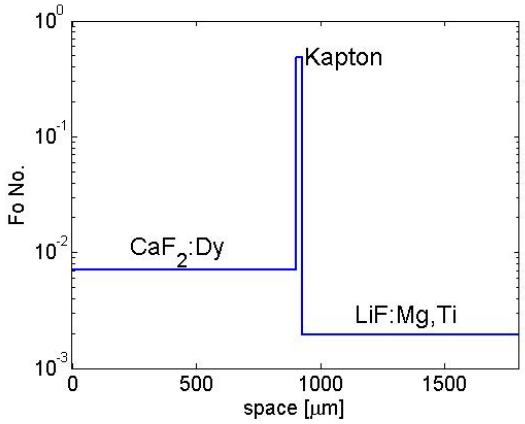

Figure 3.2: Fo property map across the TL multilayer

This condition is critical for solving the heat FDTD equation [46]; if this condition is not met, the solution will not converge. Figure 3.2 shows the overall *Fo* trend in which Kapton tape is the material with the highest thermal diffusivity. A thermal contact conductance (TCC) was introduced at the interface between CaF_2:Dy and aluminum to better match the simulation with experimental results, as shown in Figure 3.3. The material properties of each layer are shown in Table 3.1.

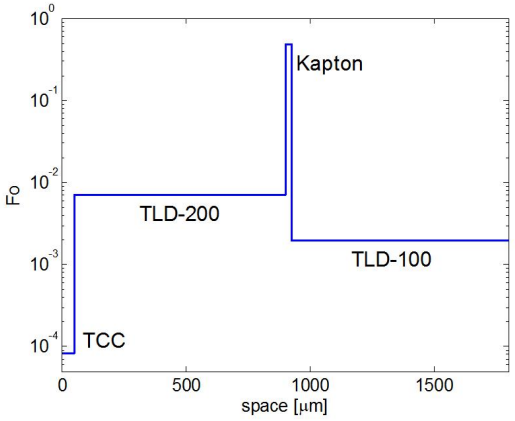

Figure 3.3: Fo property map across the TL multilayer with TCC

Boundary and initial conditions in FDTD

Initial condition at t=0 is the same as described in the previous section 3.1.2. The boundary condition at x=0 is the Neuman condition where the surface heat is generated:

$$\forall p,\ T^p_{m=1} = T^p_{m=2} \tag{3.12}$$

$$\forall p,\ T^p_{m=1} = T_{pulse} = T(t) \tag{3.13}$$

where T_{pulse} is surface temperature generated by laser. On the other hand, the B.C. at x=L (where L is total layer thickness) will be as follows:

$$\forall p,\ -k\frac{T^p_M - T^p_{M-1}}{\Delta x} = h(T^p_M - T_\infty) \tag{3.14}$$

where M corresponds to the integer indicating the total length (L). Introducing a new term called *Biot* number for FDTD ($Bi = h\Delta x/k$), (3.13) will be simplified as follows:

$$\begin{aligned} -T^p_M + T^p_{M-1} &= Bi(T^p_M - T_\infty) \\ \Rightarrow (Bi+1)T^p_M &= T_{M-1} + BiT_\infty \\ \Longrightarrow T^p_M &= \frac{T_{M-1} + BiT_\infty}{Bi+1} \end{aligned} \tag{3.15}$$

3.3 Heat Transfer Simulation on multi-layered dielectric films

This thesis places high focus on heat transfer into multi-layered dielectric films, since thermal material properties, such as thermal conductivity, are quite important. Table 3.1 shows the summary of the thermal properties of each dielectric material. Since the TL multilayer is facing with air, the property of air is also considered for heat convection, as well as TCC modeling because we determine the parameters of a TCC layer by combining the properties of air and CaF_2:Dy .

Figure 3.4 shows the simulated temperature conditions experienced by the TL multilayer samples. For comparison, there are two distinct cases shown here. The case for a

Table 3.1: Thermal properties of each material for heat transfer simulation

Properties	LiF (TLD-100)[a]	CaF_2 (TLD-200)[b]	Kapton[c]	Air[d]
Density(Kg/m^3)	2639	3180	1420	1.127
Thermal conductivity(W/mK)	4.01	9.71	0.12	0.0271
Specific heat(J/KgK)	1604	887.6	1.09	1.005
Thickness(μm)	890	890	30.4	N/A

[a] is from [47, 48].
[b] is from [49].
[c] from [50].
[d] from [51].

laser heating pulse of 250 ms, which can be regarded as short pulse, is shown in Figure 3.4(a)-(c) while the case for a long pulse of 1000 ms is shown in Figure 3.4(d)-(f).

Figure 3.4(b) and (e) indicate the maximum temperature profile across the TL multilayer. Figures 3.4(c) and (f) indicate the temperature profile at each layer in the time domain. The short pulse seems to have a different profile between the two TL materials, while the longer pulse has a more similar temperature profile. The temperature profiles shown in Figures 3.4(c) and (f) were obtained from the center of each layer. This temperature profile, temperature as function of time, feeds into a TL model to achieve the final emission intensity, which will be discussed in chapter 7.

Here is another case where heating temperature is at 480 °C as shown in Figure 3.5. It is expected that the higher the temperature, the more depopulation occurs, resulting in the lower emission intensity later with TL experiment. Although heating may generate different thermal distributions, the thermal slope, dT/dx remains quite similar because it is determined by the diffusivity of the multilayer, which should remain the same.

Once the TCC is introduced into this FDTD simulation, the graphs look quite different. The temperature drops significantly where the TCC is located as if TCC blocks heat transfer. This case is shown in Figure 3.6, which is the final simulation result matching the experimental one; these results will be discussed later.

FDTD simulation can give us real-time trends, and Figure 3.7 illustrates a few special cases in which the heating pulse of 250 ms and 480 °C is applied. Figure 3.7 (a) shows

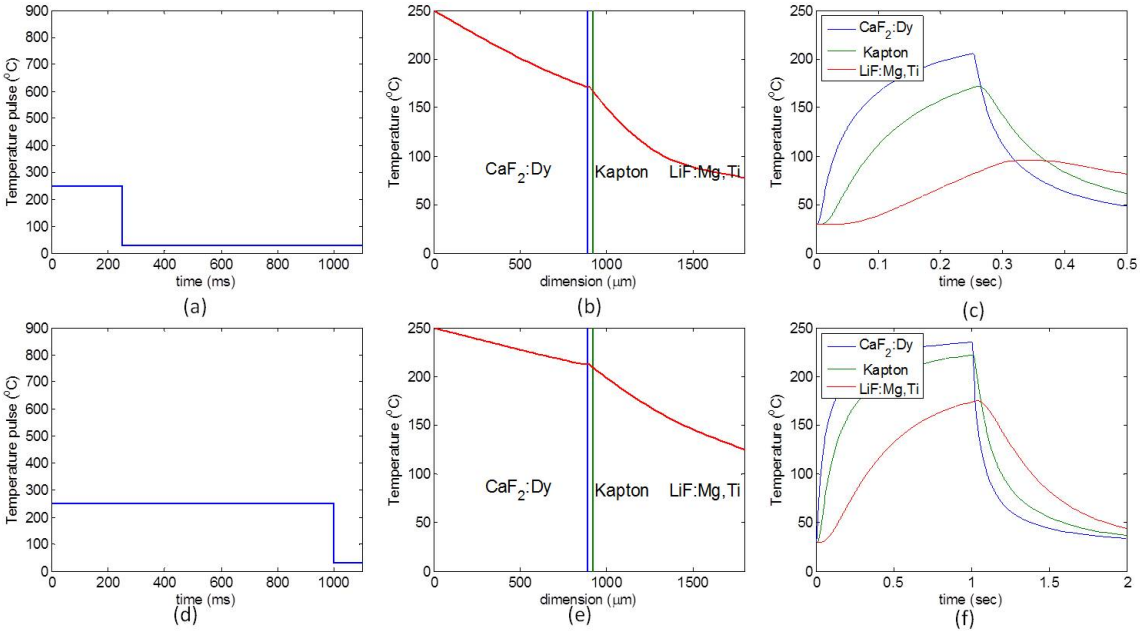

Figure 3.4: Temperature pulse comparison for 480 °C laser pulse without TCC (a)-(c) for 250ms pulse and (d)-(f) for 1000ms pulse. (a) and (d) show pulse time, (b) and (e) are maximum temperature profile in temporal domain, (c) and (f) shows temperature profile for each layer in time domain. It is noted that thermal profiles shown in (c) and (f) were derived from the middle thickness of each layer

the 0 ms case that is initial condition with no heating. 2.5 ms is shown in fig. 3.7(b), which is immediately after 480 °C heating is applied; therefore, CaF_2:Dy or TLD-200 starts being heated. Figure 3.7(c) and (d) show 122.45 ms and 247.41 ms, respectively. Moreover, Figure 3.7(e) shows the case after heating is turned off so that the boundary near CaF_2:Dy starts dropping off its temperature. Finally, Figure 3.7(f) shows the final time when almost all the layers have reached room temperature. In this way, one can generate a movie of how heat propagates through each layer.

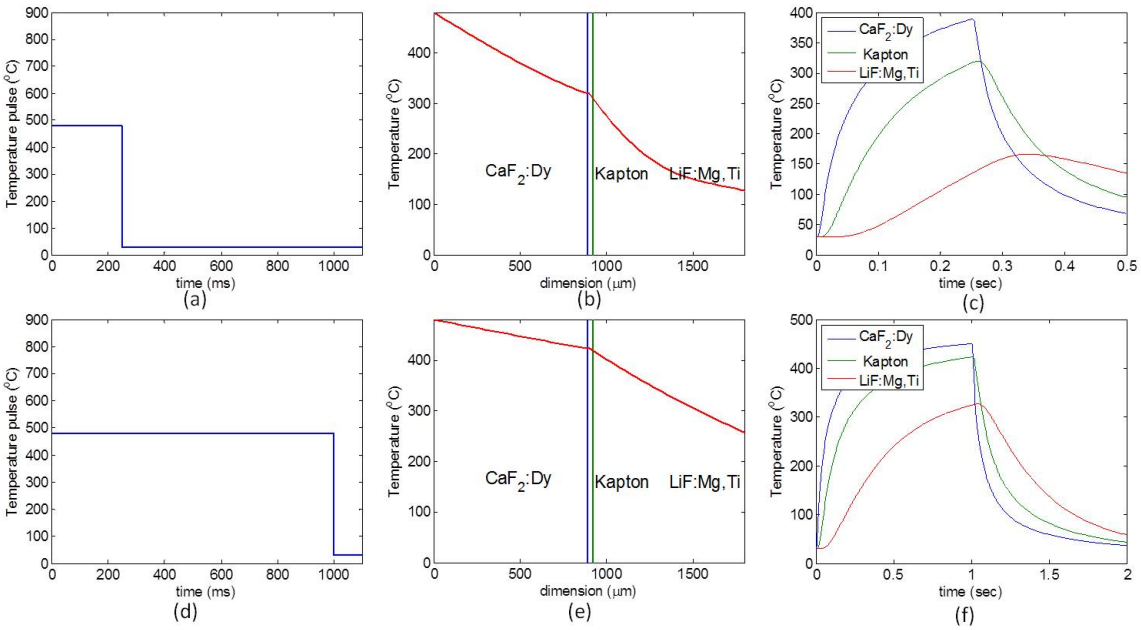

Figure 3.5: Temperature pulse comparison for 480 °C laser pulse without TCC (a)-(c) for 250ms pulse and (d)-(f) for 1000ms pulse. (a) and (d) show pulse time, (b) and (e) are maximum temperature profile in temporal domain, (c) and (f) shows temperature profile for each layer in time domain. It is noted that thermal profiles shown in (c) and (f) were derived from the middle thickness of each layer

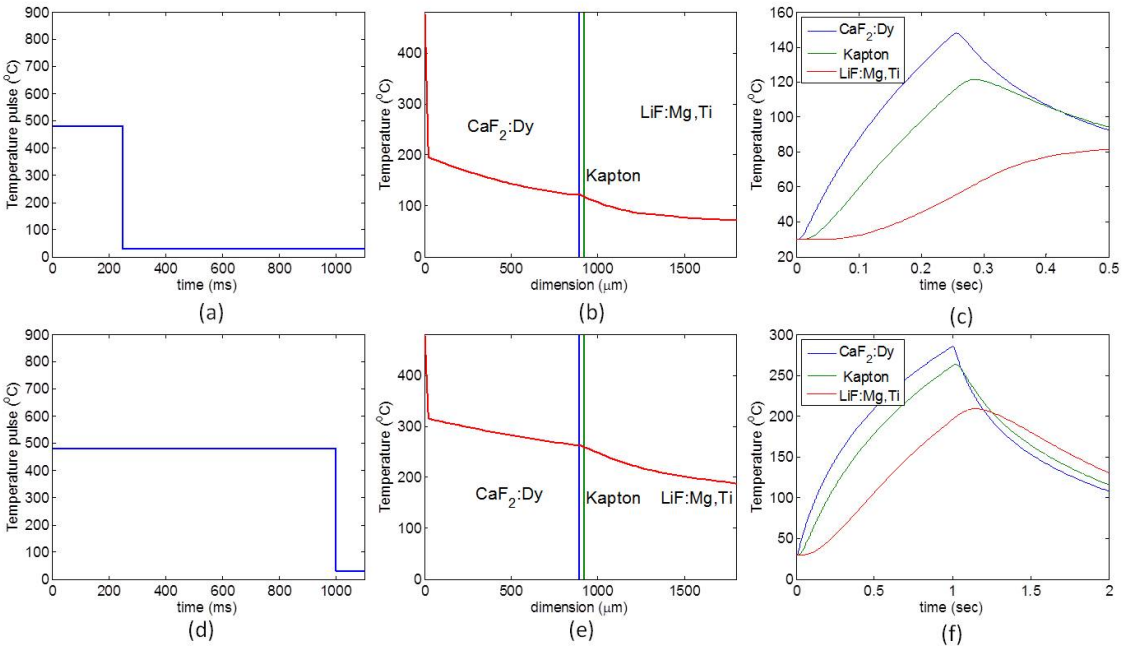

Figure 3.6: Temperature pulse comparison for 480 °C laser pulse with TCC (a)-(c) for 250ms pulse and (d)-(f) for 1000ms pulse. (a) and (d) show pulse time, (b) and (e) are maximum temperature profile in temporal domain, (c) and (f) shows temperature profile for each layer in time domain. It is noted that thermal profiles shown in (c) and (f) were derived from the middle thickness of each layer

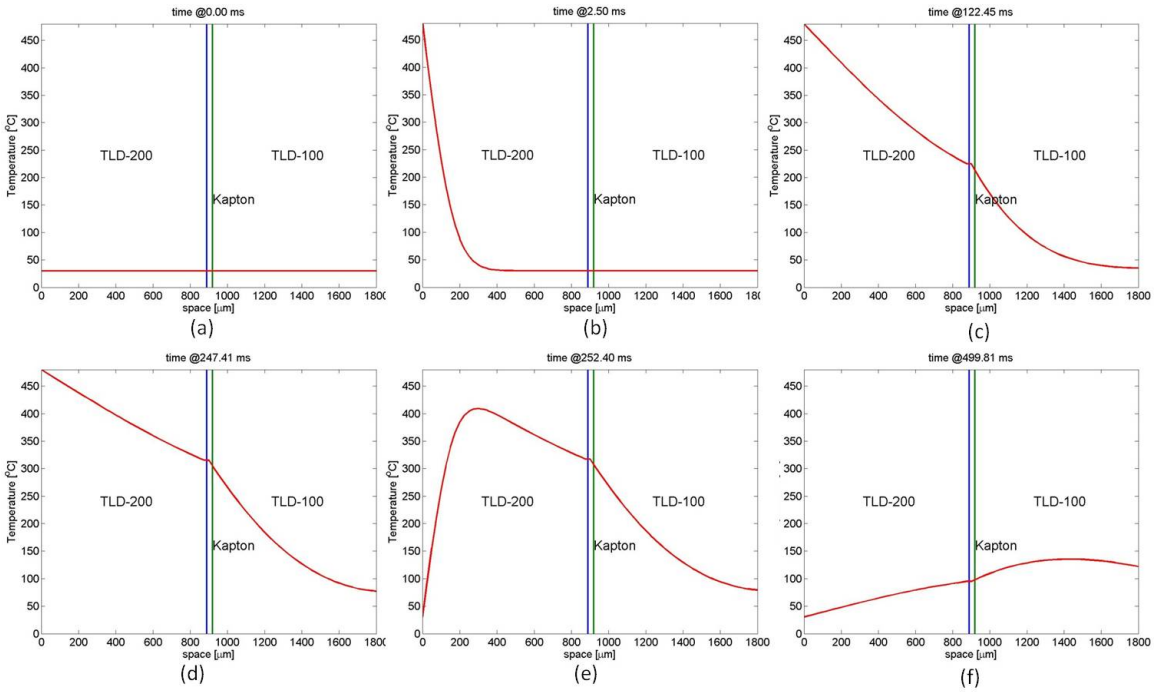

Figure 3.7: Thermal profile of TL multilayer with 480 °C heating pulse; (a) at 0 ms with no heating, (b) at 2.5 ms, (c) at 122.45 ms, (d) at 247.41 ms, (e) at 252.40 ms, and (f) at 499.81 ms, respectively

Chapter 4

Theory of thermoluminescence

This chapter addresses the theory of thermoluminescence, beginning with a general overview and then elaborating on its application for temperature sensors.

4.1 Introduction to thermoluminescence

When radiation is incident on an object material, part of its energy can be absorbed or re-emitted in the form of light of a longer wavelength by Stoke's Law. This is called the luminescence process. The wavelength of the emitted light is characteristic of the luminescent object not of the incident radiation [1].

A variety of luminescences have their own names reflecting the type of radiation used to excite the emission. The luminescences excited by radiation are *photoluminescence* (excited by ultra-violet or optical light), *radioluminescence* (nuclear radiations such as X-rays, γ-rays, and β-particles), and *cathodoluminescence* (electron beam). Besides of radiated excitation, chemical energy (*chemiluminescence*), mechanical energy (*triboluminescence*), electrical energy (*electroluminescence*), biochemical energy (*bioluminescence*) and even sound waves (*sonoluminescence*) can also create the luminescence [1].

A light emission occurs in a characteristic time named τ_c after the radiation absorption. This time enable us to categorize the luminescence process, as in Figure 4.1. Therefore, we can differentiate between *fluorescence*, where $\tau_c < 10^{-8}s$, and *phosphorescence*, where $\tau_c > 10^{-8}s$ [1]. The case where $\tau_c < 10^{-8}s$ delivers a essential definition

for the spontaneous process of fluorescence emission. The fluorescence emission occurs simultaneously with the absorption of radiation and stops immediately when the radiation ends. On the other hand, phosphorescence has a delay between the absorption of a radiation and the time [1]. The thermoluminescence can be explained as a case of phosphorescence with long period of τ_c as depicted in Figure 4.1.

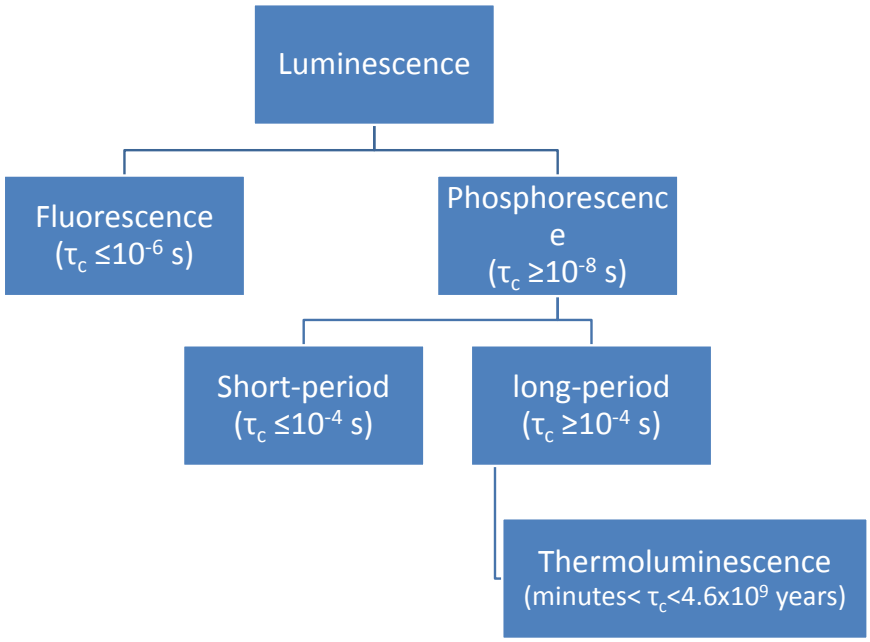

Figure 4.1: The family tree of luminescence phenomena [1].

In general, the transfer of energy from radiation to the electrons of the solid can define the luminescence emissions, thus bringing the electrons from a ground state **g** to an excited state **e** (transition (i) in Figure 4.2 (a)). The emission of a photon happens when an excited electron comes back to its ground state (transition (ii)). Thus, for the case of fluorescence, the delay between transitions (i) and (ii), is less than 10^{-1} s. On the other hand, Figure 4.2 (b) shows that the energy level diagram is modified by the presence of a metastable level **m** in the forbidden energy gap between **e** and **g**. An electron excited from **g** to **e** can now be captured at **m** level where it will dwell until it receives enough energy **E** to return to **e** from where it can encounter a normal transition back to **g**, with the ensuing emission of light. Therefore, the delay in phosphorescence is in line with the time the electron spends in the electron trap **m** [1]. According to

thermodynamic explanation, the mean time spent in the trap at temperature T can be expressed as follows:

$$\tau = s^{-1} exp\left(\frac{E}{kT}\right) \tag{4.1}$$

where s is a constant, E is the energy difference between **m** and **e** (named the trap depth), and k is Boltzmann's constant. Therefore, the phosphorescence process is exponential function of temperature [1].

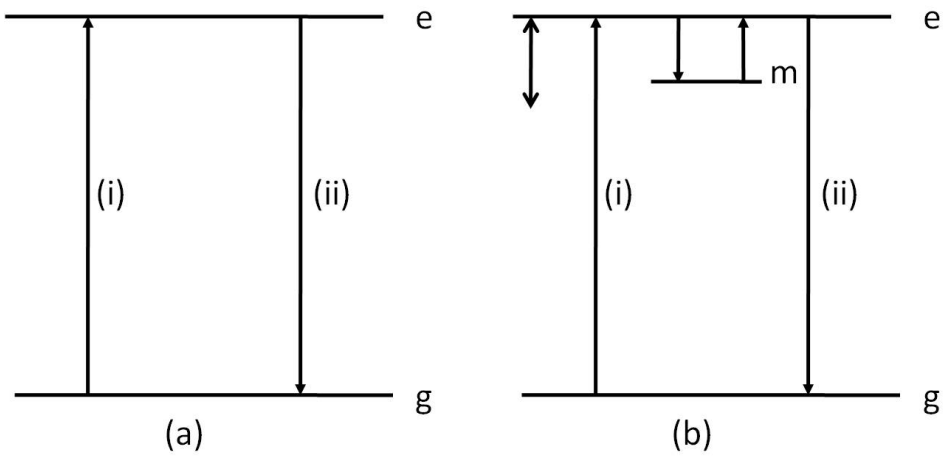

Figure 4.2: Energy transition diagrams involved in (a) fluorescence and (b) phosphorescence. It is noted that for simplicity only one m level is depicted in (b) but a number of different m levels can exist practically

4.2 Basic Principle of thermoluminescence

Figure 4.3 shows how the TL happens in the band of a material. First the temperature is increased with a heating sources, such that the trapped electrons are excited to a conduction band. Then, the electrons and holes will recombine at the luminescence center that will emit photons as relaxation, as shown in Figure 4.3:

In order to model thermoluminescence, one can start with a simple kinetic equation describing the thermodepopulation process of the filled traps [52]. Basically, the density of traps will be a function of temperature as:

$$\frac{\partial n(E,t)}{\partial t} = -n(E,t) v_{th} \sigma N_c \exp -\frac{E}{kT(t)} \tag{4.2}$$

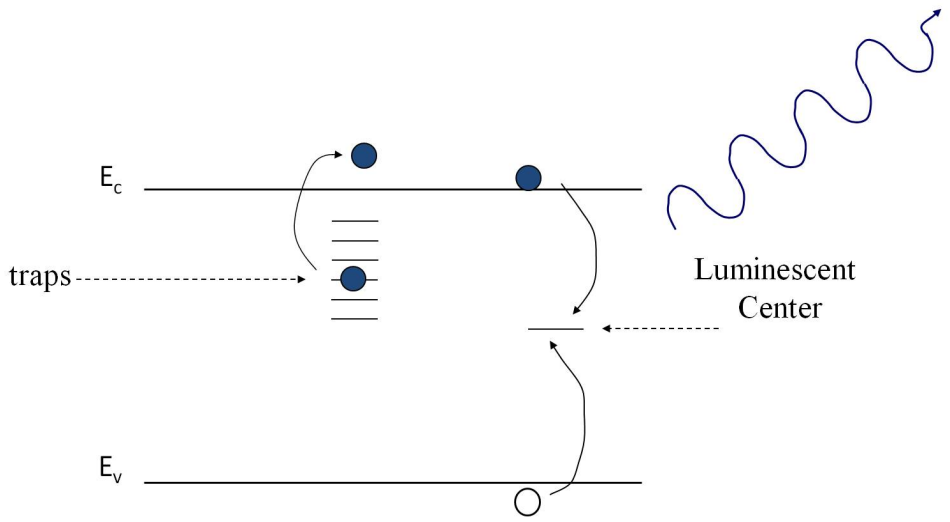

Figure 4.3: Energy transition diagrams for TL

where *n(E,t)*is the density of the traps, v_{th} is the mean value of the thermal velocity, σ is the electron capture cross section of the traps, N_c is the effective conduction band state density, n_0 is the initial density of the traps, E is the energy depth of the traps from the edge of the conduction band, t is time of thermal treatment, k is Boltzmann's constant, and T(t) is temperature (K).

Integrating 4.2 will result in the following equation:

$$n(E,t) = n_0(E) \exp\left[-\int v_{th}\sigma N_c \exp\left(-\frac{E}{kT(t)}\right)dt\right] \tag{4.3}$$

where the temperature is the function of time as follows

$$T(t) = T_R + (T_{peak} + T_R)\exp\left(-\frac{t}{\tau_c}\right) \tag{4.4}$$

The probability that an electron will escape from the trap at some temperature is given by [53].

$$p = S\exp\left(-\frac{E}{kT}\right) \tag{4.5}$$

where E is the trap depth and S a frequency factor. For the conditions described above, the rate of release of electrons from the traps is given by the first-order kinetics equation:

$$\frac{dn}{dt} = -np = -nS\exp\left(-\frac{E}{kT}\right) \tag{4.6}$$

where n is the number of trapped electrons. On integration of the above equation:

$$n = n_0 \exp\left[-\frac{S}{\beta}\int_{T_0}^{T} \exp\left(-\frac{E}{kT}\right)dT\right] \tag{4.7}$$

where $\beta = dTdt$ is the heating rate, and n_0 is the initial concentration of electrons in the traps. The intensity of luminescence I is determined by the rate of arrival of electrons at the luminescence centers:

$$I = -C\frac{dn}{dt} = CS \times n \exp\left(-\frac{E}{kT}\right) \tag{4.8}$$

where C is a constant related to luminescence efficiency. The equation describing thermoluminescence with first order kinetics is then:

$$I = CSn_0 \exp\left(-\frac{E}{kT}\right) \exp\left[\left(-\frac{S}{\beta}\right)\int_{T_0}^{T} \exp\left(-\frac{E}{kT}\right)dT\right] \tag{4.9}$$

For the case of equal retrapping and recombination probabilities:

$$\frac{dn}{dt} = -n^2 S \exp\left(-\frac{E}{kT}\right) \tag{4.10}$$

and is termed second-order kinetics which is not of interest in this thesis. The untrapping of electrons is not limited to first- or second-order kinetics but may follow a general order [53], [54]. From the equation (4.9) one can manipulate or simulate the real TL glow curve that most TL materials generate if β,E_0 and S are given.

There are various methods for evaluating the trapping parameters from TL glow curves. One of the glow peaks is highly isolated from the others; the experimental methods such as initial rise, various heating rates, and peak shape methods, are suitable methods to determine them [55, 1].

4.3 Ideal simulation

In order to optimize the TL materials as temperature sensors, we must examine how the light output curves of an ideal system vary as a function of temperature. For simplicity, we will start with the TL of a crystal with a bandgap of 6eV with a series of 10 trap bands near an energy depth of 1.4eV. Each trap band has a Gaussian energy width of 0.05eV (approximately 2kT at room temperature) and is separated by 0.05eV, as

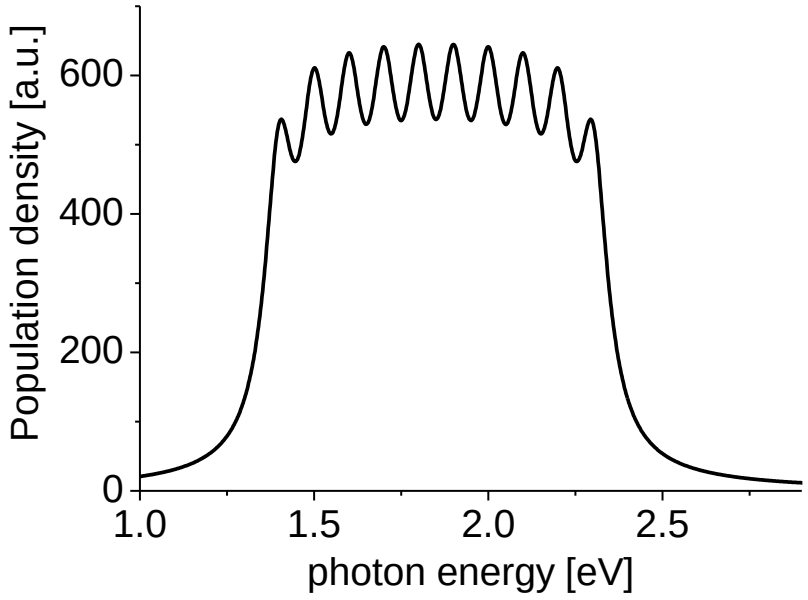

Figure 4.4: Trap density profile with 10 separate traps for an ideal simulation. Each trap band has a Gaussian energy width of 0.05 eV and is separated by 0.05 eV.

shown in Figure 4.4. If every trap is filled initially and then the particle is exposed to a sudden jump in temperature followed by a slow cool (30 sec time constant), the shallow traps will be preferentially emptied. Figure 4.5 compares thermoluminescence intensity versus the temperature of two particles: one that experienced a peak temperature of 300°C and one that experienced a peak temperature of 310°C. Figure 4.6 is a close-up of the temperature region of interest. Note the clear differences between the two curves. In comparing figures 4.4 and 4.5, we realize that the ability to compare the populations of multiple trap bands gives us temperature information that is independent of the overall intensity, making temperature extraction much simpler.

Of course, finding a material with a perfectly ideal set of traps is unlikely, but the concept applies even to a non-ideal distribution of traps. For example, there are modeling techniques that can extract trap distribution and population, even though the trap distribution is nearly continuous across the gap [56]. In this program, one of the first techniques we will develop is multiple-wavelength OSL. If long wavelength light is used to excite a material, only those traps at low energies will contribute to the

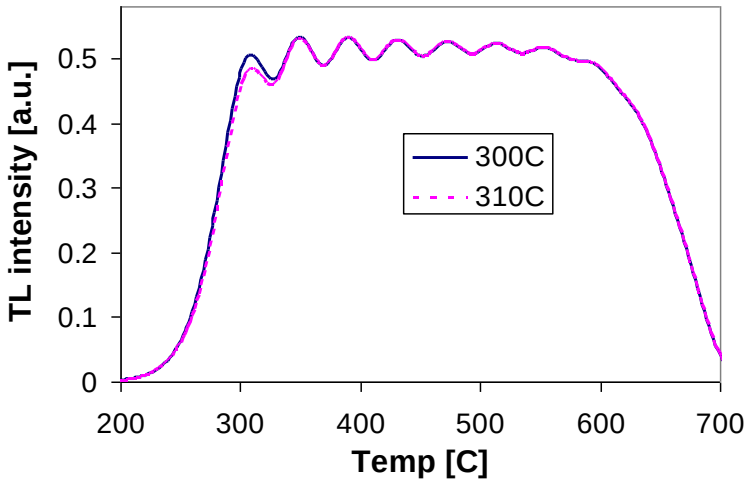

Figure 4.5: TL results of 10 ideal traps with two different cases; one is exposed to 300 °C and the other to 301 °C.

luminescence. Once these traps are significantly emptied, shorter wavelengths of light could be used to determine the population of deeper trap levels. One would expect to see some cross-talk, but the information gained would relate to population distribution much more directly than a single wavelength luminescence scan, and therefore one would expect finer temperature resolution for an agent defeat event.

4.4 Material Study and Choice

Many TL materials have been available as conventional products from Thermo Scientific [57] for dosimetry applications. Table 4.1 shows the summary of TL materials based on their TL peak temperatures and emission wavelength.

4.4.1 Theory and background on LiF:Mg,Ti

The most widely used and also most extensively studied material is LiF:Mg,Ti (TLD-100) marketed by Harshaw Chemical Company which is now ThermoFisher Inc. TLD-100 consists of LiF doped with about 170 ppm Mg^{2+} ions and about 7 ppm Ti^{4+} ions.

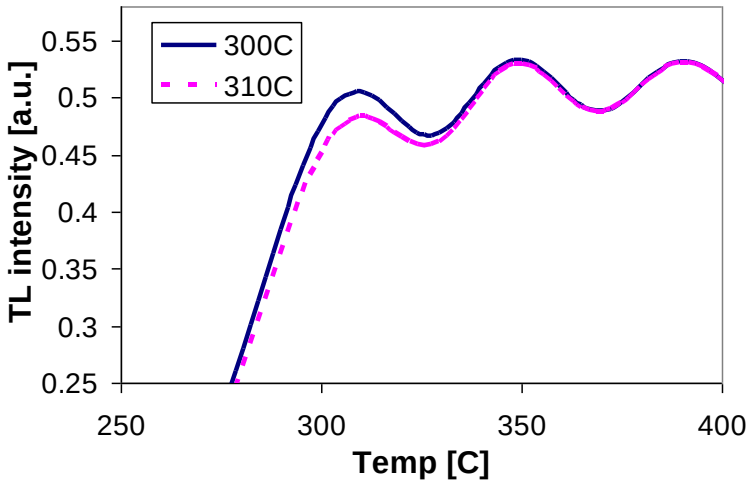

Figure 4.6: Zoom-in TL results for 10 ideal traps using first order kinetics model

The Mg^{2+} ions are believed to be related with the trapping of electrons while the Ti^{4+} ions with the recombination process [53]. The glow curve of the LiF:Mg,Ti is composed of five peaks varying from room temperature to 230°C. Peaks 2 and 3 have been involoved with Mg^{2+} and cation vacancy pairs and peaks 4 and 5 with higher-order clusters of dipoles, maybe trimers [53].

A typical glow-curve for LiF:Mg,Ti is shown in Figure 4.7. The temperature at which the peak maximum appears is related to the trap depth. In Figure 4.7, four peaks (2-5) are shown indicating that four different species of trap are being activated within this particular temperature range, each with its own value of **E** and **s**. In general the larger the value of E, the higher the temperature at which the peaks will occur [1]. The glow curve of LiF:Mg,Ti is resolved into the component first order glow peaks and also heating rate is 0.5 °C/s[53].

Many peaks overlapped each other because their full width at half maximum (FWHM) is sometimes so big that it is hard to separate each peak. In general, the deconvolution method is applied to achieve the proper E and s for each peak, as shown in Figure 4.7 [60].

In addition, peaks 2 and 3 are associated with the impurity-cation vacancy dipoles.

Table 4.1: TLD Materials chart

Materials	TL (°C)	$\lambda_{emission}$(nm)	Remarks
LiF:Mg,Ti (TLD-100)	210, >300	400	[58]
CaF_2:Dy (TLD-200)	120, 140, 210, 250	<450, 500-550	[58]
LiF:Mg,Cu,P (TLD-100H)	220	400-490	[59]
α-Al_2O_3:C	180	420	[59]
$CaSO_4$:Dy (TLD-900)	220	475-570	[59]
$CaSO_4$:Tm	220	335, 350, 445	[59]
MgB_4O_7:Dy	185	475, 487, 570, 585	[59]
MgB_4O_7:Tm	185	455	[59]
$BaSO_4$:Eu	220	375, 560	[58]
Mg_2SiO_4:Tb	200, 250, 330	380, 415, 440, 490, 550, 590	[58]
Al_2O_3:Ti, Si	170, 330, 490	410, 600	[58]

As a result of migration, dipoles become aggregated and give rise to clusters of two (dimers) or three dipoles (trimers). Peaks 4 and 5 are associated with higher order cluster of Mg^{2+} -V_c^- dipoles where V_c^- means cation vacancies. The aggregates can encounter different architectures inside the host matrix ending in a precipitate phase. Heating and cooling at a variety of different rates pushes these reactions and explains general trends observed in the subsequent way. Annealing at 400°C disassembles all the Mg impurities in dipole form. Following low-temperature annealing causes to aggregate the dipoles into trimers. Slow cooling of material stimulates aggregating while material quenching causes to freeze the defect structure [60].

TL dosimetry data suggests that greater emphasis should be placed on the study of the behavior of peak 5 alone, in the hope that peak 5 will be perhaps less influenced by these clustering and precipitation reactions than peak 4, under certain conditions of experimental procedures and analysis techniques. In other words, it may be that over a certain range of cooling rates and glow curve heating rates, it will be possible to separate peak 4 from peak 5 accurately. In addition, the intensity of peak 5 will not be significantly affected by the aggregation of traps responsible for peaks 2 and 3 [60].

Furthermore, peak 6 which is not captured in Figure 4.7 can be observed sometimes at a higher temperature than peak 5. This means that the high temperature tail of peak 5 will overlap with the low-temperature tail of peak 6.

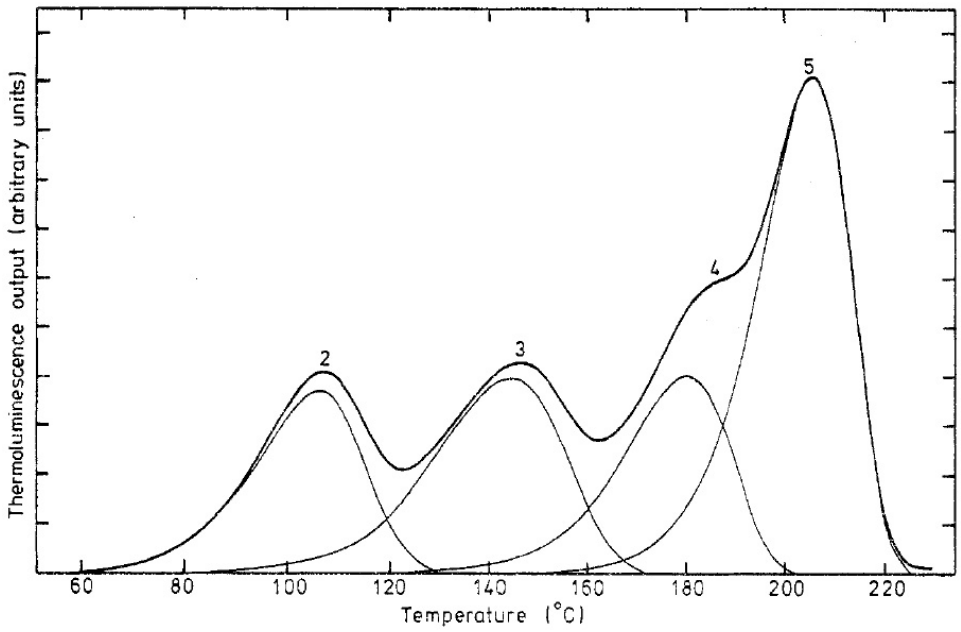

Figure 4.7: LiF:Mg,Ti glow curve from reference [53]

4.5 Thermoluminescence of LiF:Mg,Ti and CaF_2:Dy

The material properties of LiF:Mg,Ti and CaF_2:Dy are shown in Table 4.2 along with other TL materials. CaF_2:Dy was chosen because it tends to have different glow curve peaks and emission spectra from LiF:Mg,Ti, as indicated in Table 4.2. The drawback is that it is 16 times more sensitive than LiF:Mg,Ti as depicted in Figure 4.8. In other words, given the same dose radition, CaF_2:Dy emits at an intensity that is a factor of 16 higher than LiF:Mg,Ti. However this drawback can be overcome by filtering the combined emission of the two materials to select a suitable emission wavelength which balances out the intensities.

Figure 4.8 shows the typical TL versus temperature curves for each individual TL material without laser heating. CaF_2:Dy has its highest peak at 150 °C while LiF:Mg,Ti has a peak at 225 °C, which differs slightly from published data from Table 4.2. Even in Figure 4.8(a), the relative maximum intensity of TLD-200 is quite close to 16 times higher than that of TLD-100. It is noted that the CaF_2:Dy or TLD-200 data does not seem to have a strong blackbody radiation component, probably due to its strong TL

Table 4.2: TLD material properties.

TLD Name	Phosphor	Glow peak (°C)	Emission (nm)	Relative sensitivity	Linear Range (cGy)
TLD-100	LiF:Mg,Ti	210	425	1	0.005 - 100
TLD-200	CaF2:Dy	200, 240	480, 575	16	0.001 - 1000
TLD-400	CaF2:Mn	300	500	10	0.001 - 1000
TLD-800	Li2B4O7:Mn	210	600	0.4	0.01 - 300
TLD-900	CaSO4:Dy	220	480, 570	30	$1e^{-4}$ - 3000
TLD-100H	LiF:Mg,Cu,P	232	310, 410	0.5	N/A

All the material properties are from [1].

intensity. It is also found that there is no interaction effect between LiF:Mg,Ti and CaF_2:Dy.

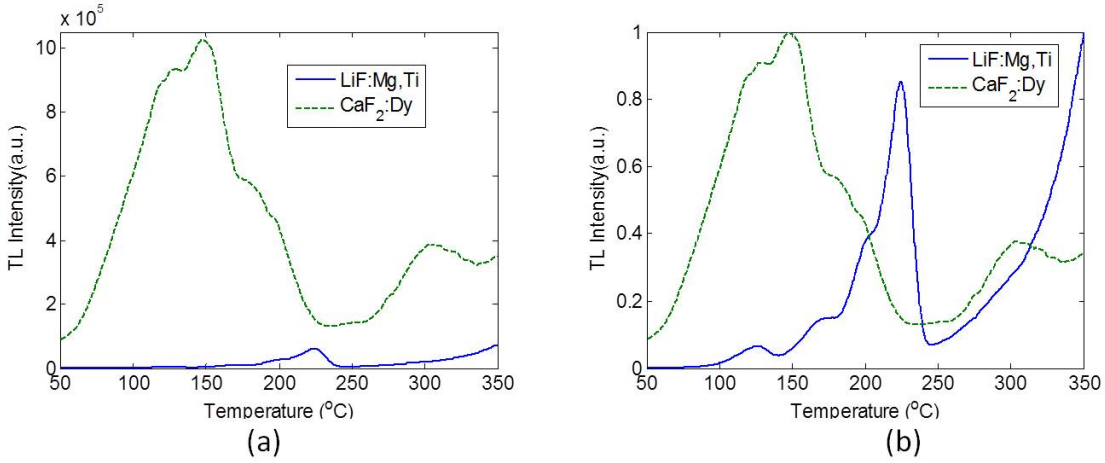

Figure 4.8: Thermoluminescence of LiF:Mg,Ti and CaF_2:Dy in (a) relative intensity, and (b) normalized intensity

The blackbody signal is emitted from the sample holder and was subtracted to obtain more accurate TL parameters. Figure 4.9 shows a typical TL intensity curve of LiF:Mg,Ti. Since our experiments in this study did not use a short-pass filter to reduce blackbody radiation, we have included the blackbody radition in the figure as well as a reconstruction TL curve created by mathematically subtracting the blackbody response.

Figure 4.10(a) indicates how the reconstruction of LiF:Mg,Ti works. The trap parameters used in this thesis were from the reference papers [30, 53] but modified to

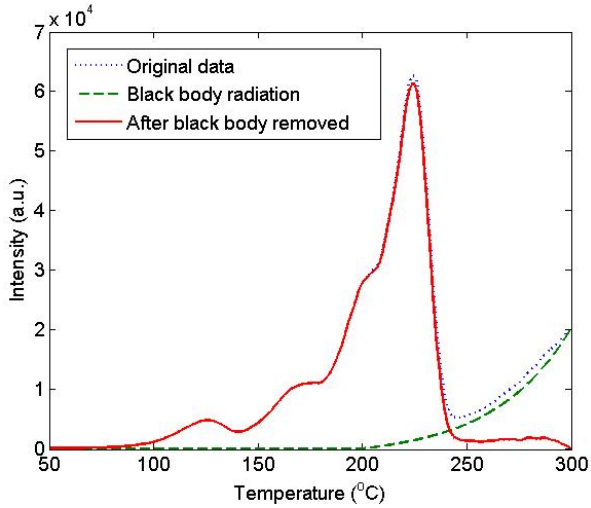

Figure 4.9: LiF:Mg,Ti TL glow curve with and without black body radiation

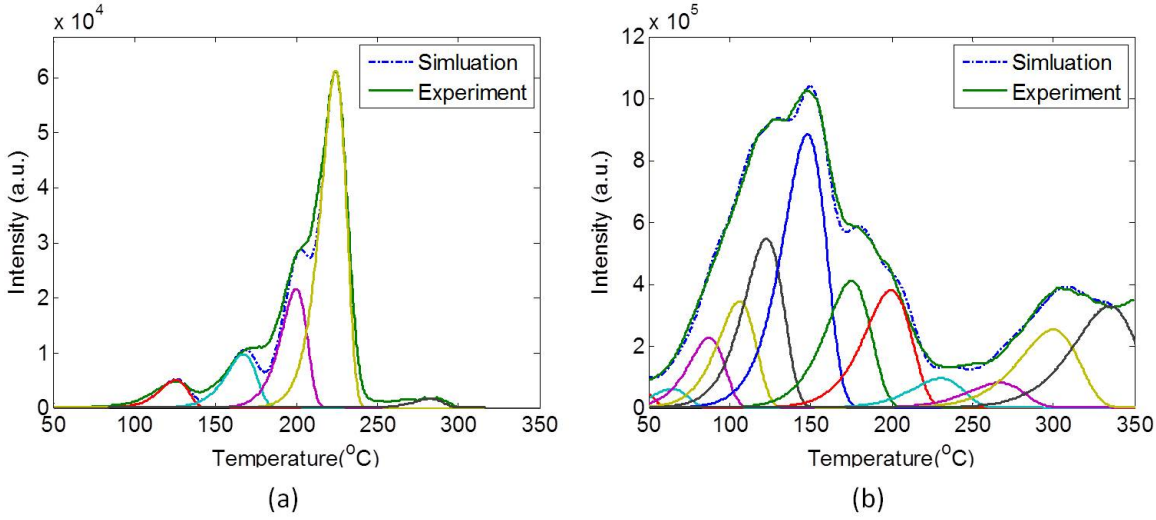

Figure 4.10: Deconvolution of TL materials to obtain trap parameters (a) for LiF:Mg,Ti, and (b) for CaF_2:Dy

acquire better matching results. It is noted that the simulated intensities over temperature seem to have a sharper transitions between each peak than the experimental results, which have a blunt transition. In the same manner, one can reconstruct the CaF_2:Dy intensity as shown in Figure 4.10(b) where the CaF_2:Dy parameters used to start the simulation were from [55]. The trap parameters actually used could be slightly different from the literature due to different heating rates, materials variations, experimental conditions, and so forth. It is noted that the CaF_2:Dy data does not seem to have a strong blackbody radiation component, probably due to its strong TL intensity.

Table 4.3: Trap parameters after a de-convolution of each TL intensity curve

Material	Parameter	Values
LiF:Mg,Ti	n_0	1.45×10^5, 3×10^5, 5.7×10^5, 1.59×10^6, 5×10^4
(5 traps)	E	1.562, 1.78, 2.411, 2.71, 2.95
	s	5×10^{18}, 2×10^{19}, 5×10^{24}, 3×10^{26}, 5×10^{25}
CaF_2:Dy	n_0	2×10^6, 2×10^6, 0.75×10^7, 1.2×10^7, 2.0×10^7, 3.51×10^7,
(12 traps)		1.7×10^7, 1.65×10^7, 0.45×10^7, 0.42×10^7, 1.38×10^7, 1.9×10^7
	E	0.80, 0.86, 0.99, 1.04, 1.080, 1.125,
		1.223 1.302 1.355 1.42 1.515 1.61
	s	5.5×10^{11}, 5.5×10^{11}, 5.5×10^{12}, 5×10^{12}, 4×10^{12}, 1.9×10^{12},
		3.5×10^{12}, 4.5×10^{12}, 2×10^{12}, 0.9×10^{12}, 1×10^{12}, 1×10^{12}

All the trap parameters are derived with deconvolution method in this paper.

Table 4.3 shows a summary of these reconstructed TL trap parameters. It is found that LiF:Mg,Ti has 5 traps while CaF_2:Dy has more than 12 traps. Once we have extracted a set of trap parameters, we also measure the luminescent intensity versus wavelength for the LiF:Mg,Ti and CaF_2:Dy. A wavelength is selected where the intensities of the two materials are approximately the same and then the residual intensity ratio factor is included in our simulations. The results will be discussed in a subsequent section.

Table 4.4: Comparison of the trap parameters of LiF:Mg,Ti

Parameters	category	peak 1	peak 2	peak 3	peak 4	peak 5
E	this study	1.562	1.78	2.411	2.71	2.95
E	Ref. [30]	1.315	1.515	1.532	1.697	2.250
s	this study	5×10^{18}	2×10^{19}	5×10^{24}	3×10^{26}	5×10^{25}
s	Ref. [30]	1×10^{12}	8×10^{12}	2×10^{18}	9×10^{18}	1.8×10^{24}

Table 4.4 shows comparison of the trap parameters of LiF:Mg,Ti reported in this

study and reference [30]. It is noted that these parameters can vary depending on how to pick up the parameters for simulation.

Chapter 5

SiO_2 Nanorod Thin Film Encapsulated by ALD Al_2O_3

This chapter is mainly extracted from the reference [61].

5.1 Introduction

Thin films consisting of SiO_2 nanorods are of great interest because they tend to have a refractive index lower than the bulk value of about 1.46, which is especially useful in distributed Bragg reflectors [6] and anti-reflection coatings [7]. In principle, there is an inverse relationship between film porosity and refractive index because the air trapped between nanorods reduces the composite refractive index of the film. Oblique-angle deposition makes it possible to grow these nanorods due to the self-shadowing effect [6]. As shown in Figure 5.1, there is a region where deposition is blocked due to self-shadowing. This effect creates nanorod thin films. A DBR made of the same material can be also realized by this oblique angle deposition [8].

Increasing the porosity, however, also causes the film to interact unfavorably with the external environment so that material properties such as refractive index and coefficient of thermal expansion (CTE) are unstable. For instance, water, with a refractive index of 1.33, can be trapped in the pores and boost the overall refractive index of a thin film, with the effect depending heavily on the level of surrounding humidity [9]. In addition to SiO_2, there are many other films whose mechanical properties are dependent on

environmental conditions as well, for example, zirconium tungstate thin films [10] show different CTEs in dry versus wet environments.

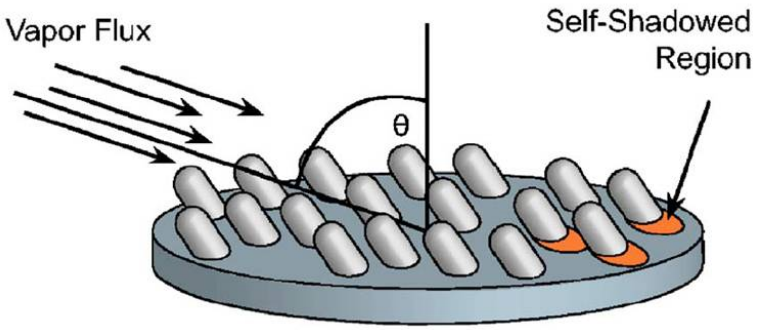

Figure 5.1: Explanation for self-shadowing effect in [6]

In this chapter we demonstrate that it is possible to stabilize porous films and prevent them from interacting with the ambient by coating ALD Al_2O_3 on top of the unstable dielectric films. This technique will be extremely important, not just for mirrors which need to be precisely controlled over temperature, but also for making thermally invariant mirrors [11].

5.2 np-SiO_2 properties

Thin films of np-SiO_2 were deposited on 250μm thick (100) Si wafers by electron beam evaporation, with the substrates at room temperature and mounted at an oblique angle of 60° relative to the source material. The oblique angle is typically defined as an angle between vapor flux and substrate normal [6], and that is the convention used here. The refractive index versus temperature of the resulting films was measured at 632.8nm by a Gaertner ellipsometer in a clean-room environment with 40% relative humidity (RH). Heating and cooling was performed with a thermoelectric heating element and temperature controller. Wafer curvature versus temperature measurements were performed with a Frontier Semiconductor FSM-900TC commercial stress measurement system. These measurements were made both in clean-room air at 40% RH, and in a dry N_2 ambient with a continuous flow rate of roughly 2000 sccm (standard cubic centimeters per minute).

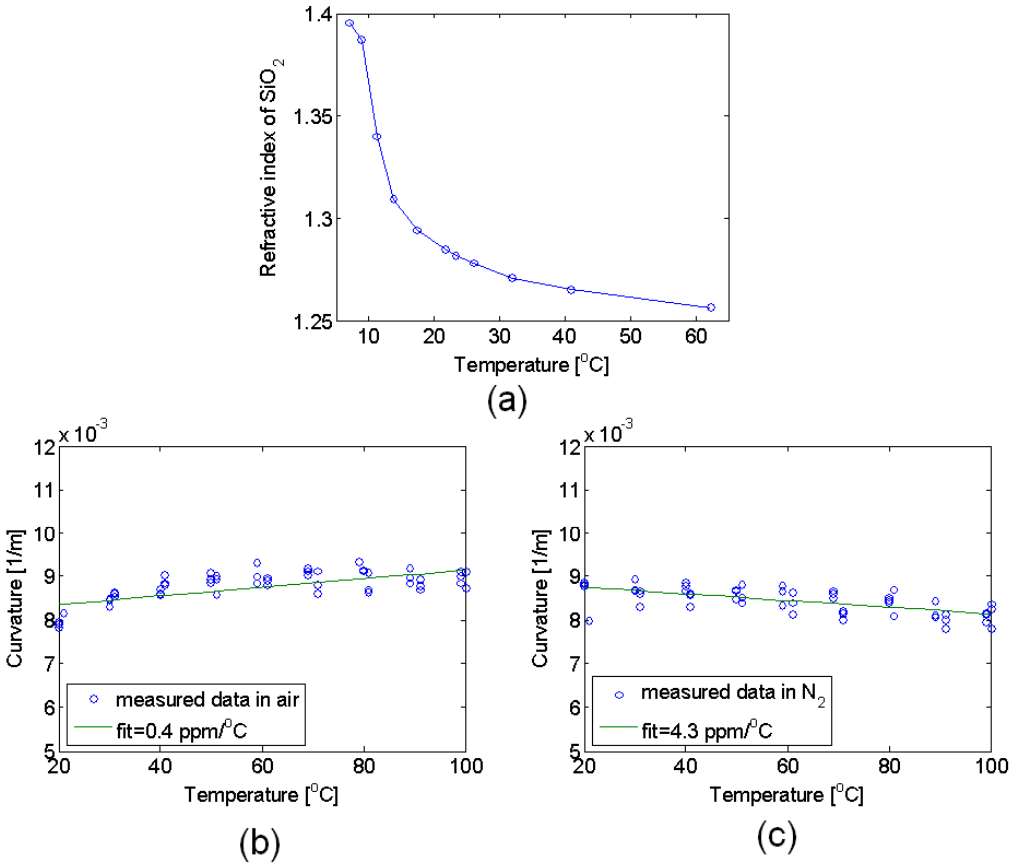

Figure 5.2: The properties of np-SiO_2 change significantly with ambient conditions. Measurements of (a) refractive index versus temperature in the presence of humidity and wafer curvature change versus temperature (b) in air and (c) in dry N_2.

Figure 5.2 shows how measured film properties vary with changes in ambient conditions. Figure 5.2(a) indicates that the refractive index drastically decreases as the temperature increases. The thermo-optic coefficient (dn/dT) of the np-SiO_2 film is almost -3×10^{-3}/°C in the range of 10°C-70°C, over two orders of magnitude larger than the roughly 10^{-5}/°C expected from changes in intrinsic material properties [62]. This occurrence is explained most simply by the presence of pores that can easily desorb and adsorb water vapor from an external environment as temperature increases and decreases, respectively. Figure 5.2(b) and (c) show the measured curvature change with respect to temperature in air and N_2, respectively. The sign of the slope depends on

the CTE value of the substrate; a slope of zero would indicate the film CTE exactly matches that of the substrate. When the CTE of a thin film is lower than the substrate, it curves upward upon heating. Similarly, the substrate curves downward upon heating when film CTE is larger than substrate CTE. Therefore, the positive and negative slopes in Fig. 5.2(b) and (c) occur, even though both np-SiO_2 CTE values are positive. The typical curvature measurement in N_2 can be seen as Fig. 5.3. It is noted that the first heating cycle is different from the rest of the curves because water vapor trapped in porous sites outgases, resulting in a different curvature behavior than subsequent heat cycles. When the CTE is calculated from measurements in N_2, the first cycle data were removed because there was hysteresis loop with the first run that behaves differently than any other runs.

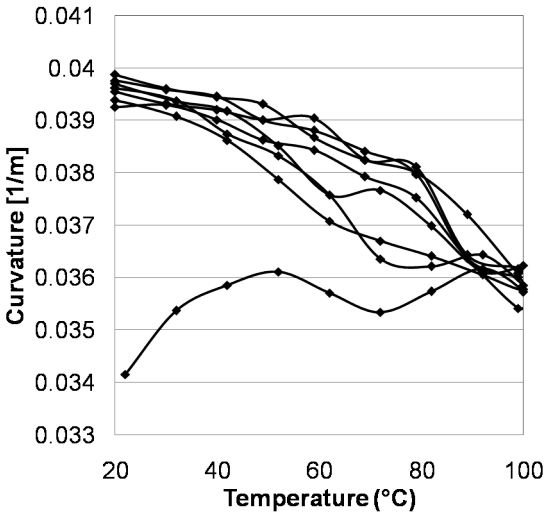

Figure 5.3: Typical curvature measurement in N_2. It is noted that the first heating cycle is different from the rest of the curves because water vapor trapped in porous sites outgases, resulting in a different curvature behavior than subsequent heat cycles.

Quantitatively, the np-SiO_2 film CTE in each case is extracted from the slope of each dataset using a linear, multilayer analysis based on free-plate theory [11], with assumptions of substrate and film biaxial modulus as shown in Fig. 2.1.

For this particular film, the CTE change between air and N_2 is roughly one order of magnitude (0.4ppm/°C to 4.3ppm/°C), which would make it difficult to model and use in a multilayer optical design, where thermomechanical performance is also of interest.

As with refractive index, the observed CTE instability is most likely caused by adsorption and desorption of water vapor contained in the air ambient by the nanoporous film, changing its properties. In contrast, as the temperature is cycled in an N_2 environment any moisture in the film tends to outgas until the film reaches a steady-state with thermal expansion behavior dominated by intrinsic film properties [63].

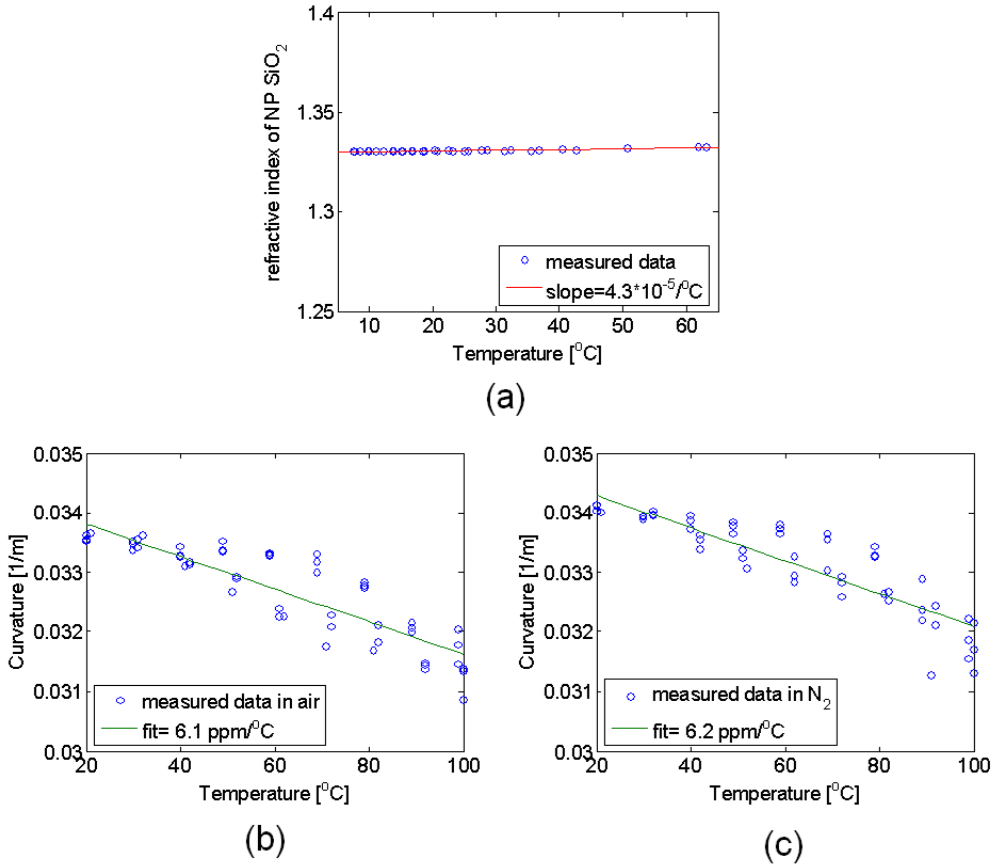

Figure 5.4: (a) The refractive index of np-SiO_2 encapsulated ALD Al_2O_3 , plotted on the same scale as Fig. 5.2, shows very little change with temperature. Similarly, the CTE values extracted from measurements of curvature versus temperature indicate a np-SiO2 CTE of (b) 6.1 ppm/°Cin air, and (c) 6.2 ppm/°Cin N_2, assuming a constant Al2O3 CTE of 3.4ppm/C.

5.3 Encapsulation of np-SiO_2

Many dielectric materials made by electron beam evaporation, even without oblique-angle deposition, show similar ambient dependence [63]. After numerous attempts to keep the CTE and optical constant stable with different materials and deposition methods, we found that ALD Al_2O_3 works quite well. ALD Al_2O_3 films were deposited with a Cambridge NanoTech, Inc. Savannah system, using alternating pulses of H_2O and trimethylaluminum at a process temperature of 250°C and pressure 1 torr, with N_2 as the carrier gas flowing at 20 sccm. Figure 5.4(a) shows the np-SiO_2 optical constant change with temperature when encapsulated by ALD Al_2O_3. The refractive index for the buried np-SiO_2 layer was calculated indirectly based on the measurement of the total reflection obtained from ellipsometry, assuming constant film thicknesses and ALD Al_2O_3 index. Basically, an ellipsometer measures amplitude (ψ) and phase shift Δ of polarized light reflected on the thin films as shown in the equation (5.1). The magnitude and phase of the reflected light incident upon the multi-layered thin films can be calculated with optical transmission matrix method, which was explained in Chapter 2. The reflectivity ratio is:

$$\rho = \frac{r_p}{r_s} = \tan(\psi)e^{i\Delta} \tag{5.1}$$

where r_p is p-polarized reflectance (TM mode), r_s is s-polarized reflectance (TE mode), $\tan(\psi)$ is the ratio on the reflected amplitude, and Δ is phase shift.

The dn/dT of np-SiO_2 was found to be 4.3×10^{-5}/°C, which is similar to the intrinsic behavior of fused silica (about 10^{-5}/°C [62]). Since the dn/dT of bulk Al_2O_3 is also 10^{-5}/°C[64], the exact quantitative result for dn/dT of encapsulated np-SiO_2 may be somewhat lower than what we measured, but the overall point remains. The refractive index of np-SiO_2 is stabilized by ALD Al_2O_3.

As shown in Figure 5.4(b) and (c), ALD Al_2O_3 can also encapsulate the np-SiO_2 in terms of thermomechanical properties. The measured film thicknesses for the system in Figure 5.4 are 1302 Å of Al_2O_3 and 2037 Å of np-SiO_2. We determined the refractive index of the Al_2O_3 to be 1.65 compared to 1.6-1.7 reported in [65]. The instability of the underlying film CTE between air and N_2 has dropped from 3.9 ppm/°C to 0.1ppm/°C when encapsulated, the latter being a much more manageable level of variation for design purposes. These results agree with recent observations that

ALD Al_2O_3 is believed to be a gas diffusion and moisture permeation barrier [66], [67]. While that research was based on encapsulation of polymer materials, our measurements indicate ALD Al_2O_3 is a promising moisture permeation barrier for low-index np-SiO_2.

5.4 Application to Distributed Bragg Reflectors

Table 5.1: Parameters measured for the various layers in the 4-pair DBR mirror

Layer No.	Materials	Thickness Å	Refractive index @ 632.8nm
8	ALD Al_2O_3	1086	1.66
7	SiO_2	1098	1.33
6	TiO_2	1569	1.96
5	SiO_2	1620	1.31
4	TiO_2	1627	1.95
3	SiO_2	1436	1.32
2	TiO_2	1108	2.07
1	SiO_2	1926	1.31

We developed and fabricated a DBR based on np-SiO_2, TiO_2 made by electron beam evaporation, and ALD Al_2O_3, as shown in Table 5.1. All measurements were performed on dummy wafers with a single film co-deposited with the DBR mirror layers. For comparison, literature values for the refractive index of the films are listed below. ALD Al_2O_3 is 1.6-1.7 from [65], TiO_2 made by e-beam evaporation is 1.8-2.1 from [68], and SiO2 made by e-beam evaporation is 1.43-1.49 from [69]. In order to make a DBR mirror with more than 90% reflectance, simulations suggest we must put 8 layers of alternating np-$SiO_2$and TiO_2, with the top TiO_2 layer replaced by ALD Al_2O_3 as a barrier.

A simulation of this coating on a silicon substrate is shown in Fig. 5.5, along with actual measured reflectance; both have a 15° angle of incidence relative to normal. Data were measured on a J.A. Woollam Co. VASE spectroscopic ellipsometer system. The discrepancy between the model and the data possibly comes from deviations in actual thickness and refractive index of the DBR layers. It could be partially due to ALD Al_2O_3 penetration into the top np-SiO_2 layer, since the resulting increase in np-SiO_2 refractive index would be expected to induce a similar red-shift in peak reflectance.

Some of these variations are illustrated in Figs. 5.6 (a) and (b). Figure 5.6(a)

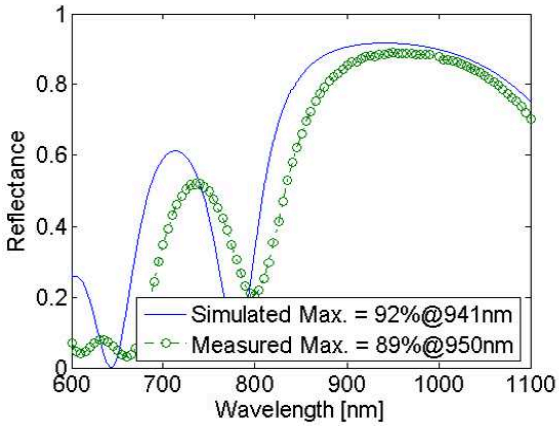

Figure 5.5: Simulated and measured reflectance versus wavelength for the encapsulated 4-pair DBR on Si. Both include a 15° angle of incidence relative to normal, since measurement at 0° is not practical. Reasonable agreement with simulation is observed, with expected variations due to some uncertainty in the thickness and refractive index of each layer.

shows the slight reduction of the discrepancy by increasing the film thickness. Because thickness measurement was always implemented with a dummy wafer having only one thin film to make the measurement easier, the real thicknesses in the DBR layers might be slightly different. Furthermore, Fig. 5.6(b) demonstrates that simulation can almost match the real measurement by increasing the refractive index of the top SiO_2 layer, considering the ALD Al_2O_3 penetration which ends up boosting the SiO_2 index. It is noted that if standard silica was used instead of the reduced-index np-SiO_2, simulations indicate that more than 12 layers would be needed to achieve a similar peak reflectance.

The encapsulation capability of ALD Al_2O_3 is also confirmed with this DBR mirror, as seen in Figure 5.7(a) and (b). The measured curvature versus temperature of the DBR coated wafer does not vary based on ambient conditions. We also performed a fit to the experimental data using a multilayer model to extract the CTE of the TiO_2 layers in each case. To do this we assume that the CTE of np-SiO_2 and ALD Al_2O_3 remain constant at the values in Table 5.2, and that all TiO_2 layers have identical CTE. This fit indicates that the CTE of the TiO_2 films is 3.6ppm/°C in air and 4.0ppm/°C in N_2, a difference of only 0.4ppm/°C . Although it is based on several assumptions, this result gives a sense of the coating stability in a changing ambient.

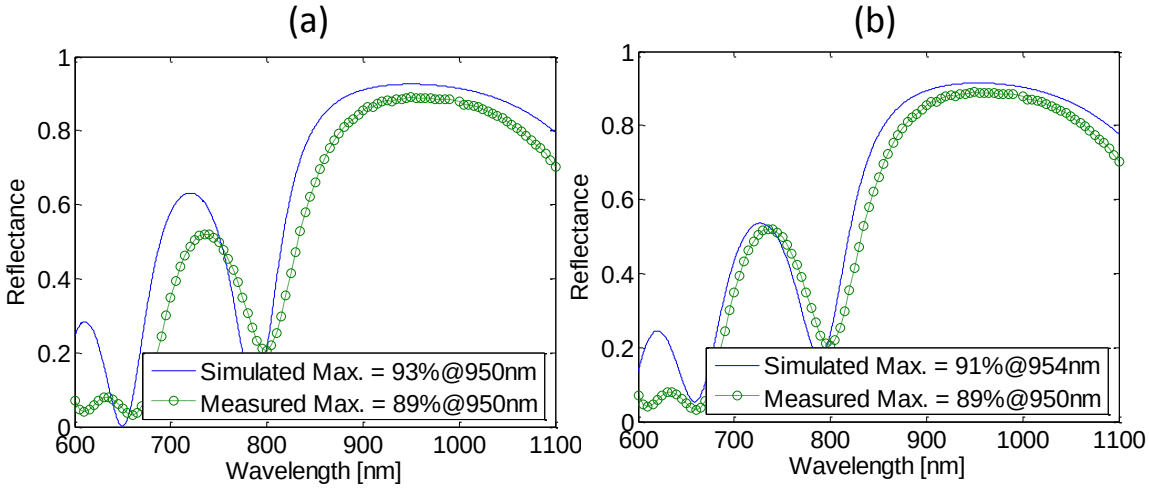

Figure 5.6: Simulated and measured reflectance versus wavelength for the encapsulated 4-pair DBR on Si. (a) with simulation that has the film thickness adjusted for better matching, and (b) by increasing the refractive index of the top SiO_2 layer in addition to increased film thickness. Simulation can almost match the real measurement in (b).

Table 5.2: Material properties of the DBR materials used in themomechanical modeling

Materials	Biaxial modulus (GPa)	CTE (ppm/°C)
ALD Al2O3	247	3.3 – 3.4
SiO2	56	6.1 6.2
TiO2	96	3.6 4.0
Si	216.7	2.6c

Nanoindentation was performed on thin films to estimate the biaxial modulus of SiO_2, TiO_2, and ALD Al_2O_2. A MTS Nanoindenter XP with Continuous Stiffness Measurement capability was used to measure the modulus of the materials. Figure 5.8 shows a typical example of a nanoindentation measurement of modulus value. It is found that the deeper the indenter tip goes in, the harder or higher the modulus, because the Si substrate itself is harder than SiO_2. The best practice is to pick up the modulus value from the indentation data corresponding to around 10% of total thin film thickness. The green dots in Fig. 5.8 indicate where the modulus values are averaged. The SiO_2 modulus value is somewhat close to the lowest value for thermal-wet grown oxide, as summarized in Table 5.2. This is a good indication of how porous the SiO_2 is.

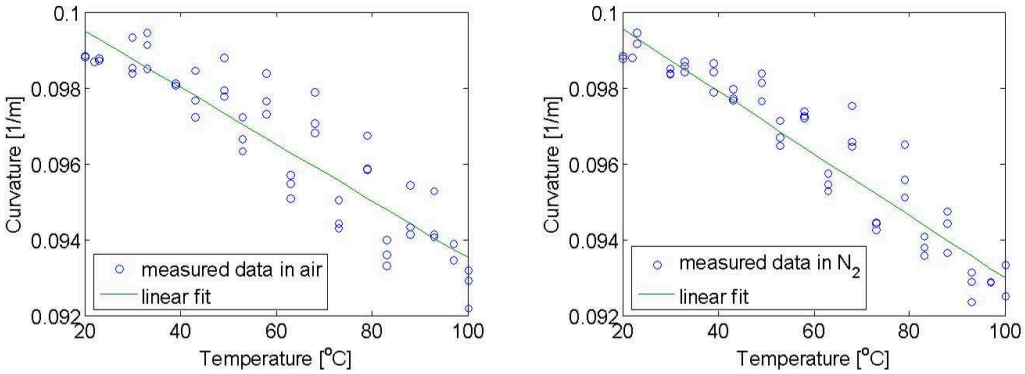

Figure 5.7: Curvature measurements versus temperature of the 4-pair DBR on Si, (a) in air and (b) dry N_2. The axes are scaled identically, and we observe no significant change due to ambient conditions.

The Si modulus value was from [70], and the Si CTE value was from [71].

For comparison, we measured the curvature change of a three-layer structure, consisting of a silicon wafer with thin films of np-SiO_2 and e-beam evaporated TiO_2. Assuming that the np-SiO_2 properties remain constant for simplicity, we found that the difference in TiO_2 CTE between air and N_2 was about 5 ppm/°C as shown in the Fig 5.9 (a) in air and (b) in N_2. This difference suggests that the TiO_2 would be a poor encapsulant and could also have a nanoporous structure.

Figure 5.10(a) shows a cross-sectional scanning electron microscope (SEM) image of the np-SiO_2 films showing the nanorod structure, which seems to be 30-60 nm in diameter. It is noted that the film thickness of this particular sample was roughly 300 nm, somewhat thicker than the others. In other films we had difficulty seeing these nanorods clearly, even though all films exhibited a low refractive index when deposited in this manner. It is believed that porosity plays an important role in lowering its optical constant, so that even films without this particular nanorod structure have a low refractive index. Figure 5.10(b) indicates how the ALD Al_2O_3 deposition process at 250°C may influence the np-SiO_2 films. The np-SiO_2 remains porous, although it is difficult to see if ALD Al_2O_3 can penetrate into the pores. One thing that we did notice, however, was that the refractive index of np-SiO_2 when encapsulated by ALD Al_2O_3 (in Figure 5.4(a)) is about 0.08 higher than the np-SiO_2 film without encapsulation near

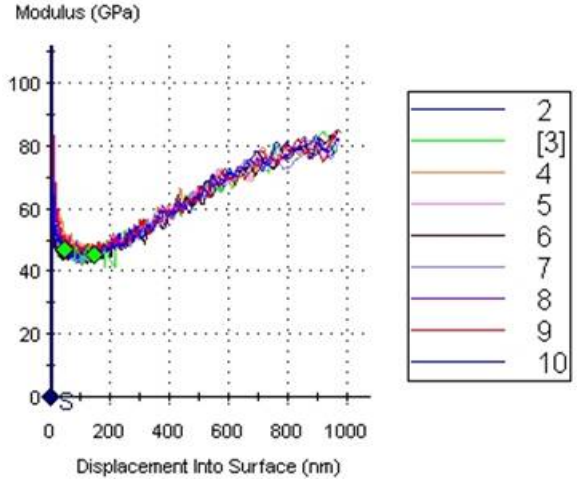

Figure 5.8: Modulus versus depth into surface of np-SiO_2 . the deeper the indenter tip goes in, the harder or higher the modulus, because the Si substrate itself is harder than SiO_2.

T = 60°C in Fig. 1(a), which suggests that ALD Al_2O_3 may partially penetrate into np-SiO_2. Furthermore, the 8-layered DBR can be seen in Fig. 5.7, showing that all of the np-SiO_2 films, except perhaps the top np-SiO_2 layer (layer 7), appear to maintain a significantly nanoporous structure. In addition, the Fig. 5.11 can show how porous thin film is.

5.5 Conclusion

We successfully demonstrate that the optical and thermomechanical properties of a SiO_2 nanorod array or np-SiO_2 can be stabilized by encapsulation with ALD Al_2O_3, while maintaining a very useful reduction in refractive index to 1.33. The dn/dT of encapsulated np-SiO_2 is only 4.3×10^{-5}/°C in a humid environment, which is much less than the -3×10^{-3}/°C observed in the exposed film. Similarly, the encapsulated np-SiO_2 CTE difference between air and dry N_2 was only 0.1 ppm/°C , compared to a shift of 3.9 ppm/°C in the bare film. The successful demonstration of this encapsulation ability is also shown in a 4-pair DBR design, showing very little curvature dependence on ambient gas, while maintaining about 90% reflectance. This technique could be useful to stabilize entire coatings, or in patterning specific regions of a film for optical

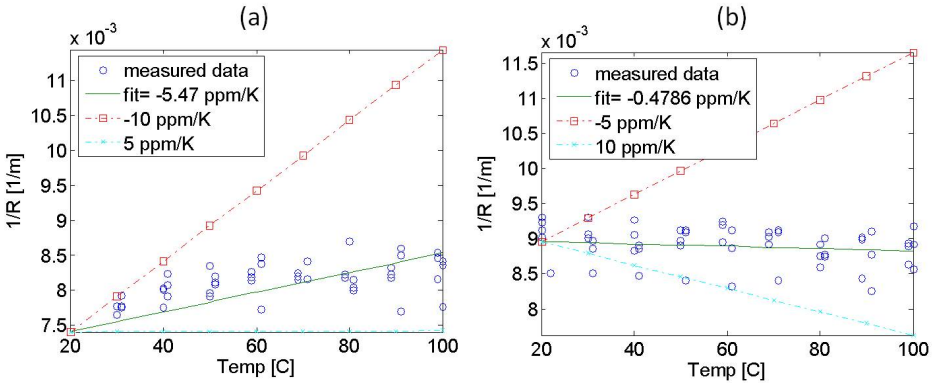

Figure 5.9: Curvature variation for three-layer structure with electron-beam deposited TiO_2 on top. This difference indicates that the TiO_2 would be a poor encapsulant and could also have a nanoporous structure.

and mechanical stability.

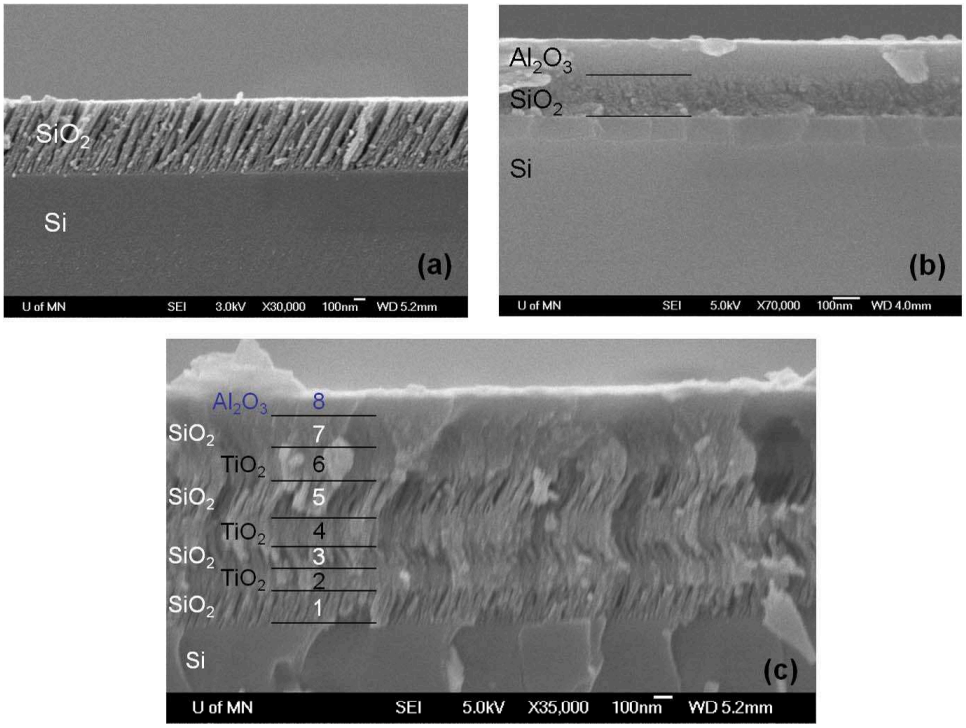

Figure 5.10: The SEM images of (a) cross-sectional SEM image of a np-SiO2 film, indicating the nanorod structure. The diameter of the nanorods varies around is approximately 30-60nm, (b) Cross-sectional SEM image of a np-SiO2 film coated with ALD Al_2O_3 , and (c) our DBR layers indicating that TiO_2 layers do not have nanorods while SiO_2 layer have nanorods.

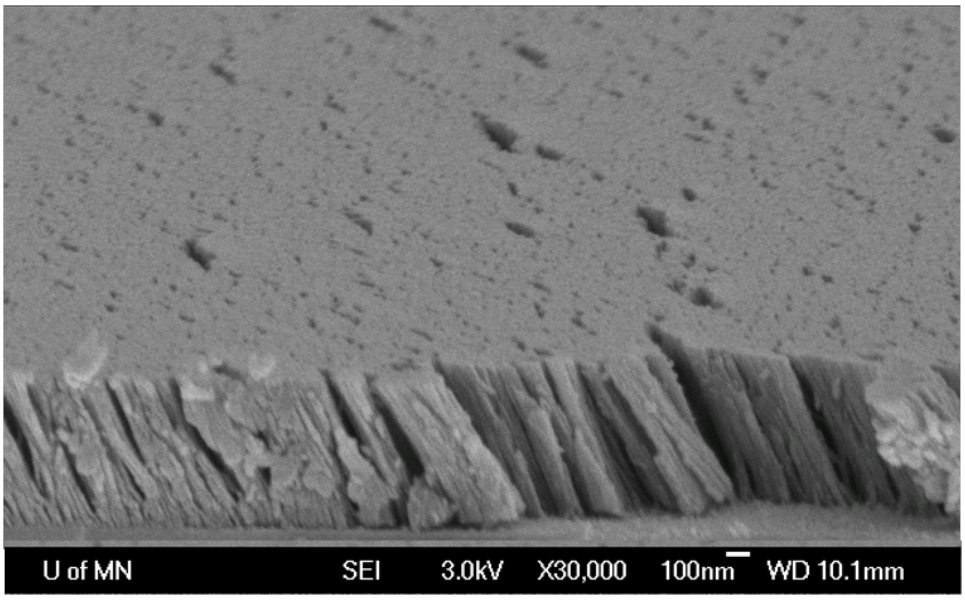

Figure 5.11: SEM image of Tilted SiO_2 nanorod thin film showing their deposition direction and how porous they are

Chapter 6

Infrared Absorption in Laser Damaged Dielectric Thin Films

This chapter is mainly extracted from references [72] and [73].

6.1 Introduction

The first sign of optical coating failure in high power laser systems is often disastrous. Because high power mirrors can be extremely expensive and often require tight alignment and mechanical assembly, it may not be possible to have backup mirrors. Ideally one would like to have an *in situ* method to assess the state of a coating that could predict damage prior to catastrophic failure. In this manner, one may be able to adapt the illumination or to repair the local area before one loses the entire mirror.

There has been much research focusing on the detection of laser-induced damage using laser scattering [12], integrated photothermal microscopy[13], total internal reflection microscopy [14, 15], high frequency scanning acoustic microscopy [16], optical coherence tomography [17, 18], and photoacoustic microscopy [19]. Not only can some methods detect the damage non-destructively, but also locate subsurface defects which are embedded deep inside of the coatings. However, most methods assume that the optical coatings have particulate defects which may not be the same material as the coating; thus it is not apparent that they could detect the fundamental mechanism of material thermal collapse.

To expand on some methods mentioned previously, laser scattering has been suggested to observe damage in optical coatings [12]. This method has the advantage of utilizing the laser light itself and therefore needs no secondary equipment. However, the method requires that the source of the coating failure is one or more particulates whose size, number, or optical constants increase with time but well before catastrophic failure occurs. While particulate failure can certainly be tracked in this way, it is not clear that the underlying mechanisms of materials failure are captured by it.

Photothermal microscopy [13] has also been used to predict the impact of laser damage in real-time. During, *et al.* [20] described a pump-probe experiment where a pump optical pulse heats a silica film embedded with gold nanoparticles. This pulse slightly heats the local area around the beam and reduces the refractive index, deflecting a probe beam. Since pump-beam heating is related to the local absorption of the film, so is the probe-beam deflection. This technique can detect nanoparticles in the coatings of interest while also providing information about the surface profile. While the technique can obtain information on the onset of laser damage, it would be unable to identify the physical mechanisms accompanying such damage.

In this thesis, we investigate if fundamental thin film characteristics could be used to track damage in optical coatings. Since it is likely that any degradation in coating strength is accompanied by a change in bond structure, a materials technique that could quantify this change might be able to predict the onset of coating damage prior to catastrophic failure. Infrared absorption measures dipole transitions directly between different molecular vibrational states. Should any characteristics of local bonding change, it will show up in the infrared absorption spectrum. Perhaps the most common type of laser damage is laser-induced thermal damage. This can occur in a highly local area due to particulate absorption, but it can also occur over a larger area due to the absorption of the coating itself. Prior research into the properties of annealed thin films has shown that the infrared hydroxyl (OH) signature often decreases under high temperature annealing due to the desorption of water [21].

It is shown that the OH infrared absorption characteristics of Al_2O_3 and Y_2O_3 membranes that have been illuminated by a high power Nd:YAG laser show significant spatial variation, corresponding to regions of high laser flux and visible damage but prior to coating breakdown. This work indicates that infrared spectroscopy should be

further examined as a technique to provide warning of thermal damage in high power optical coatings.

6.2 Fabrication of thin film membranes

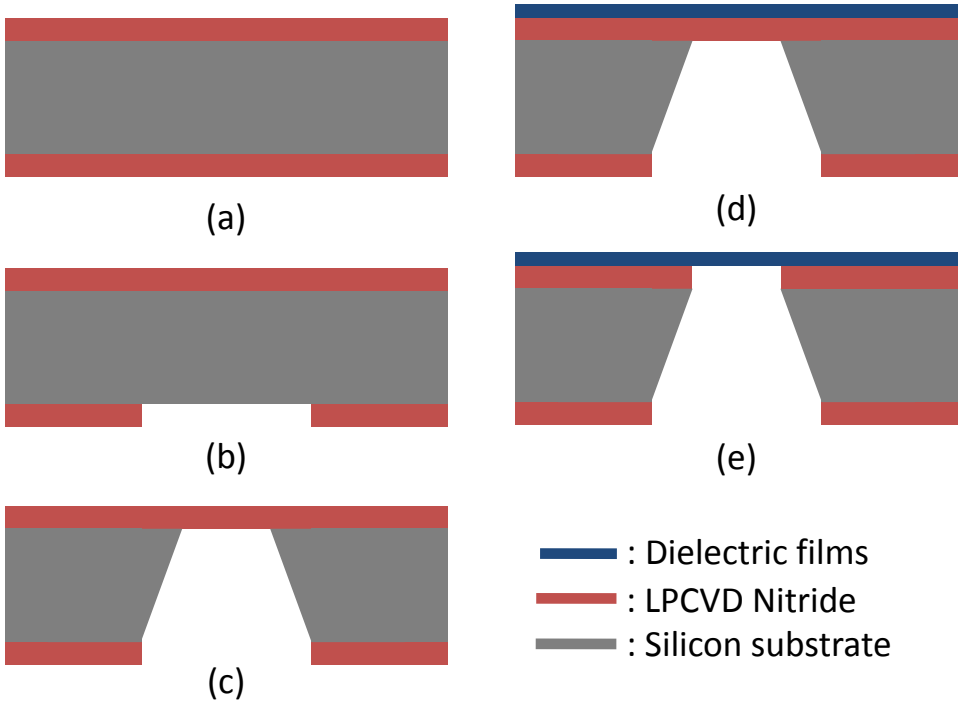

Figure 6.1: The fabrication process for thin film membranes. It is noted that membrane sizes are about 1 cm.

The influence of the substrate on the measured properties of a film is quite significant that one might wish to remove the substrat to get the more accurate properties of the film. The fabrication process as shown in Fig. 6.1 can remove or at least reduce the substrate effect, which can be a source of measurement ambiguity. Therefore, any given changes in the infrared spectrum could be unequivocally identified with the dielectric thin film itself.

In our study, the first step of the membrane fabrication process involved a low pressure chemical vapor deposition (LPCVD) low-stress silicon nitride (LSN) layer deposited with a thickness of 5000 Å on an n-type (100) 525 μm thick silicon substrate

as shown in Fig. 6.1(a). The back side of the wafer was patterned using a one-mask photolithography process, creating an opening for etching as Fig. 6.1(b). The wafer was then placed in a potassium hydroxide (KOH) solution heated to 90°C. The KOH etched through the substrate for 4 hours, leaving open holes in the silicon exposing free nitride membranes as shown in Fig. 6.1(c).

Figure 6.1(d) shows how a thin film of Al_2O_3, Y_2O_3, Nb_2O_5, or WO_3 was then deposited on the front side of the nitride membranes using electron-beam (EB) evaporation or atomic layer deposition (ALD). The thickness of these films was around 3000 Å. The final step was to remove the LSN film underneath the oxides using reactive-ion etching (RIE). It is noted that the RIE etching time was controlled so that some residual LSN might remain, in order to minimize etching of the optical coating while significantly reducing the effect of LSN on subsequent measurement. The resulting membrane structure is shown in Fig. 6.1(e).

6.3 Experimental Setup

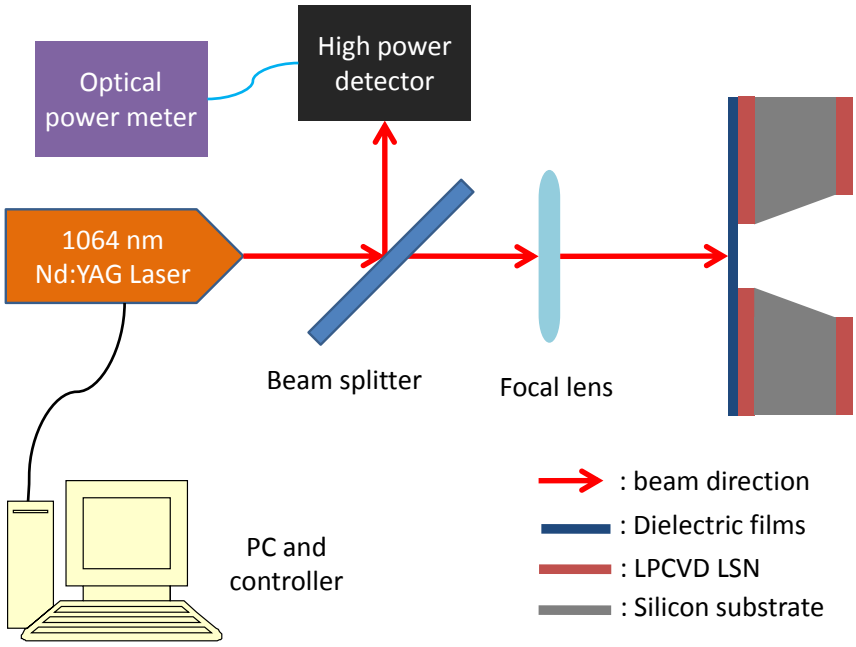

Figure 6.2: The experimental setup for laser damage testing

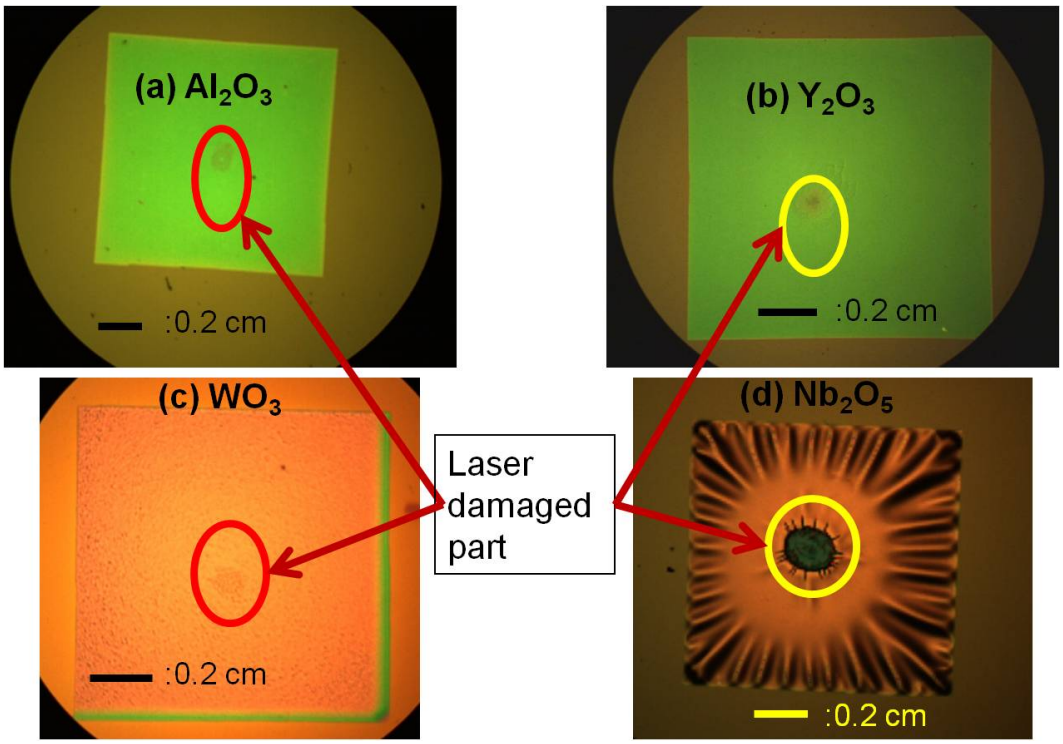

Figure 6.3: Optical microscope images of laser damaged membranes

Figure 6.2 indicates the experimental set-up for laser damage testing. A 1064 nm Nd:YAG laser (U.S. Laser Corporation Model 405) in continuous wave mode was employed for laser damage testing of the completed membrane structures as shown in the left side of the Fig. 6.2. A Newport 818T high power detector and Model 2835-C optical meter were used to measure the laser power after the beam splitter. To achieve a small laser spot, a focal lens was positioned between the beam the thin film membrane and splitter. The resulting spot size was approximately 0.5 mm in diameter. The optical power at the membrane was approximately 5 W and was applied for 5 seconds, corresponding to an approximate 640 W/cm^2. Note that the lower power with considerably longer time yields a slightly higher fluence than a femtosecond or nanosecond laser, which usually measures at tens of J/cm^2. After this exposure, non-catastrophic damage was visible to the eye. Optical microscope images after laser exposure are shown in Fig. 6.3; the membrane size is roughly 1 cm^2 while the damaged spot is around 0.5 mm diameter. All films except Nb_2O_5 seem to look reasonable; the Nb_2O_5 membrane was

severely damaged by the laser so that any meaningful scientific result from this sample may not be possible.

6.4 EXPERIMENTAL RESULTS

We will first discuss the Fourier transform infrared (FTIR) spectra results, which indicate there are IR signatures for laser damage. In the next section, it is discussed that surface roughness or film quality can be determined by using a confocal microscope, indicating why some of the membranes do not follow the general observation where OH bonds decrease upon laser damage. In the final section, the Raman spectra will be introduced as a complementary tool for the FTIR.

6.4.1 Fourier Transform Infrared Spectra

The Fourier transform infrared (FTIR) spectra of the membranes were obtained with a Nicolet Series II Magna-IR System 750 using the microscopic transmission mode, which has a position resolution of 150 μm. Fig. 6.4 shows the change in the spectra with and without laser damage. Most spectral features show little change except those around 3500 cm^{-1}. A broad peak observed in the O–H stretching region centered at approximately 3500 cm^{-1} has been correlated with surface hydroxyl groups [74], which most dielectric materials usually have on their surface.

The actual FTIR spectroscopy measurements were done more than 2 weeks after the samples were irradiated by the Nd:YAG laser, suggesting that re-adsorbed water onto the surfaces of the films does not affect the 3500 cm^{-1} peak. This measurement may indicate that laser damage drives water out from the bulk of the film, which is not replaced upon re-exposure to water vapor. An effect on O–H bonding similar to that shown by our laser damage testing was found by Kwon *et al.*, who found that the O–H peak decreased and finally disappeared as the annealing temperature went up [21]. An intriguing feature of our data is that even though these films were clearly damaged under visual observation (Fig. 6.3) and in the OH signature region, there was little evidence of damage in the region with wavenumber 2500 cm^{-1} and below according to the FTIR spectra. This result may suggest that the O-H peak might be a sensing point where we can monitor thermal damage.

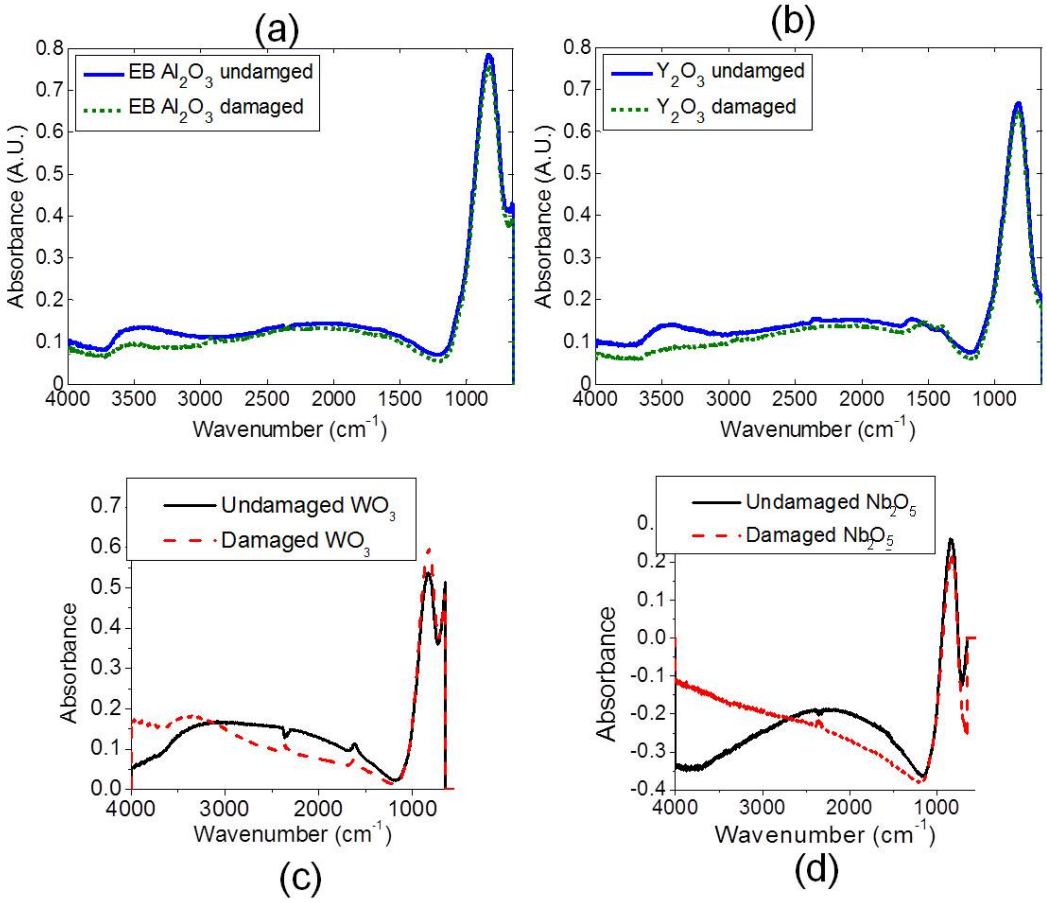

Figure 6.4: FTIR spectra of each dieletric membrane

6.4.2 Confocal microscope

The Hyphenated Systems HS200A optical profiler has been used to map out the surface profile of these membranes, especially those with FTIR spectra that are difficult to interpret. Figure 6.5 shows that the WO_3 surface seems rougher than Al_2O_3. Scattering due to the rough surface might affect our FTIR results, which could explain why it is difficult to interpret the spectral difference in Fig. 6.4(c). On the other hand, Al_2O_3 is smoother, although it has a curved shape due to residual stress between the Al_2O_3 and the LSN film left underneath it. The units of the x-axis in 6.5(c) and (f) are in mm while the y-axis is in μm. Hence, the roughness of the WO_3 is more than 2 μm which

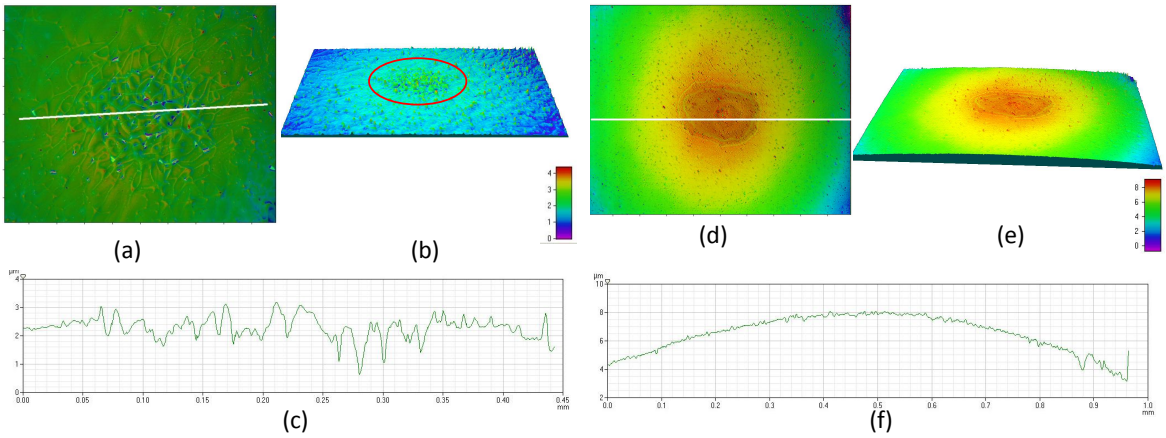

Figure 6.5: Confocal microscope images

is much larger than its thickness (around 0.3 μm), while the roughness of Al_2O_3 seems to be much less than 1 μm. This would require further investigation if more accurate numbers are needed.

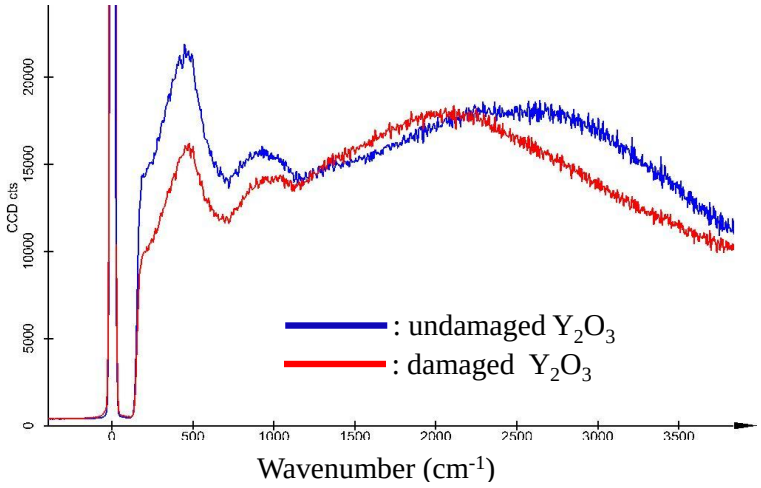

Figure 6.6: Raman microscope images

6.4.3 Raman Spectra

A WiTec Alpha300 R Confocal Raman Microscope was used to further probe the O–H vibrational signal. The Raman spectra of the films were collected with a 20 mW Omnichrome argon ion laser at 514.5 nm wavelength. Figure 6.6 shows the Y_2O_3 membrane result as a typical example of the damaged and undamaged Raman spectra. Unfortunately, due to the focused high energy excitation from the laser, fluorescence from the film and its impurities was strong enough to mask the water stretching peaks. Still, the spectrum from the damaged region on the film showed a reduction in the fluorescence intensities around 3500 cm^{-1} to 3000 cm^{-1} when compared its undamaged counterpart, possibly due to the elimination of surface hydroxyl groups. Other dielectric materials such as Nb_2O_5 and Al_2O_3 have also been tested with the same experiment. However, these membranes were catastrophically destroyed upon the Raman laser exposure so that meaningful data was impossible to obtain.

6.5 CONCLUSION

We have demonstrated that Nd:YAG laser-induced thermal damage of dielectric thin films dramatically reduces the O–H stretching mode dipole signature as measured by Fourier transform infrared spectroscopy near 3500 cm^{-1}. The remainder of the infrared spectrum appears to be largely unaffected. Microfabrication techniques were used to remove the substrate beneath the oxide membranes so that the changes in signature could clearly be ascribed to the coatings in question. This work shows that infrared spectroscopy should further be examined as a detection technique for laser induced thermal damage in high-power optical coatings [72].

Chapter 7

Heat gradient effect on thermoluminescence in heterogeneous multilayers

The majority of this chapter is derived from the article [42].

7.1 Introduction

Thermoluminescence (TL) has been used extensively in radiation dosimetry [1] and sedimentary dating [22]. In general, luminescence emission is explained as the transfer of energy from radiation to the electrons of the solid, thus exciting the electrons from a ground state to an excited state [1]. The emission of a luminescence photon takes place when an excited electron returns to its ground state [1]. Furthermore, an excited electron can become trapped at a certain level, called a trap center, where the electron will remain until it is given enough energy to return to the excited state, before undergoing a normal transition back to the grounded state [1].

Laser-stimulated TL has been a popular research topic because it has applications to micro-dosimetry and high resolution TL imaging [23, 24]. For example, Braunlich *et. al.* first devised a laser stimulated TL system using a CO_2 laser and $CaSO_4$:Mn powder. In particular, he measured the two-dimensional TL pattern of the surface with

localized laser heating [23].

Since then, there have been many attempts to study the laser-stimulated TL both theoretically and experimentally. The heat conduction model of LiF:Mg,Ti powder on top of a borosilicate glass substrate was solved analytically by Abtah *et. al.* [25, 26], focusing on laser-generated heat diffused into the LiF:Mg,Ti powder through the glass substrate, which resulted in a delayed TL response. Young *et. al.* also tried to calculate the temperature distributions of a similar LiF:Mg,Ti on a glass substrate for simple dynamic system where the laser could be turned on and off [27].

More recently, TL has found useful applications in determining the temperature history of rapid thermal events [28, 29]. Mah et. al. demonstrated that TL microparticle sensors can record the thermal history of detonated high explosives [30]. Microparticles of TL materials are uniquely suited for the detailed profiling of extremely violent temperature events, such as the explosive destruction of biological particles, which would destroy existing direct-contact sensors. TL microparticles have no fabricated components, are often composed of highly robust materials, and are inexpensive and relatively simple to fabricate in large quantities [28]. In [28], microparticles were spread onto the fabricated microheaters, which later can be used for TL measurement. However, these microparticles were difficult to integrate with the microheaters and vulnerable to external vibration, causing them to spread to locations where they can no longer produce a TL signal.

In this chapter, we suggest that thermal gradients in heterogeneous multilayered TL structures can provide a detailed record of thermal events. We model the TL responses of a three-layer TL structure for the case where laser-induced heating on one TL layer diffuses into another TL layer, resulting in different temperature distribution. To verify these simulation results, LiF:Mg,Ti and CaF_2:Dy samples are used and bonded with Kapton as an interlayer. These bonded TL composites produced strong multiple peaks from their component materials, whose individual contributions were distinguished in both the time and wavelength domains.

We discussed heat transfer modeling in chapter 3 and Thermoluminescence modeling in chapter 4, respectively. Hence, this chapter will be focused on detailed experimental results.

7.2 Experimental set-up and procedure

The LiF:Mg,Ti and CaF_2:Dy materials were purchased from Thermo Scientific [57]. The material came in the form of 3.2 mm x 3.2 mm x 0.89 mm chips and were bonded with Kapton tape from DuPont [50]. This Kapton tape can survive the high temperatures required for measurement that is performed usually up to 360°C.

Harvery *et. al.* also used high-temperature self-adhesive tape with powder based TL materials. In that paper, LiF:Mg,Ti powder was fixed in place by spreading the material over adhesive tape [75]. Using this high-temperature tape could be an inexpensive solution to make thin-layer dosimeters or temperature sensors, which might be more robust than particle-based micro heaters. However, as the adhesion of the high-temperature tape is weak, powder can still dislodge easily; therefore, fixing precise amounts of TL powder in this manner is difficult.

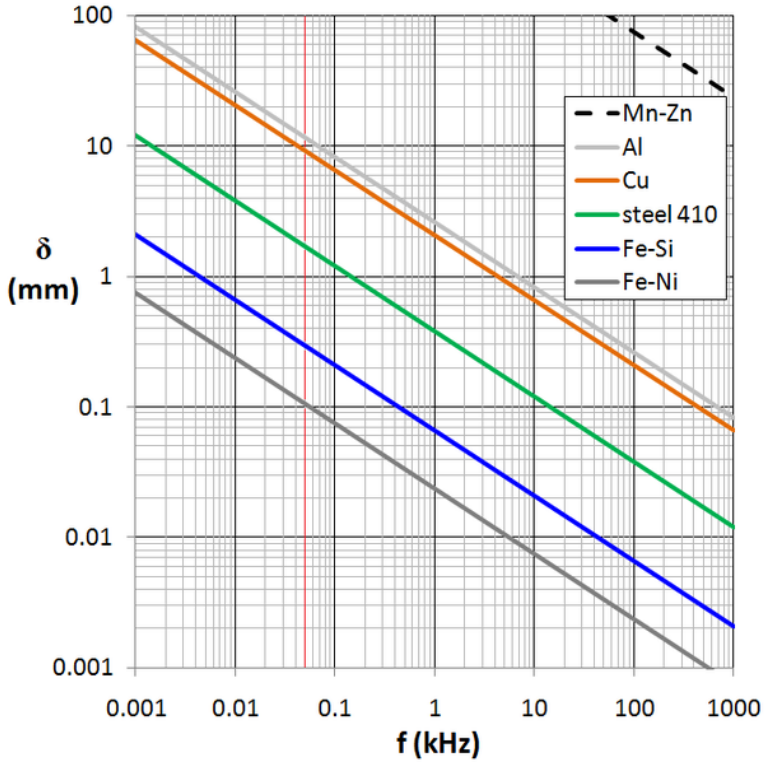

Figure 7.1: Skin depth relationship with respect to frequency in metals [76].

In addition to these three materials, 400 nm thick aluminum (Al) is deposited on top of LiF:Mg,Ti as an absorbing layer because the dielectric multilayer we built can absorb the external heating uniformly, resulting in no thermal gradients. The Al layer can take the external heating and let it diffuse into the multilayer, in which there are strong nonuniform heating that can be converted to different TL signal. Since a Nd:YAG laser was chosen as a heating source, focusing an optical beam from the laser onto the sample would be problematic, since all of materials are dielectric and would heat the whole multilayer too easily or uniformly. To determine how thick Al needs to be deposited, one can consider the skin depth of Al to be a critical parameter, which is usually around 100nm for visible light in Figure 7.1 [76].

In order to prevent light from heating the entire multilayer, 400nm-thick absorber layer composed of aluminum was deposited on the surface of the CaF_2:Dy using electron beam evaporation. Most literature is based on the frequency scale, but with the simple equation (7.1) one can have the proper skin depth with respect to the wavelength for a 1064nm Nd:YAG laser, as follows:

$$f = \frac{c}{\lambda} \tag{7.1}$$

where c is speed of light, λ is the wavelength (m), and f is frequency (Hz)

To fill the traps, the TL multilayer was irradiated with an X-RAD 320 dosage calibrated X-ray source. The source, with a beam hardening filter of 2mm thick Al, generates 2.7 Gy/min at 320kV voltage and 12.5mA current at a distance of 50cm. The LiF:Mg,Ti surface was turned toward the X-ray source to avoid potential interference of the aluminum absorber on the CaF_2 with the X-ray beam. The radiation dose was set to 700 cGy, but it was observed that the actual dose varied within $\pm$ 1Gy of this value.

A beam from a Nd:YAG laser illuminated the aluminized surface of the TL multilayer, as shown in Figure 7.2. The relative size of the composite has been exaggerated for better illustration, but the laser spot size was larger than the sample to ensure uniform lateral heating. A 50:50 beam splitter divided the light so that the optical power could be simultaneously and independently measured by a silicon detector and optical power meter. Additional optics were used to focus the light. The laser was operated in continuous wave (CW) mode, and the pulse duration was set by an external function generator.

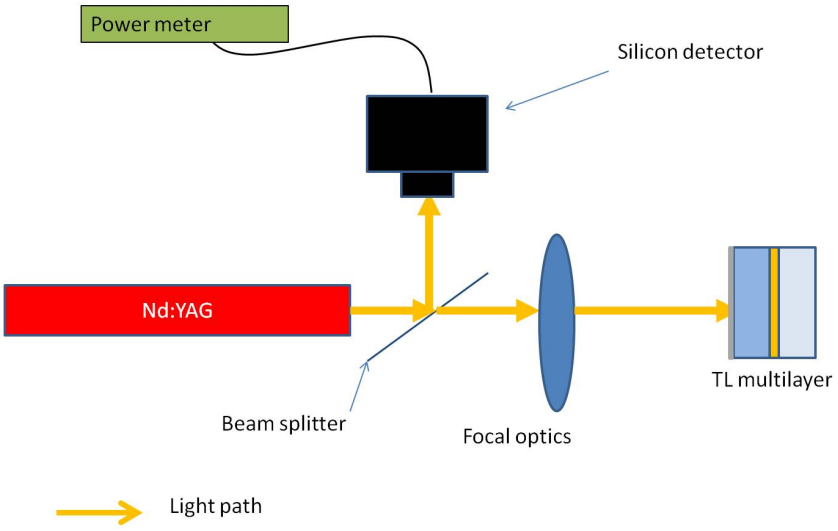

Figure 7.2: Laser heating experiment set-up. The relative size of the TL multilayers has been exaggerated for better illustration, but the laser spot size is larger than the TL multilayers to ensure uniform lateral heating across the surface.

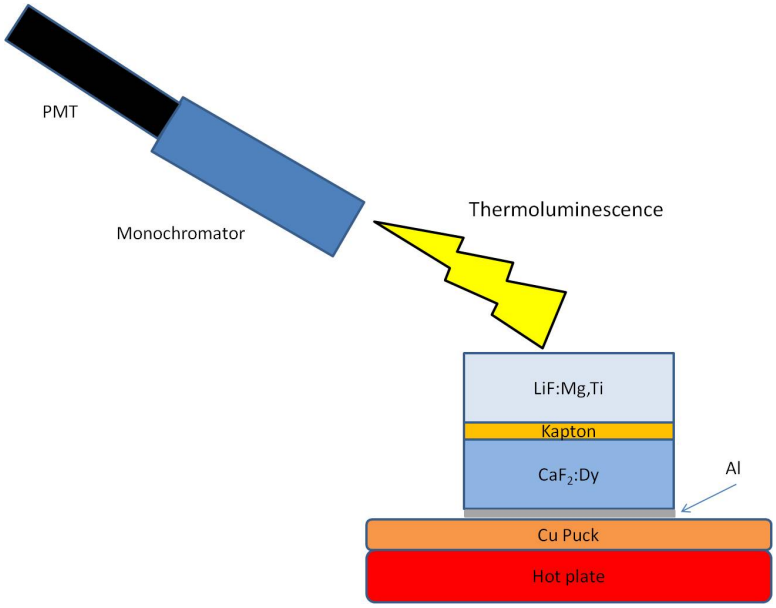

Figure 7.3: Experimental set-up for thermoluminescence test

Figure 7.3 shows the experimental thermoluminescent measurement system. The TL experiments were performed in a concealed chamber located inside a dark room 30 minutes after irradiation to ensure that effects due to thermal fading were consistent [1, 77]. In addition, the samples were carried in a black container to avoid optical fading effects [1].

A photomultiplier tube (PMT) was used to measure light output and a monochromator was used to select the specific wavelength that balanced out the TL intensities of the LiF:Mg,Ti and CaF_2:Dy materials. In this paper, a wavelength of 460nm with a 14nm Full Width Half Maximum (FWHM) passband was chosen after several trials. In order to protect the Kapton tape, the samples were placed on a copper puck atop a hot plate, thereby reducing the highest peak temperature from 400 °C to 350 °C.

7.3 Discussions

7.3.1 Interaction between TLD-200 and TLD-100

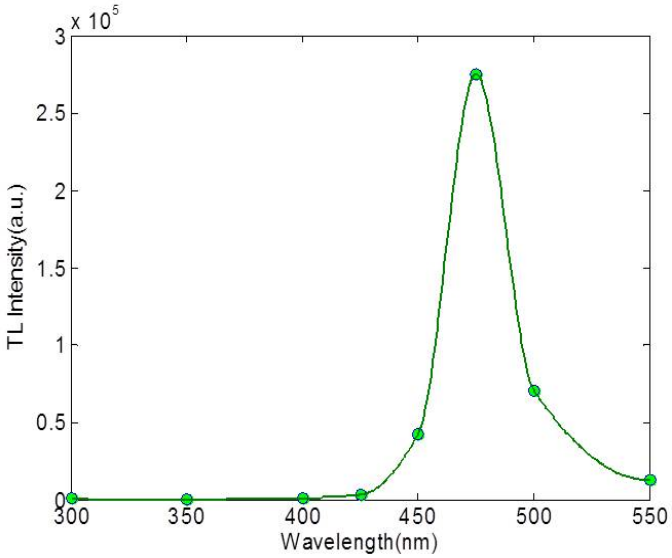

Figure 7.4: Interaction effect from luminescence of TLD-100 to TLD-200

TLD-100 has a known characteristic, called radioluminescence, in which light is emitted with a different wavelength upon irradiation. This radioluminescence has been

reported with several methods such as Cs source [78] and high eV electrons [79]. It is unlikely that low E photons would cause such an effect but to be sure, we tested the effect of the TLD-200 luminescence on TLD-100. As shown in the figure 7.3, interaction from TLD-200 to TLD-100 is of interest in this paper since the opposite interaction rarely happens due to opposite light paths.

The experiment for this interaction effect was carried out with various wavelength TL measurements, as shown in the Figure 7.4. It is noted that 480nm is the emission maximum peak of TLD-200 TL, while there is no peak at 410nm which is associated with TLD-100 emission wavelength. This observation indicates that TLD-200 TL does not interact with TLD-100. Therefore, combining two materials would not generate an interaction effect, meaning that it is easier to separate out both TL data later, which is important to note for further interpretation of the experimental results.

7.3.2 Thermal fading effect

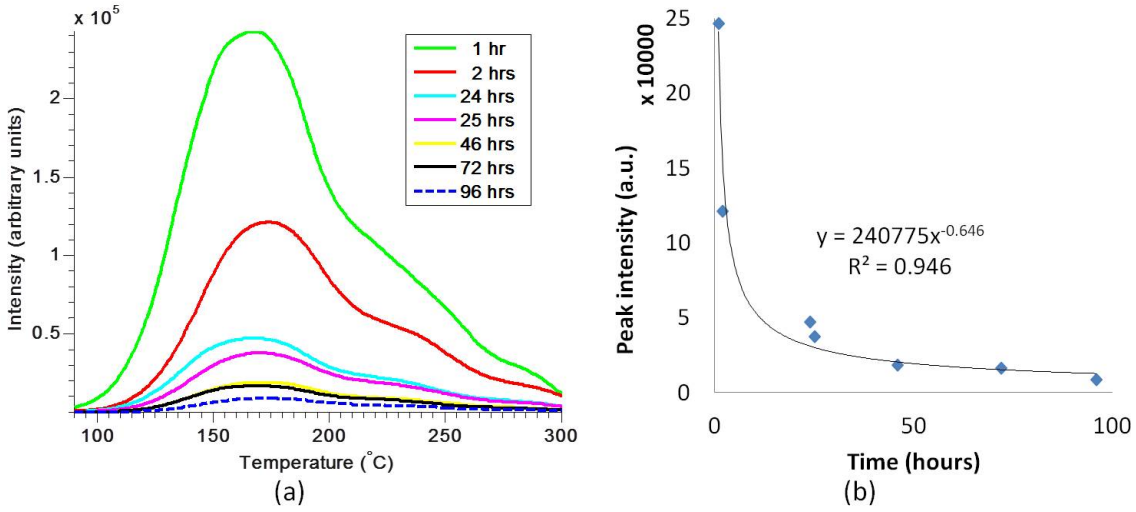

Figure 7.5: Thermal fading of TLD-200, showing that intensity drops significantly as time increases; (a) in TL glow curves, (b) in plots of intensity versus time, which shows it drops exponentially

It is observed that the traps of TLD-200 are thermally fading; in other words, TLD-200 gradually empties out its trap centers even in room temperature [1, 77]. The peak intensity drops significantly as time progresses, which might obscure the data integrity.

Therefore, our TL glow curve experiments were always carried out 30 minutes after X-ray irradiation. Figure 7.5 shows this thermal fading effect. The overall TL glow curves are shown in figure 7.5(a), and the maximum intensity over time is shown in figure 7.5(b).

7.4 Final results

The experiment was carried out cautiously with all the above effects considered. A 460nm-wavelength was selected to balance out the intensity of the two materials, and the TL measurement was also run 30 minutes after irradiation to compensate for the thermal fading effect. Furthermore, the TL multilayer samples were always stored in a black container to avoid the optical fading effect.

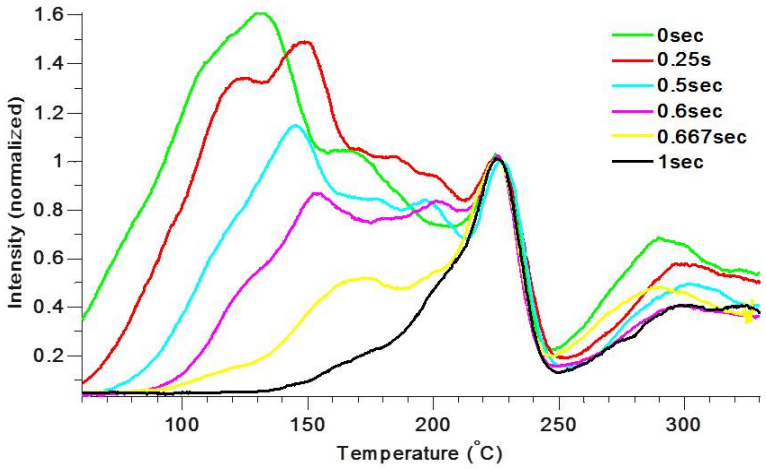

Figure 7.6: TL glow curves for bonded chips with different laser heating conditions

Figure 7.6 shows typical glow curves of the TL multilayers. The peak at 150 °C is associated with CaF_2:Dy and the peak at 225 °Cwith the LiF:Mg,Ti. The 150 °C peak began to empty upon laser heating. The lower peaks of LiF:Mg,Ti depopulated, while the peak 225 °C remained. These curves were normalized at 225 °C. The curves were also adjusted to demonstrate the same peak temperature position, because the peak temperatures drifted slightly due to variations in optical alignment, irradiation, heating rate, and thermal contact.

With heat transfer and TL de-convolution simulation illustrated in the previous

chapters, one can generate quite similar simulation graphs matching the real TL glow curves shown in Figure 7.6. Several simulation results are shown in Figure 7.7 under various conditions, including (a) with no thermal contact conductance (TCC) and original thermal diffusivities, and heating at 380°C; (b) with no TCC, original thermal diffusivities, and heating at 250°C; (c) with TCC, original thermal diffusivities, and heating at 250°C; (d) with TCC, original thermal diffusivities, and heating at 350°C; (e) with TCC, original thermal diffusivities, and heating at 480°C; (f) with TCC, modified thermal diffusivities, and heating at 480°C, respectively.

Each graph describes luminescence behavior under various heating pulses, ranging from 0 ms to 1000 ms. Figure 7.7(a) illustrates the initial TL glow curve results where simulation tends to depopulate trap parameters more quickly than the experimental results. In the second trial, we reduced the heating pulse down to 250 °C as shown in Figure 7.7(b) which was slightly better but the CaF_2:Dy peaks still remain quite intact. We introduced a TCC as shown in Figure 7.7(c) where LiF:Mg,Ti peak remain intact again. Hence, we increased the heating temperature to 480 °C as shown in Figure 7.7(e). Finally, thermal diffusivities of each layer were slightly modified to simulate the experimental results better as illustrated in Figure 7.7(f).

The simulation graphs compared with experimental results are shown in Figure 7.8 where the graphs are adjusted to have the same maximum intensity as the experimental results. If the 150 °C peak is available, the simulation and experiment have the same intensity at 150 °C as depicted in Figure 7.8(a)-(c), while the other temperature peaks vary accordingly. For the 250 ms pulse, the peak of LiF:Mg,Ti which is located at 225 °C has a 6% intensity error between the simulation and experiment. If the 150 °C peak is no longer available due to depopulation, the simulation is adjusted to have the same intensity at 225 °C like Figure 7.8(d)-(f).

In this simulation, a thermal contact conductance was introduced between the aluminum and the CaF_2:Dy layer and was found to better match experimental results than when we assumed an infinite interface conductivity. The aluminum was otherwise regarded as a perfect heat conductor that could absorb heat and dissipate it laterally. One-dimensional heat transfer was assumed, neglecting convection and other heat transfer mechanisms. The Kapton thermal conductivity appeared to differ slightly from published values, since an increase in its simulated conductivity from 0.12 to 0.144 gave

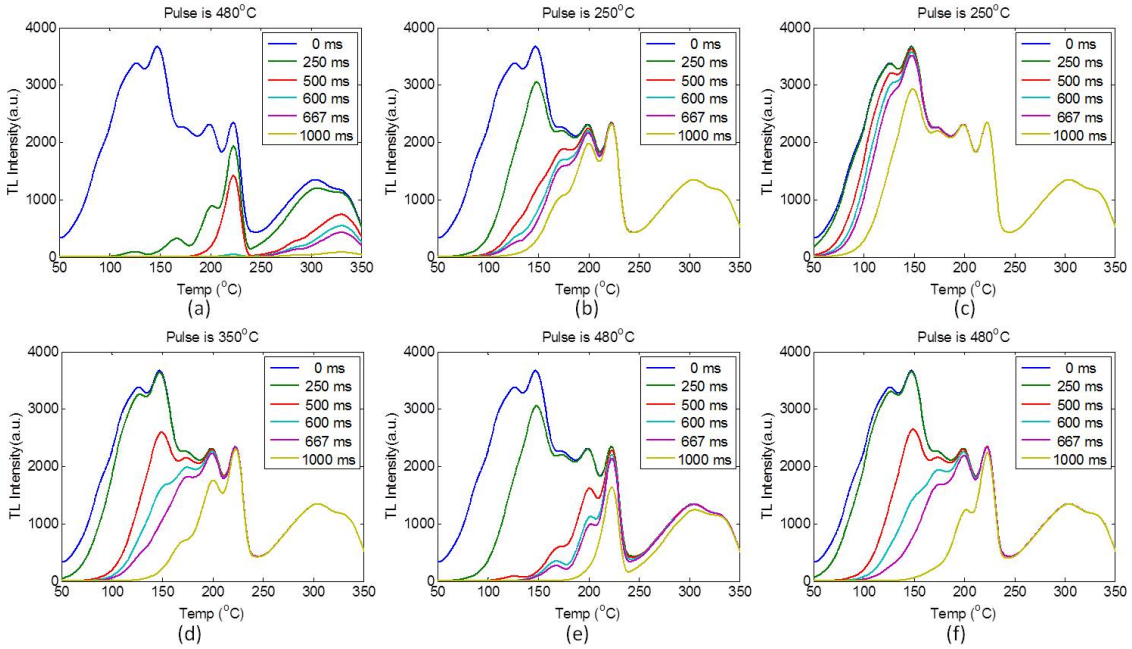

Figure 7.7: Simulated TL results with various conditions, specifically (a) with no TCC, original thermal diffusivities, and heating at 380°C; (b) with no TCC, original thermal diffusivities, and heating at 250°C; (c) with TCC, original thermal diffusivities, and heating at 250°C; (d) with TCC, original thermal diffusivities, and heating at 350°C; (e) with TCC, original thermal diffusivities, and heating at 480°C; (f) with TCC, modified thermal diffusivities, and heating at 480°C

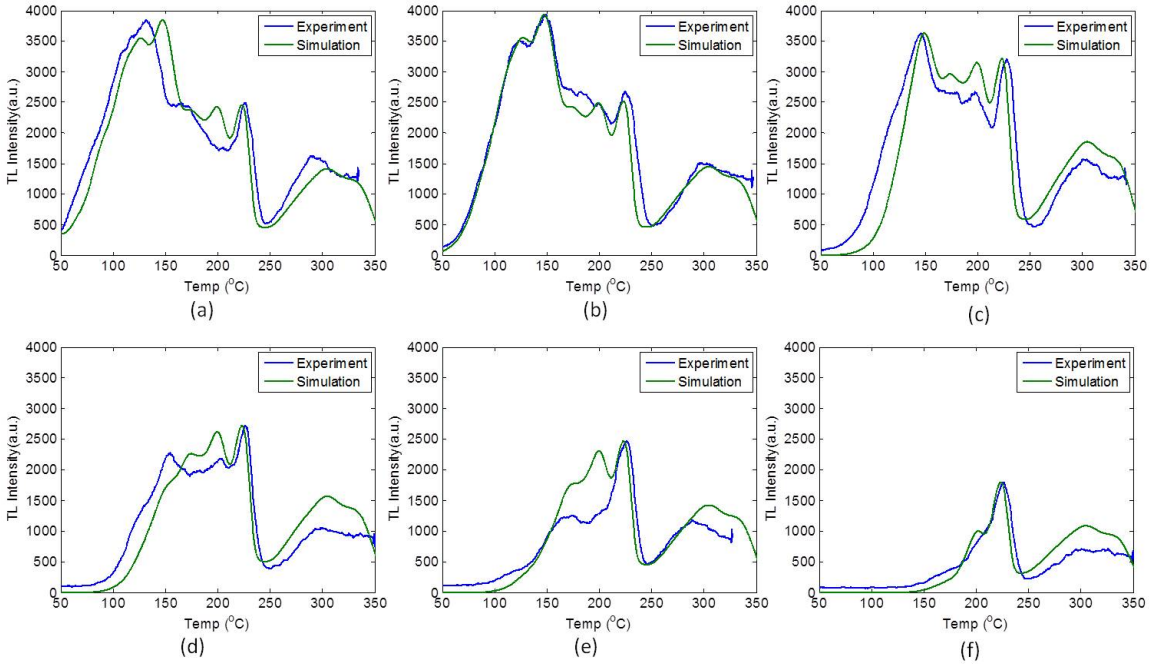

Figure 7.8: Final simulation results compared with experiment, in (a) for a laser pulse of 0 s, (b) 250 ms, (c) 500 ms, (d) 600 ms, (e) 667 ms, and (f) 1000 ms. It is noted that all the simulation curves are normalized for better comparison

better matching results between simulation and experiment.

The location of the CaF_2:Dy peaks differed from one experiment to another due to variations in the thermal contact between the samples and the Cu puck. They also varied due to the slightly different heating rates that the hot plate generated.

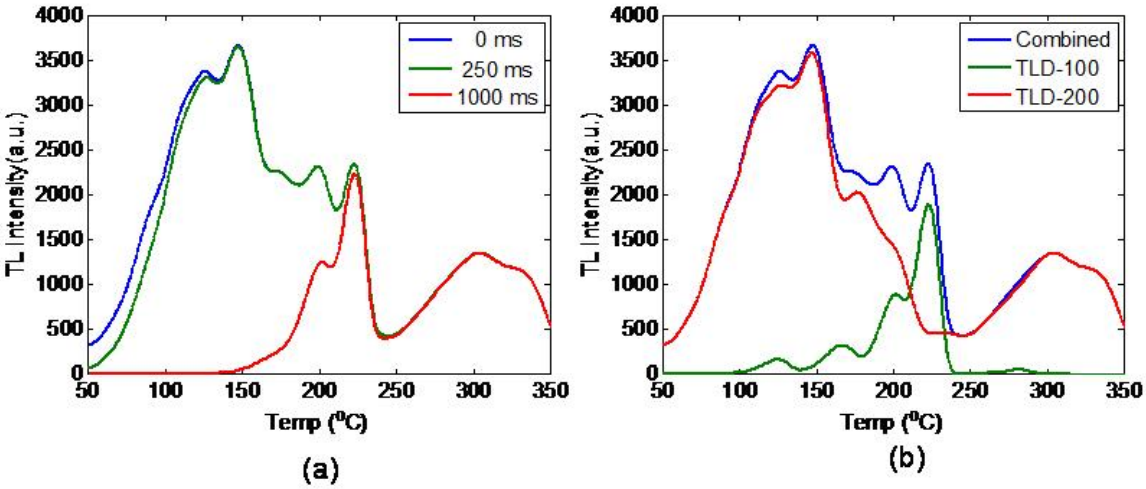

Figure 7.9: Simulated TL glow curves in (a) of the TL mulltilayer with a 0 ms laser pulse, with a 250 ms laser pulse and with a 1000 ms laser pulse, and in (b) of each TLD material with a 0 ms laser pulse.

Another promising result is that each layer can experience different laser heating, depending on the speed of the temperature pulse. Figure 7.9 shows the comparison between short versus long pulses. Figure 7.9(a) indicates TL glow curve with a 0ms laser pulse, with a 250ms laser pulse, and with a 1000 ms laser pulse. Figure 7.9(b) shows reference graphs that have TL glow curves for each TLD materials. A simple analysis indicates that short pulses depopulate only the TLD-200 while long pulses depopulate the TLD-200 and also some of TLD-100. This would be useful for temperature sensors, which need to detect temperature distribution along through their depth. This technique would be very useful in that one can track down temperature distribution across depth.

7.5 Conclusion

In summary, we modeled and experimentally tested the TL responses of heterogeneous TL multilayers for the case where laser-induced heating on one TL layer diffuses into another TL layer, resulting in different thermal gradients. LiF:Mg,Ti was bonded to CaF_2:Dy with Kapton, which is resistant to high-temperature environments. The TL multilayers were irradiated by X-rays to populate the traps of each TL material, and then the materials were heated by a Nd:YAG laser with varying laser pulse durations. The Nd:YAG laser was incident on CaF_2:Dy, emptying out the traps of CaF_2:Dy before the heat diffused into the LiF:Mg,Ti underlayer. The final results showed that, as the laser pulse time increased, the lower peaks of CaF_2:Dy depopulated first and then the LiF:Mg,Ti peaks began to depopulate. This heterogeneous TL multilayer can provide strong multiple peaks from its component materials whose individual contributions were distinguished in both the time and wavelength domains. By using these TL multilayers, a thermal history including temperature and heating duration can be reconstructed. This technique could resolve extremely rapid thermal events if the TL multilayer thickness is scaled down to the nano regime.

Chapter 8

Conclusion and discussion

In summary, this dissertation examines how to improve the reliability of high power laser systems in three significant ways.

First, we successfully demonstrate that the optical and thermomechanical properties of a SiO_2 nanorod array or np-SiO_2 can be stabilized by encapsulation with ALD Al_2O_3, while maintaining a very useful reduction in refractive index to 1.33. The dn/dT of encapsulated np-SiO_2 is only $4.3 \times 10^{-5}/°C$ in a humid environment, which is much less than the $-3 \times 10^{-3}/°C$ observed in the exposed film. Similarly, the encapsulated np-SiO_2 CTE difference between air and dry N_2 was only 0.1 ppm/°C , compared to a shift of 3.9 ppm/°C in the bare film. The successful demonstration of this encapsulation ability is also shown in a 4-pair DBR design, while showing very little curvature dependence on the ambient gas, while maintaining about 90% reflectance. This technique could be useful to stabilize entire coatings, or in patterning specific regions of a film for optical and mechanical stability.

Second, we have demonstrated that fundamental thin film characteristics could be used to track damage in optical coatings. Nd:YAG laser-induced thermal damage of dielectric thin films dramatically reduces the O–H stretching mode dipole signature as measured by Fourier transform infrared spectroscopy near 3500 cm^{-1}. The remainder of the infrared spectrum appears to be largely unaffected. Microfabrication techniques were used to remove the substrate beneath the oxide membranes so that the changes in signature could clearly be ascribed to the coatings in question. This work shows that infrared spectroscopy should further be examined as a detection technique for laser

induced thermal damage in high-power optical coatings [72].

Third, we showed that thermal gradients in heterogeneous multilayered TL structures can provide a detailed record of non-uniform thermal events. We modeled and experimentally tested the TL responses of heterogeneous TL multilayers for the case where laser-induced heating on one TL layer diffuses into another TL layer, resulting in a nonuniform temperature profile. LiF:Mg,Ti was bonded to CaF_2:Dy with Kapton, which is resistant to high-temperatures. The TL multilayers were irradiated by X-rays to populate the traps of each TL material, and then the materials were heated by a Nd:YAG laser with varying laser pulse durations. The Nd:YAG laser was incident on CaF_2:Dy, emptying out the traps of CaF_2:Dy before the heat diffused into the LiF:Mg,Ti underlayer. The final results showed that, as the laser pulse time increased, the lower peaks of CaF_2:Dy depopulated first and then the LiF:Mg,Ti peaks began to depopulate. This heterogeneous TL multilayer can provide strong multiple peaks from its component materials whose individual contributions were distinguished in both the time and wavelength domains. By using these TL multilayers, a thermal history including temperature and heating duration can be reconstructed. This technique could resolve extremely rapid thermal events if the TL multilayer thickness is scaled down to the nano regime.

References

[1] S. W. S. McKeever. *Thermoluminescence of Solids*. Cambridge University Press, 1985.

[2] R. Paschotta. *Encyclopedia of Laser Physics and Technology*, volume 1. Wiley-VCH, 2008.

[3] Afshin Partovi, David Peale, Matthias Wuttig, Cherry A. Murray, George Zydzik, Leslie Hopkins, Kirk Baldwin, William S. Hobson, James Wynn, John Lopata, Lisa Dhar, Rob Chichester, and James H-J Yeh. High-power laser light source for near-field optics and its application to high-density optical data storage. *Applied Physics Letters*, 75(11):1515–1517, 1999.

[4] R.E. Rottmayer, S. Batra, D. Buechel, W.A. Challener, J. Hohlfeld, Y. Kubota, Lei Li, Bin Lu, C. Mihalcea, K. Mountfield, K. Pelhos, Chubing Peng, T. Rausch, M.A. Seigler, D. Weller, and XiaoMin Yang. Heat-assisted magnetic recording. *Magnetics, IEEE Transactions on*, 42(10):2417 –2421, oct. 2006.

[5] H.F. Hamann, M. O'Boyle, Y.C. Martin, M. Rooks, and H.K. Wickramasinghe. Ultra-high-density phase-change storage and memory. *Nature materials*, 5(5):383–387, 2006.

[6] J.-Q. Xi, Jong Kyu Kim, E. F. Schubert, Dexian Ye, T.-M. Lu, Shawn-Yu Lin, and Jasbir S. Juneja. Very low-refractive-index optical thin films consisting of an array of SiO_2 nanorods. *Opt. Lett.*, 31(5):601–603, Mar 2006.

[7] J.-Q. Xi, Martin F. Schubert, Jong Kyu Kim, E. Fred Schubert, Minfeng Chen, Shawn-Yu Lin, W. Liu, and J. A. Smart. Optical thin-film materials with low

refractive index for broadband elimination of fresnel reflection. *Nature Photonics*, 1(3):176–179, March 2007.

[8] M. F. Schubert, J.-Q. Xi, J. K. Kim, and E. F. Schubert. Distributed Bragg reflector consisting of high- and low-refractive-index thin film layers made of the same material. *Applied Physics Letters*, 90(14):141115–141117, April 2007.

[9] David Grosso, Cedric Boissiere, and Clement Sanchez. Ultralow-dielectric-constant optical thin films built from magnesium oxyfluoride vesicle-like hollow nanoparticles. *Nature Materials*, 6(8):572–575, August 2007.

[10] M.S. Sutton and J. Talghader. Zirconium tungstate (ZrW_2O_8)-based micromachined negative thermal-expansion thin films. *Journal of Microelectromechanical Systems*, 13(4):688 – 695, 2004.

[11] Wei Liu and Joseph J. Talghader. Thermally invariant dielectric coatings for micromirrors. *Appl. Opt.*, 41(16):3285–3293, Jun 2002.

[12] Zhouling Wu, L. Sheehan, and Mark Kozlowski. Laser modulated scattering as a nondestructive evaluation tool for defect inspection in optical materials for high power laser applications. *Opt. Express*, 3(10):376–383, 1998.

[13] E. Welsch and D. Ristau. Photothermal measurements on optical thin films. *Appl. Opt.*, 34(31):7239–7253, 1995.

[14] S. N. Jabr. Total internal reflection microscopy: inspection of surfaces of high bulk scatter materials. *Appl. Opt.*, 24(11):1689–1692, 1985.

[15] Christian F. Kranenberg and Kenneth C. Jungling. Subsurface damage identification in optically transparent materials using a nondestructive method. *Appl. Opt.*, 33(19):4248–4253, 1994.

[16] D. Rats, J. von Stebut, and F. Augereau. High frequency scanning acoustic microscopy: a novel non-destructive surface analytical tool for assessment of coating-specific elastic moduli and tomographic study of subsurface defects. *Thin Solid Films*, 355-356:347–352, 1999.

[17] M. Bashkansky, M. D. Duncan, M. Kahn, D. Lewis III, and J. Reintjes. Subsurface defect detection in ceramics by high-speed high-resolution optical coherent tomography. *Opt. Lett.*, 22(1):61–63, 1997.

[18] Michael Duncan, Mark Bashkansky, and John Reintjes. Subsurface defect detection in materialsusing optical coherence tomography. *Opt. Express*, 2(13):540–545, 1998.

[19] Haruo Endoh, Katsuhiko Miyamoto, Yoichiro Hiwatashi, and Tsutomu Hoshimiya. Measurement of subsurface defect shape by photoacoustic microscopy. *Japanese Journal of Applied Physics*, 41(Part 1, No. 5B):3361–3362, 2002.

[20] Annelise During, Mireille Commandre, Caroline Fossati, Bertrand Bertussi, Jean-Yves Natoli, Jean-Luc Rullier, Herve Bercegol, and Philippe Bouchut. Integrated photothermal microscope and laser damage test facility for in-situ investigation of nanodefect induced damage. *Opt. Express*, 11(20):2497–2501, 2003.

[21] Jeong Oh Kwon, Sang Il Seok, and Dongwoon Jung. Annealing effect on photoluminescence properties of Er doped Al_2O_3-SiO_2 sol-gel films. *J. Non-Cryst. Solids*, 352(26-27):2841–2845, 2006.

[22] M. J. Aitken. *Thermoluminescence dating*. Academic press, 1985.

[23] P. Braunlich, J. Gasiot, J. P. Fillard, and M. Castagne. Laser heating of thermoluminescent dielectric layers. *Applied Physics Letters*, 39(9):769–771, 1981.

[24] J. Gasiot, P. Braunlich, and J. P. Fillard. Laser heating in thermoluminescence dosimetry. *Journal of Applied Physics*, 53(7):5200–5209, 1982.

[25] Abdollah Abtahi, Peter F. Braunlich, and Paul Kelly. Theory of transient temperature response of a two-layer system heated with a localized laser beam. *Journal of Applied Physics*, 60(10):3417–3421, 1986.

[26] Paul Kelly, Abdollah Abtahi, and Peter F. Braunlich. Laser-stimulated thermoluminescence. II. *Journal of Applied Physics*, 61(2):738–747, 1987.

[27] J. F. Young, P. Kelly, A. Abtahi, P. F. Braunlich, and S. C. Jones. Transient solution of the diffusion equation for a composite system heated with a laser beam. *Journal of Applied Physics*, 66(11):5627–5629, 1989.

[28] M.L. Mah, M.E. Manfred, S.S. Kim, M. Prokic, E.G. Yukihara, and J.J. Talghader. Measurement of rapid temperature profiles using thermoluminescent microparticles. *Sensors Journal, IEEE*, 10(2):311 –315, 2010.

[29] M.L. Mah, M.E. Manfred, S.S. Kim, M. Prokic, E.G. Yukihara, and J.J. Talghader. Sensing of thermal history using thermoluminescent microparticles. In *Optical MEMS and Nanophotonics, 2009 IEEE/LEOS International Conference on*, pages 23 –24, 2009.

[30] M.L. Mah, P.R. Armstrong, S.S. Kim, J.R. Carney, J.M. Lightstone, and J.J. Talghader. Thermal history sensing inside high-explosive environments using thermoluminescent microparticles. *Accepted in Sensors Journal, IEEE.*

[31] Zhe-chuan Feng and Hong-du Liu. Generalized formula for curvature radius and layer stresses caused by thermal strain in semiconductor multilayer structures. *Journal of Applied Physics*, 54(1):83 –85, January 1983.

[32] S. Timoshenko. Analysis of bi-metal thermostats. *J. Opt. Soc. Am.*, 11(3):233–255, Sep 1925.

[33] G. Gerald Stoney. The tension of metallic films deposited by electrolysis. *Proceedings of the Royal Society of London. Series A, Containing Papers of a Mathematical and Physical Character*, 82(553):pp. 172–175, 1909.

[34] Dinguo Chen. Anti-reflection (ar) coatings made by solgel processes: A review. *Solar Energy Materials and Solar Cells*, 68(34):313 – 336, 2001. Sol-Gel Coatings.

[35] Shandon D. Hart, Garry R. Maskaly, Burak Temelkuran, Peter H. Prideaux, John D. Joannopoulos, and Yoel Fink. External reflection from omnidirectional dielectric mirror fibers. *Science*, 296(5567):510–513, 2002, http://www.sciencemag.org/content/296/5567/510.full.pdf.

[36] H. A. Macleod. *Thin-Film Optical Filters.* IOP, 2001.

[37] Bertrand G. Bovard. Derivation of a matrix describing a rugate dielectric thin film. *Appl. Opt.*, 27(10):1998–2005, May 1988.

[38] M. L. Barton and Z. J. Cendes. New vector finite elements for three-dimensional magnetic field computation. *Journal of Applied Physics*, 61(8):3919–3921, 1987.

[39] Sang-Hyun Oh. Class: EE8950 nanophotonics and plasmonics. Class note.

[40] F. Zheng, Z. Chen, and J. Zhang. A finite-difference time-domain method without the courant stability conditions. *Microwave and Guided Wave Letters, IEEE*, 9(11):441 –443, nov 1999.

[41] Kane Yee. Numerical solution of initial boundary value problems involving maxwell's equations in isotropic media. *Antennas and Propagation, IEEE Transactions on*, 14(3):302 –307, may 1966.

[42] Sangho S. Kim, Philip Armstrong, Merlin Mah, and Joseph J. Talghader. Interaction of heat gradients on thermoluminescence in heterogeneous multilayers. *Submitted to Journal of Physics D: Applied Physics*, 2013.

[43] Frank P. Incropera and David P. Dewitt. *Fundamentals of Heat and Mass Transfer*. John Wiley Sons, 4th edition, 1996.

[44] M. Grupen and K. Kearfott. Numerical analysis of infrared laser heating in thermoluminescent material layers. *Journal of Applied Physics*, 64(3):1044–1049, 1988.

[45] M. E. Grupen-Shemansky, K. J. Kearfott, and E. D. Hirleman. Numerical analysis of infrared laser heating in thermoluminescent material layers: The focused laser case. *Journal of Applied Physics*, 66(7):3407–3409, 1989.

[46] Rob F. Remis. On the stability of the finite-difference time-domain method. *Journal of Computational Physics*, 163(1):249 – 261, 2000.

[47] Timothy Tong. *Thermal Conductivity 22*. Technomic Publishing Company, 1994.

[48] Inc Almaz Optics. *Lithium Fluoride (LiF) Material Properties*. `http://www.almazoptics.com/LiF.htm`.

[49] Opto Technological Laboratory. Thermal properties of CaF_2, 2007. `http://www.optotl.com/mat/CaF2`.

[50] DuPont. Kapton polyimide films technical info. `http://origin.dupont.com/Kapton/en_US`.

[51] The Engineering ToolBox. Air properties. `engineeringtoolbox.com/air-properties-d_156.html`.

[52] I. Strzakkowski, M. Marczewski, and M. Kowalski. Thermal depopulation studies of electron traps in ion implanted silica layers. *Applied Physics A: Materials Science amp; Processing*, 40:123–127, 1986. 10.1007/BF00616488.

[53] G C Taylor and E Lilley. The analysis of thermoluminescent glow peaks in LiF (TLD-100). *Journal of Physics D: Applied Physics*, 11(4):567, 1978.

[54] R. Chen and S. A. A. Winer. Effects of various heating rates on glow curves. *Journal of Applied Physics*, 41(13):5227–5232, 1970.

[55] A Necmeddin Yazici, Reuven Chen, Semra Solak, and Zehra Yegingil. The analysis of thermoluminescent glow peaks of CaF_2:Dy (TLD-200) after beta-irradiation. *Journal of Physics D: Applied Physics*, 35(20):2526, 2002.

[56] Von H. Whitley and S. W. S. McKeever. Photoionization of deep centers in Al_2O_3. *Journal of Applied Physics*, 87:249–256, 2000.

[57] ThermoSientific. Thermoscientific tld material chart, May 2011. `https://fscimage.thermoscientific.com/images/D10472~.pdf`.

[58] P J Fox, R A Akber, and J R Prescott. Spectral characteristics of six phosphors used in thermoluminescence dosimetry. *Journal of Physics D: Applied Physics*, 21(1):189, 1988.

[59] M. Prokic and L. Botter-Jensen. Comparison of main thermoluminescent properties of some TL dosemeters. *Radiation Protection Dosimetry*, 47(1-4):195–199, 1993.

[60] Y S Horowitz, B Ben Shachar, and D Yossian. Study of the long-term stability of peaks 4 and 5 in TLD-100: correlation with isothermal decay measurements at elevated temperatures. *Journal of Physics D: Applied Physics*, 26(9):1475, 1993.

[61] Sangho S. Kim, Nicholas T. Gabriel, Woo-Bin Song, and Joseph J. Talghader. Encapsulation of low-refractive-index SiO_2 nanorods by Al_2O_3 with atomic layer deposition. *Opt. Express*, 15(24):16285–16291, Nov 2007.

[62] T Toyoda and M Yabe. The temperature dependence of the refractive indices of fused silica and crystal quartz. *Journal of Physics D: Applied Physics*, 16(5):L97, 1983.

[63] Martin T K Soh, Jeremy Thurn, J H Thomas III, and Joseph J Talghader. Thermally induced stress hysteresis and co-efficient of thermal expansion changes in nanoporous SiO_2. *Journal of Physics D: Applied Physics*, 40(7):2176, 2007.

[64] Crystran Ltd. *optical component material data for sapphire.* `http://www.crystran.co.uk/products.asp?productid=231`.

[65] Diana Riihel, Mikko Ritala, Raija Matero, and Markku Leskel. Introducing atomic layer epitaxy for the deposition of optical thin films. *Thin Solid Films*, 289(1-2):250 – 255, 1996.

[66] M. D. Groner, S. M. George, R. S. McLean, and P. F. Carcia. Gas diffusion barriers on polymers using Al_2O_3 atomic layer deposition. *Applied Physics Letters*, 88(5):051907, 2006.

[67] E. Langereis, M. Creatore, S. B. S. Heil, M. C. M. van de Sanden, and W. M. M. Kessels. Plasma-assisted atomic layer deposition of Al_2O_3 moisture permeation barriers on polymers. *Applied Physics Letters*, 89(8):081915, 2006.

[68] D. Bhattacharyya, N. K. Sahoo, S. Thakur, and N. C. Das. Spectroscopic ellipsometry of TiO_2 layers prepared by ion-assisted electron-beam evaporation. *Thin Solid Films*, 360(1-2):96 – 102, 2000.

[69] Martin Jerman, Zhaohui Qiao, and Dieter Mergel. Refractive index of thin films of SiO_2, ZrO_2, and HfO_2 as a function of the films' mass density. *Appl. Opt.*, 44(15):3006–3012, May 2005.

[70] J. Dolbow and M. Gosz. Effect of out-of-plane properties of a polyimide film on the stress fields in microelectronic structures. *Mechanics of Materials*, 23(4):311 – 321, 1996.

[71] R B Roberts. Thermal expansion reference data: silicon 300-850 K. *Journal of Physics D: Applied Physics*, 14(10):L163, 1981.

[72] Sangho S. Kim, Nicholas T. Gabriel, Wing S. Chan, and Joseph J. Talghader. Infrared absorption signature on laser-damaged optical thin films. *Opt. Lett.*, 34(14):2162–2164, Jul 2009.

[73] Sangho S. Kim, Nicholas T. Gabriel, Wing S. Chan, and Joseph J. Talghader. Early thermal damage in optical coatings identified by infrared spectral signatures. In Gregory J. Exarhos; Vitaly E. Gruzdev; Detlev Ristau; M. J. Soileau; Christopher J. Stolz, editor, *Laser-Induced Damage in Optical Materials: 2009*, volume 7504 of *Proc. SPIE*, pages 69–75, 2009.

[74] Caroline M. Parler, James A. Ritter, and Michael D. Amiridis. Infrared spectroscopic study of sol-gel derived mixed-metal oxides. *J. Non-Cryst. Solids*, 279(2-3):119–125, 2001.

[75] J R Harvey and S J Felstead. Thin-layer thermoluminescent dosemeters based on high-temperature self-adhesive tape. *Physics in Medicine and Biology*, 24(6):1250, 1979.

[76] Zureks. Skin effect in wikipedia, May 2011. `http://en.wikipedia.org/wiki/Skin_effect`.

[77] B. Burgkhardt, R. Herrera, and E. Piesch. Fading characteristics of different thermoluminescent dosimeters. *Nuclear Instruments and Methods*, 137(1):41 – 47, 1976.

[78] G. Erfurt and M. R. Krbetschek. A radioluminescence study of spectral and dose characteristics of common luminophors. *Radiation Protection Dosimetry*, 100(1-4):403–406, 2002.

[79] A. Peto and A. Kelemen. Radioluminescence of LiF:Mg,Ti induced by 4 MeV electrons. *Radiation Measurements*, 24(4):571 – 573, 1995.

Appendix A

Glossary and Acronyms

Care has been taken in this thesis to minimize the use of jargon and acronyms, but this cannot always be achieved. This appendix defines jargon terms in a glossary, and contains a table of acronyms and their meaning.

A.1 Glossary

A.2 Acronyms

Table A.1: Acronyms

Acronym	Meaning
ALD	Atomic Layer Deposition
np-SiO_2	Nanoporous SiO_2
EB	Electron Beam
SEM	Scanning Electron Microscope
CTE	coefficient of thermal expansion
CVD	chemical vapor deposition
LIDT	Laser Induced Damage Threshold

Continued on next page

Table A.1 – continued from previous page

Acronym	Meaning
TL	Thermoluminescence
TE	Transverse Electric
TM	Transverse Magnetic
TLD	Thermo Luminescence Dosimetry
TCR	temperature coefficient of resistance
BTLC	Bonded Thermoluminescent Dosimetry chips
DBR	Distributed Bragg Reflector
FTIR	Fourier Transform Infrared spectroscopy